Polytechnic of Turin

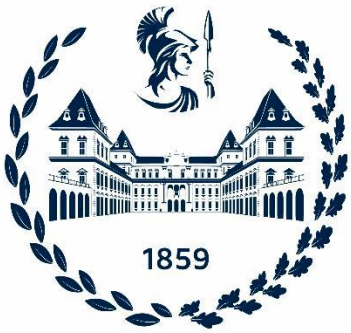

College of Chemical and Materials Engineering

Master's Degree Program in Materials Engineering

Master's Thesis

The influence of Hot Isostatic Pressing performed above solidus temperature of LPBFed Inconel 939 for microstructural improvement

Thesis supervisor:

Dr. Daniele Ugues

Dr. Emilio Bassini

Candidate:

Alessandro Ruggieri

Academic year: 2023/2024

Abstract

Ni-based superalloys are a particular class of metallic materials primarily used in the energy production field (nuclear, oil and gas) and in the aerospace sector, where they are particularly employed in the production of turbine blades and casings. This is because Ni-based superalloys retain their mechanical stability at high temperatures, as they can operate up to 80-85% of their melting temperature without experiencing a significant loss in strength. Moreover, they exhibit excellent high-temperature oxidation resistance, a crucial aspect for sectors with extreme temperature conditions or contact with corrosive fluids. However, these alloys are challenging to process due to their high melting temperature, poor castability, and forgeability, which only allows the production of components with simple geometries. This makes additive manufacturing a highly appealing process for these alloys. Using additive manufacturing, it is possible to create components with more complex geometries and a defect structure and microstructure that differ completely from traditional methods, such as casting and wrought. The only issue with using this technology is the resulting microstructure at the end of the process; specifically, the grain structure is extremely fine, which is excellent for fatigue resistance but not effective for creep resistance, a crucial consideration for this type of alloy. This is where hot isostatic pressing (HIP) is used as a treatment, combining high temperature and high pressure to address this issue. Literature indicates that this treatment primarily pertains to components not produced with AM technology but rather with traditional processes, and this is where the following thesis finds its focal point. The main purpose of this thesis is to determine the feasibility of a dedicated HIP treatment on Laser Powder Bed Fusion (LPBF) Inconel 939, conducted above its solidus temperature, i.e. within the incipient melting region of the alloy. This is because if a standard high-temperature heat treatment were applied, it would reach the incipient melting region but would also cause uncontrolled porosity, damaging the material. By applying high pressure as well, it is possible to enter the incipient melting region without forming the liquid. Additionally, the use of HIP helps reducing the crystalline anisotropy typical of the LPBF process, favouring a more equiaxed structure, effectively coarsening grain boundaries, thus improving creep resistance. Furthermore, material density increases to almost the theoretical value since defects are easily healed. The results obtained in this study show that using HIP above the solidus temperature allows for AM components with a crystalline structure more suitable for high-temperature applications, where creep resistance is a critical factor to consider.

Chapter 1

1. State of art

1.1. Superalloys

The term "Superalloy" refers to a group of alloys based on nickel, cobalt or iron-nickel with superior strength properties provided by reinforcing intermetallic phases such as γ' and γ". Originally developed during WWII and in the early 1950s for military gas turbines, they have been continuously advanced, and a large number of new materials have been introduced. These materials are used for a wide range of applications including aerospace, power generation and multiple niche markets, such as high-end automotive components [1].

According to metallurgist, Superalloys can be defined as follows: "A superalloy, or high-performance alloy, is an alloy usually based on Group VIII B (usually consisting of various combinations of Fe, Ni, Co and Cr) elements that exhibit excellent long-time strength, creep resistance, corrosion and erosion at temperature above 650 °C, good surface stability, corrosion and oxidation resistance. Superalloy development has relied heavily on both chemical and process innovations and has been driven primarily by the aerospace and power industries." [2]

One of their most interesting characteristics is their ability to maintain high mechanical strength at elevated temperatures (typically up to 80% of their absolute melting temperature). Additionally, they exhibit excellent hot corrosion and oxidation resistance, which makes them suitable for applications at very high service temperature (up to 1000 °C).

Superalloys are known to have rather complex chemical compositions and are usually classified according to their base element and strengthening mechanisms, as shown in Fig. 1.

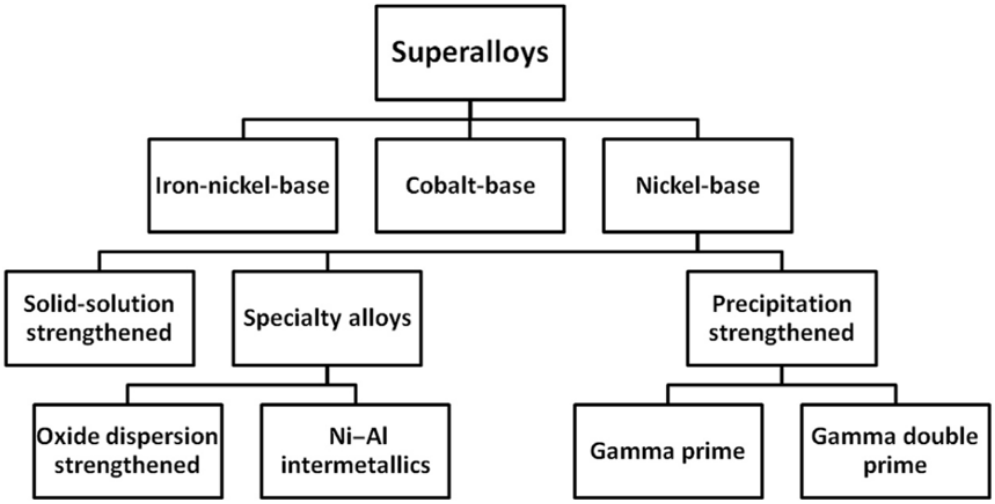

Fig. 1 Classification of Superalloys

The superalloy family can be divided in three main groups:

- Ni-based superalloys.
- Ni-Fe based superalloys.
- Co based superalloys.

The common feature in these alloys is their face-centered cubic (FCC) crystal structure, also called the gamma (γ) phase. Fe- and Co-based superalloys typically have a body-centered cubic (BCC) structure at room temperature, but can also retain the austenitic FCC structure by additions of Nickel. All the Ni-based superalloys have an austenitic FCC γ matrix phase at room temperature and variable number of secondary phases including FCC gamma prime γ' and body-centered tetragonal (bct) gamma double γ". For the most demanding applications, for example hot gas path components in land-based and aeronautical gas turbines, Ni-based superalloys are omnipresent as they outperform other superalloys [1].

1.1.1. Strengthening Mechanisms

Superalloys are strengthened by three principal mechanisms: solid solution hardening (SSH), precipitation hardening (PH) and dispersion strengthening:

1. **Solid-Solution Strengthening**: This is characterised by the addition of different elements in solution leading to an increase in the strength of the matrix. The

distortion of the atomic lattice, caused by atomic radius mismatch, inhibits the movement of dislocations. The use of high melting point elements as solutes provides strong lattice cohesion and reduces diffusion, particularly at high temperatures. Similar considerations apply to the hardening of the γ' phase. Moreover, this type of reinforcement leads to a decrease in the stacking fault energy (SFE) in the crystal lattice, which results in an inhibition of the dislocation cross slip, the most important deformation mechanism at high temperatures for imperfect crystals. The reduction of the SFE makes harder for dislocation change the slip plane [3].

2. **Precipitation Strengthening**: The addition of Al, Ti and Nb allows the formation of intermetallic compounds, usually coherent with the matrix, like γ' [Ni_3(Al, Ti)] and γ" [Ni_3Nb]. The solubility in the matrix is not great and it is also reduced by lowering the temperature. Considering this behaviour, it is possible to form fine precipitates well dispersed in the alloy performing solution treatments followed by aging treatments. The presence of precipitates has the beneficial effect of limiting the dislocations movements, which must pass inside the particles using more energy [4]. There are different factors that influence the strengthening effectiveness of a precipitate:
    - mismatch of lattice parameters formed between the matrix alloy (γ) and precipitates (such as γ' and γ").
    - the antiphase-boundary (APB) energy present when there are ordered precipitates, like γ' and γ". The APB energy represents the energy needed for dislocation to cut through the ordered precipitate.
    - the volume fraction of the precipitate.
    - the precipitates particle size.
    - the homogeneity of the precipitate distribution.
3. **Dispersed oxides strengthening**: This is a mechanism similar to precipitation hardening, except that the strengthening agent is added to the alloy and not precipitated from the matrix. The production of this family of superalloys is complicated by the fact that the density of ceramics is lower than the metal matrix and tend to float to the surface of the molten metal during casting. The oxide

particles are usually characterized by a particle dimensional range from 25 to 50 nm. The oxides presence in the matrix enhances mechanical resistance and creep properties of the alloy, providing stable properties for long times. Moreover, oxides are found to be beneficial for the oxidation resistance of the alloy, since they act like as nucleation agents for protective oxides and make the formed oxide layer smooth. In order to maximize the high temperature creep resistance, grains are preferred to be big and with a high aspect ratio parallel to the working direction. This condition can be achieved choosing the correct post processing, obtaining high creep-rupture strengths for temperatures up to 90% of their melting temperature [4], [5].

1.2. Ni-based Superalloys

Ni-based superalloys are an unusual class of metallic materials with an exceptional combination of high-temperature strength, toughness and resistance to degradation in corrosive or oxidizing environments. Casting is favoured for high strength and creep resistance in high-temperature applications. One example of application is turbine blade and discs production via, investment-casting, where Inconel Alloys 100, 713, 738 and 792 are normally adopted.

Typically, Ni-based superalloys constitute 40-50% of the total weight of an aircraft engine and are used most extensively in the combustor and turbine sections of the engine, where elevated temperatures are maintained during operation. The superior high-temperature capability of nickel-base superalloys is due to the precipitation of high-volume fractions of the γ'-Ni_3(Al, Ti) phase, which requires combined Al and Ti contents of at least 4-6%. Because of the high-volume fraction of γ' phase, there is a significant challenge in hot working due to the alloy high-temperature strength. When γ' volume fractions are higher than 40 to 45 percent, the gap between the solvus and incipient melting temperature becomes too narrow for practical purposes and limits manufacturing methods to casting or powder metallurgy [6].

1.2.1. Effects of alloying elements in Ni-based superalloys

One effect of the solution of alloying elements in Ni is the changing of the lattice parameter of Ni. All the common substitutional alloying elements expand the lattice parameter of Ni, the rate of expansion per solute addition being the greatest for Nb, W and Mo, and the least for Co, Cr and Fe [7]. The major alloying elements that may be present in nickel-base superalloys are illustrated in Fig. 2, where the height of the element blocks represents the amounts that may be present.

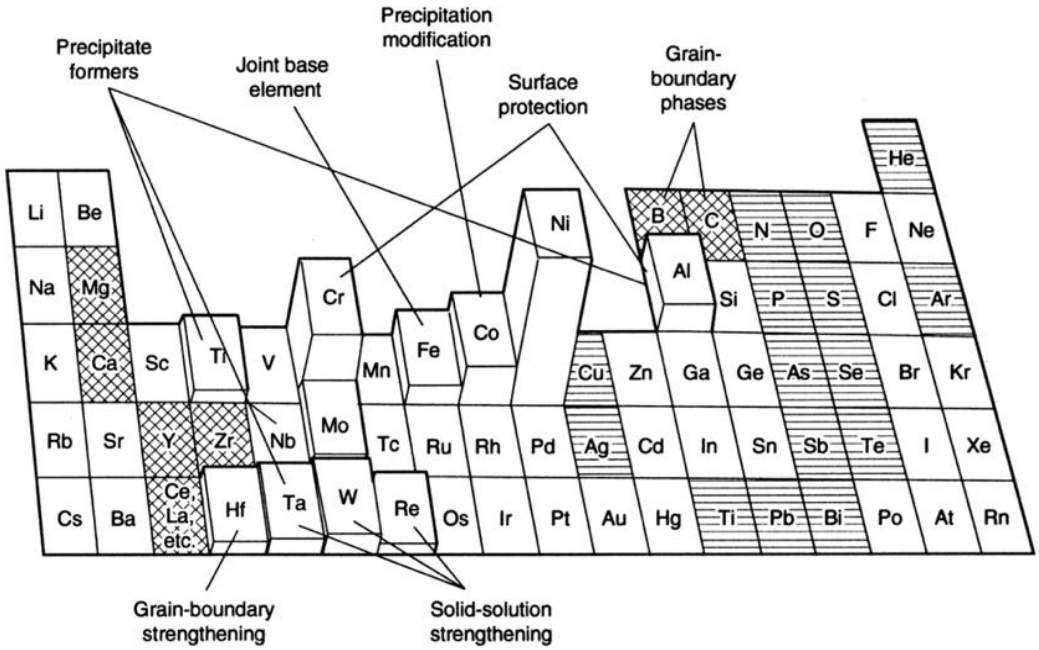

Fig. 2 Alloying elements used in Ni-base superalloys. Beneficial minor elements are marked with crosshatch, while detrimental tramp elements are marked with horizontal line hatch.

In general, refractory alloying elements with large differences in electronic structure and atomic radii, compared to Ni, such as Mo, W, Nb and Re, are added for solid solution strengthening of the γ phase. Additions of Ti, Ta and Nb contribute to the formation and strengthening of the Ni_3(Al, Ti, Ta, Nb) γ' phase. In particular, Ta and Nb are often alloyed in order to precipitate intermetallic precipitates. If these elements are to be used as solid solution strengtheners, it is also important to consider the relative stability of their nitrides [8].

Additions of Cr (up to 20%), Y and La typically improve oxidation and/or corrosion behaviour, which is optimized via formation of an adherent slow-growing alumina scale. A

high Cr content imparts a high hot corrosion-oxidation resistance to the alloy. Also, the high Cr and especially Co contents reduce the solubility of the γ' forming elements in the matrix phase, thereby making the most efficient use of the relatively low levels of these elements present in the alloy, by maximizing the precipitation of γ' [9]. Lastly, the combined effects of the addition of Co and the increase of (Ti + Al) content, enhance the service temperature of the superalloy [7].

Minor additions of B, C, Hf and Zr tend to result in the formation of borides or carbides, often located at the grain boundaries. These elements are important for control of grain size during wrought processing and for minimization of damage accumulation at grain boundaries in service [10]. The role of B on weldability is well established and this element has a strong, deleterious effect on solidification and liquation cracking susceptibility. The cracking resistance of the low B heat is excellent, while the high B heat is very susceptible to cracking. The detrimental influence of B can be attributed to its strong segregation tendency and formation of a M_3B_2 type phase that forms at the relatively low temperature of ~1200 °C [11].

Carbon exhibits a high affinity for elements such as Hf, Zr, Ti, Nb, W, Mo, V and Cr, and tends to form primary MC (where M is metal atom) carbides directly from the liquid during solidification of Ni-based superalloys. The carbides are particularly essential in the grain boundaries of poly-crystal cast alloys for the production of desired strength and ductility characteristics [10].

Depending on the composition of the primary MC carbide and the constituent elements present in the alloy, sub-sequent solid-state transformation may decompose the MC carbide into variety of $M_{23}C_6$, M_6C and M_7C_3 carbides during heat treatment or in service. The carbides encountered in superalloys serve three principal functions. First, grain boundary carbides, when properly formed, strengthening results. Third, carbides can tie up certain elements that would otherwise promote phase instability during service [12].

Therefore, the microstructure of a typical superalloy consists of different phases [13]:

I. The gamma phase, denoted γ. This exhibits FCC structure, and in almost all cases, it forms a continuous matrix phase in which the other phases reside. It contains significant concentrations of elements such as cobalt, chromium, molybdenum,

ruthenium and rhenium. Where these elements are present, they prefer to reside in this phase.

II. The gamma prime precipitate, denoted γ'. This one forms a precipitate phase, which is often coherent with the γ-matrix, and rich in elements such as aluminium, titanium and tantalum. In nickel-iron superalloys and those ones rich in niobium, a related ordered phase, γ", is preferred instead of γ'.

III. Carbides and borides. Carbon often presents at concentrations up to 0.2 wt.%, combines with reactive elements such as titanium, tantalum and hafnium to form MC carbides. During processing or service, these can decompose to other species, such as $M_{23}C_6$ and M_6C, which prefer to reside on the γ-grain boundaries, and which are rich in chromium or molybdenum and tungsten. Boron can combine with elements such as chromium or molybdenum to form borides that reside on the γ-grain boundaries.

IV. Other secondary phases. The eta (η) phase, which is a hexagonal closed pack (HCP)-type Ni_3Ti or ($Ni_6TiAlNb$) ordered phase, which is an ordered orthorhombic intermetallic compound; the delta (δ) phase, that is an orthorhombic Ni_3Nb ordered intermetallic compound.

The γ', γ" and η phases are also known as the geometrically close-packed (GCP) phases. Due to their ordered crystal structure, the γ', γ", δ and η phases play an important strengthening role in the Nickel-based superalloys. In addition to grain size and morphology (plus occasional cold work), it is the production and control (manipulation) of the various phases that give superalloys their unique characteristics [14], [15].

1.3. γ phase matrix

In nickel-based superalloys the matrix phase γ is a solid solution of the alloying elements in Ni, at least at temperatures approaching the melting point of the alloy. The main element present in the matrix-phase composition is the superalloy base metal, but there are also other solid-solution elements as mentioned in the previous paragraph. The fcc γ-phase matrix is ideal for high-temperature structural alloys for several reasons:

- The fcc matrix is tough and ductile, stable up to high temperatures, not as dense or expensive as Co and it has high microstructural stability. In addition, it offers good resistance to oxidation and corrosion.
- The densely packed fcc matrix is ideal for use at relative high temperatures (T/T_m) because of the low diffusivity of alloying elements.
- The fcc matrix has a broad solubility of secondary elements that permits precipitation of intermetallic compounds, such as γ' and γ" for strengthening, and allows the dissolution of high-melting point refractories [16].

1.4. Geometrically Close-Packed Phases

Geometrically close-packed (gcp) phases are intermetallics with the formula of A_3B. They include the principal strengthening γ', γ", η, and δ phases. The gcp phases are close-packed in all directions, unlike the tcp phases, which have regular layered interruptions in their close-packed structure.

1.4.1. γ' phase - Ni_3Al / $Ni_3(Al, Ti)$

The nickel-aluminium system is the binary basis for superalloys' compositions. As the level of aluminium added to γ-nickel increases, the second precipitate phase forms through the nominal composition of Ni_3Al, designated as γ'. Both the Ni_3Al compound and the matrix have a face-centered cubic crystal. It presents an ordered system with Ni atoms on the cube faces and the Al atoms at the cube edges. It is also important to know that up to 60% of the Al atoms could be replaced by Ti in Ni_3Al with only a slight increase in the lattice parameter. In general, the effect of replacing part of the Al with Ti in Ni-Cr-Co based alloys is to decrease the rate of growth of the γ'-precipitates and, thus, delay over-aging. Also, Ti is more significant than Al in imparting strength at higher temperatures, probably due to a higher solution temperature of $Ni_3(Al, Ti)$ versus that of Ni_3Al [7].

The volume fraction of the γ' phase is important for determining the strength and creep properties of the alloy and for determining the manufacturing processes, that can be used to produce a particular component. Although alloys can be hot worked at low γ' volume fractions, beyond 40 to 45 percent volume fraction of γ' (60 percent in case of powder materials), forging is no longer practical, and the component must be manufactured by

casting [16]. The phase forms as a coherent precipitate within the γ matrix, with morphologies dependent on heat treatment and exact composition. The coherence between the γ' phase and fcc γ matrix is maintained by tetragonal distortions. As a result, the nucleation of homogeneous precipitates with low surface energy and extraordinary long-time stability is possible. The properties of the superalloys are found to depend critically on the coherency of the γ/γ' interface [16]. This is favoured by small values of the lattice misfit, δ, defined according to:

$$\delta = \frac{\alpha_{\gamma'} - \alpha_{\gamma}}{\left(\frac{\alpha_{\gamma'} + \alpha_{\gamma}}{2}\right)}$$

This parameter is an important factor in determining the morphology of the γ' precipitate. The mismatch increases considerably when Ti is substituted for Al in these alloys [11]; furthermore, as the γ/γ' ratio increases, the resistance to high-temperature creep improves, because the γ/γ' interface is a barrier to mobile dislocations and an obstacle to plate thickening due to dislocation pile-up at the interface. The size of the γ' precipitate is also important in providing effective precipitation hardening, because the hardening generally increases with particle size until the particle reaches a critical size. The shape, which could be spheroidal or could assume the shape of cubic particles, appears as square, triangles or trapezoids in polished sections [7]. The size of the γ' precipitate can be modified through a coarsening process that takes place more rapidly at higher aging temperatures. Moreover, one of the most significant features of the γ' phase is that its yield strength increases with temperature in the range from -196 to 800 °C. The relationship between yield strength and temperature is also highly dependent on the aluminium content in the γ' phase, with the magnitude and position of the peak in flow stress being controlled by the presence of other alloying elements such as Ti, Cr and Nb [16].

The disadvantage of γ'-strengthened alloys is that the service temperature and life of the component are ultimately limited by the coarsening and dissolution of the γ' precipitates. In practice, much lower solvus temperatures for γ' are observed because of the effect of other elements of the alloy. Moreover, as the γ' solvus temperature approaches the alloy incipient melting point, heat treating of γ' precipitation-hardened alloys become more challenging. Formation of the γ' phase occurs in the solid state as the supersaturated solid solution of γ-nickel is cooled below its equilibrium solvus temperature. Hence, the precipitation and

growth kinetics of the γ' phase are highly sensitive to the rate at which the alloy is cooled through the solvus temperature. The presence of a high-volume fraction of the γ' phase is key to strengthening [10].

1.4.2. γ" phase - Ni_3Nb

The gamma double prime γ" precipitate is a useful strengthening phase, mainly in such nickel-iron-base superalloys as 718 and 706 alloys. The γ" precipitate is a coherent bct Ni_3Nb phase with an ordered D022 crystal structure that assumes a disk-shaped morphology. This phase provides very high strength at low-to-intermediate temperatures, but it is unstable at temperatures above 650 °C, caused by the loss of the strengthening γ" phase as it transforms to δ, and this evolution is associated to a lowering in the creep properties. Nickel-iron-base alloys are particularly susceptible to the transformation of γ" to δ at temperatures above 650 °C.

The morphology is disk-shaped, with the thickness under 10 nm and the diameter around 50nm; the reinforcement, brought by γ", is caused by the large mismatch between the precipitate and the matrix lattice parameter, that is around the 3%. Alloys hardened forming γ" precipitate are not subject to strain age cracking, since the γ" precipitate is formed at a much slower rate than γ'.

1.4.3. η phase

The η phase is generally regarded as a detrimental phase, exerting negative effect on tensile and creep-rupture properties and this effect is largely attributed to its formation and growth at the expense of the strengthening phase γ'. It is widely accepted that γ'-Ni_3(Al, Ti) is metastable, compared to η phase, at relatively high temperatures (above 750 °C) and would transform into the η phase in some superalloys [17]. This phase has a hexagonal close-packed (hcp) structure and has been reported to have different chemistry in different superalloys. In IN939 alloy (Ti/Al = 1.9), η phase begins to precipitate around the MC carbides during the cooling process of casting. Generally, the η phase precipitates at the grain boundary in a cellular mode at low temperatures (< 850 °C) and develops a Widmanstätten morphology throughout the grain at high temperatures (> 850 °C) [18]. At high temperatures, because

the intragranular diffusion rate is accelerated, the η phase extends into the grain interior and consumes γ'.

1.4.4. δ phase

The equilibrium structure corresponding to the γ" (Ni_3Nb) phase is the orthorhombic incoherent δ (Ni_3Nb) phase. The precipitation of the δ-phase is highly heterogeneous because of the dissimilar structure with respect to the FCC γ-matrix. The precipitation of δ-phase occurs at the temperature range of approximately 750-1020 °C. At the lower temperatures, below ~900 °C, the precipitation of the δ phase is preceded by γ" precipitation, but at higher temperatures the δ-phase precipitates directly from the austenite. It is known that the volume fraction of the δ phase increases with increasing aging time. Furthermore, with the increase in aging time, the precipitation method changes from a single mode of precipitation along the grain boundary, to two modes of precipitation along the grain boundary and direct precipitation inside the grain. It also changes the appearance, going from a short rod-shaped δ phase to a needle-shape δ phase with an increase in aging time [19].

1.5. Carbides

The role of carbides in superalloys is complex, in general they provide a beneficial effect on rupture strength at high temperature if present in the right type (composition) and morphology. The shape of carbides also plays a role in alloy ductility. Indirectly, carbides adversely affect the chemical stability of their matrix by locally depleting carbide-forming elements [16]. In Ni-based superalloys, carbide formation is required to stabilize the structure against high-temperature deformation; this is accomplished by the formation of carbide networks at the grain boundaries. These networks inhibit grain-boundary motion, thus increasing creep and stress-rupture properties [7]. The effects of carbides upon high-temperature properties are dependent upon the type of carbide present and its morphology. The carbides encountered in superalloys serve three principal functions [20]:

1. Grain boundary carbides, when properly formed, strengthen the grain boundary, prevent or retard grain-boundary sliding and permit stress relaxation.
2. If fine carbides are precipitated in the matrix, strengthening results.

3. Carbides can tie up certain elements that would otherwise promote phase instability during service.

The most stable carbide found in Ni-based superalloys are the MC carbides, where M usually represents Ti, although part of the Ti may be substituted by Nb, Ta, W, Mo and Cr, depending upon alloy composition. The MC carbides are formed as discrete blocky particles or as eutectic phases, during casting solidification and commonly have an FCC crystal structure. These carbides form during solidification, occurring as discrete particles distributed heterogeneously throughout the alloy, at both intergranular and intragranular locations, and often form between dendrites. Precipitation from solid solutioned alloys is possible at temperature higher than 1038 °C and during cooling [5].

Depending on the composition of the primary MC carbide and the constituent elements present in the alloy, subsequent solid-state transformation can decompose the MC carbide into the variety of $M_{23}C_6$, M_6C and M_7C_3 carbides during heat treatment or in service. Carbides such as $M_{23}C_6$ form at lower temperatures – around 750 °C – during protracted periods of service exposure, particularly in alloys which are rich in Cr [13]. Their formation has been attributed to the breakdown of the MC carbides, via reactions of the type:

$$MC + \gamma \rightarrow M_{23}C_6 + \gamma'$$

The $M_{23}C_6$ carbide is favoured by exposure temperatures of about 790 to 820 °C and it's usually found to precipitate on the γ-grain boundaries [13]. The complex cubic structure exhibited by this phase is, in fact, closely related to that of σ. This fact explains why σ is found to nucleate sympathetically from $M_{23}C_6$ in polycrystalline turbine disc alloys like *Udimet 720Li* and *RR1000*.

The M_6C carbides can also precipitate in blocky form in grain boundaries and, less often, in a Widmanstätten intragranular morphology. They have a complex cubic structure and form when the molybdenum and/or tungsten content is more than 6 to 8 at. %, typically, in the temperature range of 815 to 980 °C. Because M_6C carbides are stable at higher temperature levels than are $M_{23}C_6$ carbides, M_6C is the carbide more commercially important as a grain-boundary precipitate for controlling grain size during the processing of wrought alloys [12].

Although M_7C_3 is not widely observed in superalloys, it is present in some cobalt-base alloys and in Nimonic 80A after heated above 1000 °C. This carbide is usually found with a blocky shape at the grain boundary. Additions of such elements as cobalt, molybdenum, tungsten or niobium to nickel-base alloys prevent formation of M_7C_3.

Carbide dispersions are sometimes thought to reduce alloy incipient melting temperature, but this is an indirect effect. The reduced melting temperature is due to the higher carbon contents necessary to form the carbides. After the carbides' dispersion, the incipient melting temperature is observed to increase, not directly because of the carbides but because of the manufacturing method, which allows residual carbon concentration to be reduced [16].

1.6. Borides

Small additions of minor elements, especially zirconium and boron, are essential to improve creep-rupture resistance of superalloys. Borides can be used to strengthen nickel-base alloys in a similar manner to carbides; they can also improve the hot workability of an alloy [16]. Complex borides tend to have high molybdenum, titanium, chromium and nickel contents and a tetragonal crystal structure in one or two forms. The first is a low-lattice-parameter eutectic product MM'_2B_2, where M and M' are respectively large- (molybdenum, titanium) and small- (chromium, nickel, cobalt) radius elements. The second is a high-lattice-parameter $M_2M'B_2$ spheroidal form. Borides are hard particles, blocky to half-moon in appearance, that are observed at grain boundaries, but not at the same volume with which carbides appear. The boride commonly found in superalloys is of the form M_3B_2, with a tetragonal unit cell [16], [20]. It is accepted that the high-temperature creep properties of the superalloys are improved in many circumstances if carbon and boron are present; the formation of these phases is then very likely. This is primarily due to the preferred location of carbon, boron, carbides and borides at the γ-grain boundaries, which has a potent effect on the rupture strength via the inhibition of grain boundary sliding, they are referred to as grain-boundary strengtheners. This explains why carbon and boron levels are generally higher in polycrystalline or columnar-grained superalloys used in cast form, and the absence of these elements in the single-crystal superalloys, for which grain boundary strengthening is unnecessary [13].

1.7. Topologically Close-Packed Phases

Topologically close-packed (TCP) phases are undesirable, and considerable effort is made to avoid compositional ranges that will cause their precipitation during heat treatment or service. The TCP phases that are commonly observed in Ni-base superalloys, are summarised in Table 1 and they include σ-A_xB_y, μ-$A_{x'}B_{y'}$ and Laves-A_2B phases, where A is iron, nickel, or cobalt, and B is niobium, molybdenum, tantalum, or chromium [16], [21].

Table 1 TCP phases in nickel-base superalloys. Adapted from [21]

Phase	Stoichiometric composition	Unit cell type	Space group	Lattice parameters
μ	A_6B_7	Rhombohedral	166. R-3M	$a = b = 0.4755$ nm $c = 2.583$nm
P	e.g. $Cr_{18}Mo_{42}Ni_{40}$	Primitive orthorhombic	62. Pbnm	$a = 1.698$ nm $b = 0.475$ nm $c = 0.907$ nm
R	e.g. $Cr_{18}Mo_{31}Co_{51}$	Rhombohedral	148. R-3	$a = b = 1.093$ nm $c = 1.934$ nm
σ	A_2B	Tetragonal	136. $P4_2/mnm$	$a = b = 0.878$ nm $c = 0.454$nm
Laves	AB_2	Hexagonal (C14 and C36)	194. $P6_3/mmc$	$a = b = 0.475$–0.495 nm $c = 0.77$–0.815 nm
		Cubic (C15)	227. Fd-3m	

In polycrystalline alloys the precipitation of TCP phases, in continuous films on grain boundaries, along with carbides, can be a mechanism for loss of ductility and increase of fatigue crack growth rate, by providing a continuous path for crack propagation [21]. TCP phases are very detrimental because of two main factors. At first, when they nucleate and grow, they deplete the γ-matrix phase from solid solution strengtheners; this leads to decreased creep resistance of the material. Further, TCP phases are brittle and exhibit a complex lath- or plate- like morphology, which evolves with time [15]. The most detrimental TCP phase is the σ phase, which is based upon stoichiometry A_2B and has a tetragonal cell containing 30 atoms with different compositions [13]; it is characterized to have brittle behaviour and a tendency to form plates or needles, that act as crack initiation and propagation sites. μ is a rhombohedral phase with composition Co_2W_6, $(Fe, Co)_7(Mo, W)_6$ generally present in alloys rich in Mo and/or W. The appearance is coarse, irregular forming Widmanstätten platelets. It tends to form during exposure at high temperatures. Laves phases usually are composed by globules with irregular shapes, elongated or by platelets, when the alloy experiences high temperature for long periods. The crystal structure is hexagonal, and the possible compositions are: Fe_2Nb, Fe_2Ti, Fe_2Mo, Co_2Ta and Co_2Ti.

1.8. An overview of IN939

IN939 is an age-hardenable superalloy, it was developed to meet the need for a strong, highly corrosion resistant alloy capable of operating for long times at temperatures of ~850 °C, i.e. consistent with the materials requirements for blades and vanes in land-based gas turbines [22]. The chemical composition is reported in Table 2.

Table 2 The general chemical composition of IN939 alloy [23].

Element	Composition [wt.%]	Element	Composition [wt.%]	Element	Composition [wt.%]
Al	1,9	**Fe**	<0,5	**S**	<250ppm
Ni	Bal.	**Mn**	<0,5	**B**	<0,03
C	0,15	**W**	2	**Si**	<0,5
Co	19	**Nb**	1	**Ti**	3,7
Cr	22	**Ta**	1,4	**Zr**	<0,03

The strengthening mechanism of the alloy is due to the combination of the dendritic gamma solid solution matrix (γ) with a dispersion of gamma-prime precipitates (γ') Fig. 3(d), which enhances its mechanical properties. The IN939 is typically produced as a solid cast and contains a large volume fraction of γ' phase Fig. 3(a), which can reach up to 30-40% after heat treatment, and a γ-γ' eutectic phase, that results from slower cooling, as can be seen in Fig. 3(c) [23].

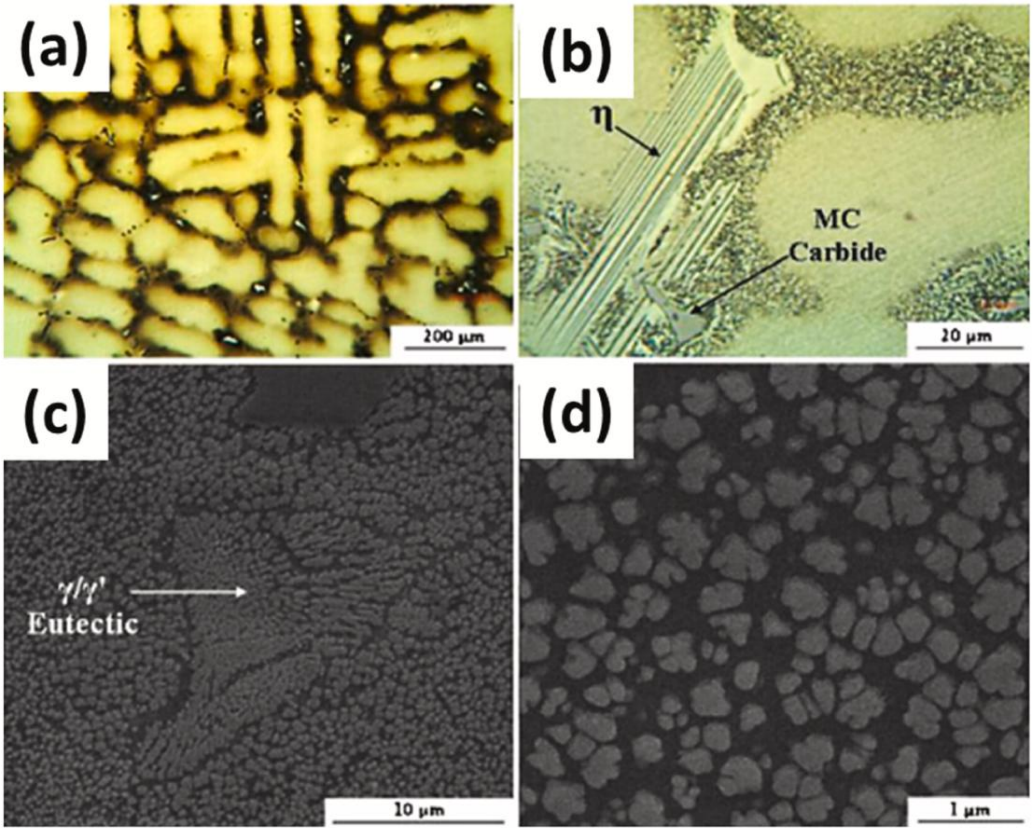

Fig. 3 The microstructure of the cast specimen showing (a) the dendritic microstructure, (b) the MC phase and η phase, (c) the γ/γ' phase, (d) rose like γ' precipitates. Adapted from [24].

The phases most commonly found in this type of superalloy are γ, γ', MC, $M_{23}C_6$, σ, and η. All these phases have been extensively studied and detailed in the previous paragraphs. Some of these phases are detrimental and they tend to appear after long service periods (σ); others, such as η, are present in the as cast alloy and can be removed performing a solution treatment. Unfortunately, long service times tend to transform phases, coarsening γ' and carbides, and eventually making them to evolve into other phases [24]. The strengthening of the IN939 cast alloy is further enhanced by the production of carbides formed during the aging treatment process, precisely two types of carbides develope that are the coarse MC-type carbide, showed in Fig. 3(b), and the finer $M_{23}C_6$-type carbide. These carbides provide strengthening by impeding dislocation motion in the matrix during deformation as well as grain boundary sliding during elevated temperature service, typically at temperature above 0.5 T_m.

In order to provide the appropriate creep properties at temperatures higher than 800 °C and for access to desirable tensile properties in a wide range of temperatures, the heat treatment of the alloy is performed in four-stages, that is known as "standard four-stage heat treatment". The four stages of this heat treatment are as it follows: 1160 °C (4 h)/FAC + 1000 °C (6 h)/FAC + 900 °C (24 h)/AC + 700 °C (16 h)/AC, in which FAC is the abbreviation of 'fast air cooling', and 'air cooling' is abbreviated as AC [24]. The purpose of this treatment is to dissolve the γ' sediments, which occur above 1100 °C and are formed in the matrix during the solidification process. With this 4-stages heat treatment, IN939 achieves good performance at room temperature; however, it has been observed that mechanical properties can be further improved—in particular, yield strength (σ_s) and tensile strength (σ_r)—by introducing a different 3-stages heat treatment with a significantly shorter process time of 14 hours. The following heat treatment involves: 1160 °C (4 h) + 1000 °C (6 h) + 800 °C (4 h).

As for high-temperature creep resistance, it has been observed that the best applicable treatment is the 4-stages process, which includes: 1150 °C (4 h) + 1000 °C (6 h) + 900 °C (24 h) + 700 °C (16 h). This treatment provides an excellent combination of strength and ductility at room temperature, along with good creep properties, ensuring exposure times over 10,000 hours at a temperature of 870 °C. The overall balance of properties is therefore suitable for blade usage [25].

The aforementioned characteristics of the IN939 superalloy are primarily related to properties designed for alloys obtained through casting or forging. In the following paragraphs, however, the typical characteristics of additive manufacturing applied to Ni-based superalloys will be introduced, focusing specifically on the microstructure obtained in IN939 produced by LPBF.

1.9. Metal Additive Manufacturing

Additive manufacturing represents a class of manufacturing using a digital approach to product designing and production, making it a bottom-up process of manufacturing. In contrast to traditional manufacturing which, in most cases, adopts subtractive or formative manufacturing approaches, AM processes, as suggested by the name, allow manufacturing parts by cumulative addition of the material pixel by pixel or/and layer by layer, to realize the shape of interest [23], [26]. Additive Manufacturing of metals is much newer than its polymeric counterpart, it is the process of joining metals in layer-by-layer manner to create a 3D object. One of the main challenges of processing metals in such an additive manner is the requirement of using high temperatures on the metal and then allowing it to solidify rapidly [26]. There are seven different technology families within AM, as defined by the ISO / ASTM 529000:2021 standard [27]. These technologies can be used for many material classes, including metallic materials, polymers and ceramics. For the purpose of this thesis study, laser powder bed fusion (LPBF) of Ni-based superalloys is the technology of relevance.

1.9.1. Laser Powder Bed Fusion: process description

After the 3D CAD model (STL file) is sliced into layers of equal thickness using a relevant software package, the feedstock material in powder form is laid down on a platform in the form of thin layers, typically around 15-45 μm, depending on the material. This thickness corresponds to the thickness of each slice of the STL file prepared for printing [26]. The laser is mounted to a scanner unit which allows extremely precise 2-dimensional patterns to be exposed by the laser beam. The laser has enough power to produce melting of the powder and already deposited material. The powder is spread onto a substrate, known as the building platform, in the form of thin layers, usually from 20 to 100 μm in height. Meanwhile, the part to be manufactured is prepared in the form of 3D model using a CAD software. The 3D model is "sliced" into layers corresponding to the layer thickness to be used by the LPBF process. In Fig. 4 is shown a representation of the general architecture of this system.

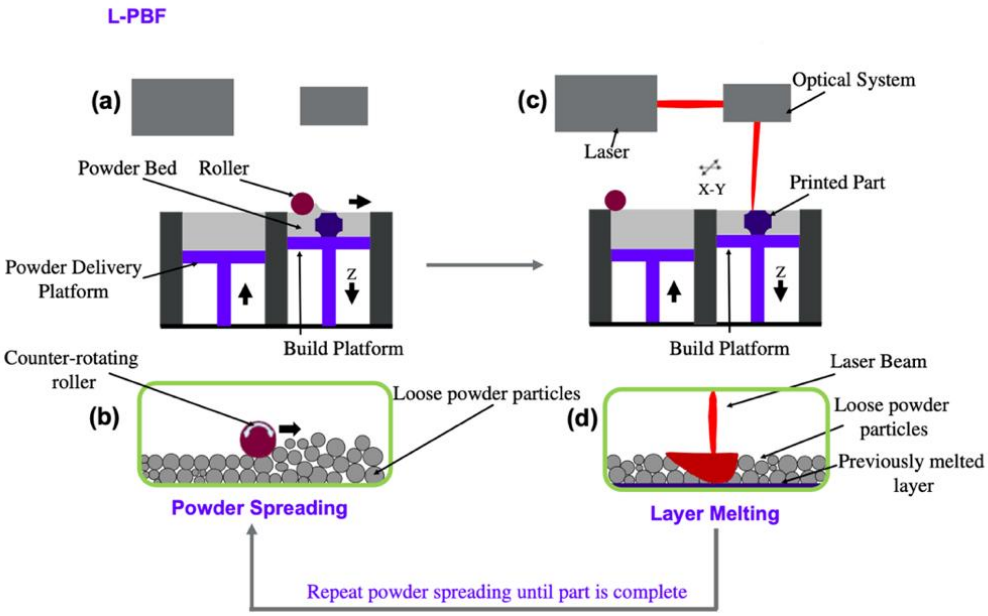

Fig. 4 A schematic of the basic architecture of an L-PBF system demonstrating the technology's operational concept as (A-D) a layer of powder deposited on the build plate and (C and D) a laser beam selectively scanning and melting the regions of interest. Adapted from [26].

Then the 2-dimensional profile of each layer is scanned over by the laser, melting and consolidating the powder as well as fusing it to the building platform, Fig. 4(d). The building platform is lowered by height of one layer, and another layer of powder is spread on top, Fig. 4(c). This layer is also melted by the laser beam according to the slice from the 3D model, and the process repeats until all layers have been processed. This results in a solid part attached to the building platform within a bed of powder. This part is the separated from the building platform by some sawing process, heat treated, and surface treated if required [28]. The entire process must operate under an inert atmosphere to protect the molten metal from oxidation. Therefore, the processing chambers are typically filled with an inert gas, such as argon, nitrogen or helium. The type of gas used has been reported to affect porosity and defect content [29], [30], microstructure [30], [31], [32] and residual stresses [29] to various extents, depending on the material being processed.

LPBF is characterized by high temperature gradients, causing non equilibrium conditions at the solid/liquid interface, thereby leading to rapid solidification as the melt pool undergoes transformation from liquid to solid. Consequently, a wide range of effects are observed, like formation of non-equilibrium phases, ad changes in the general microstructural features, mostly in scale. Finer structures may be observed in the microstructure at sufficiently high

cooling rates compared to the conventional manufacturing method. In addition, it should be pointed out that the grain structure is also controlled by the previously solidified layer grain structure and the SLM processing parameters. This process offers several advantages in comparison to conventional manufacturing techniques, like reduction in production lead time, high flexibility, high efficiency of material consumption and most important possibility to manufacture highly complex intricate components with dimensional accuracy. However, the flip side of the coin is that very short interaction times with rapid heating with highly ionized heat source causes large thermal gradient and thermal stresses. Rapid cooling and solidification of thin layers result in directional grain growth and micro segregation of constituents causes non equilibrium phases [33]. It is important to know that there is a considerable amount of process parameters that play a role in the LPBF process, and the most critical and commonly studied process parameters are illustrated in Fig. 5 [34].

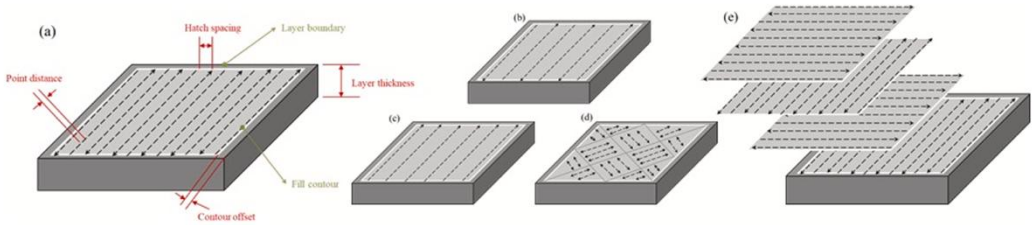

Fig. 5 The geometrical parameters in the SLM process are shown in (a). Examples for the different scan patterns (b-d). A schematic presentation for rotating the scan orientation per layer is in (e). Adapted from [34].

From the above figure, it can be seen that the most impactful and critical parameters are, respectively: laser power, hatch distance (a), scan speed (a), scanning strategy or pattern (b-e), and layer thickness. For this work all samples, that have been analysed and studied, were supplied by Siemens Energy AG and two different machines were used for their production: EOS M290 and EOS M400-1/4. The only thing that differentiates them is in the volume rate, as the EOS M400-4 has four laser beams, hence a larger volume rate, whereas the EOS M290 has a single laser beam. Both machines are equipped with a 400 W ytterbium fiber laser with a laser beam diameter of 100 µm. To prevent oxidation during AM, fabrication was carried out in a protective argon atmosphere.

The generic particle size distribution is 20-55 μm and the nominal chemical composition of EOS powder is listed in Table 3 [35].

Table 3 EOS Nickel-based Superalloy IN939 chemical composition [35]

Powder chemical composition (wt.%)											
Element	Cr	Co	W	Nb	Ti	Al	Ta	Zr	C	B	Ni
Typical	22,5	19	2,0	1,0	3,7	1,9	1,4	0,1	0,15	0,01	Balance

During LPBF three typical types of defects can be induced: lack of fusion (LoF), gas entrapped pores and keyhole pores. LoF is generated by the lack of overlap between laser hatches or by insufficient energy input. Keyhole pores appear when the laser power is high enough to cause evaporation of metal at the bottom of melt pool. Gas pores originate from bubbles of inert gas entrapped in the melt during fusion of the powder bed and/or from gas entrapped inside the feedstock material. Numerous studies on the process optimization have been conducted. They aimed at reducing the amount and volume of defects resulting from LPBF. However, even parts produced with optimum parameters sets may contain some gas entrapped porosity. Post-processing heat treatment (HT) is a vital step in the metallic AM production chain and is routinely used in industrial environments. Solution or stress relieving HTs are usually applied to stabilize the microstructure and alleviate the high residual stress after manufacturing. However, heat treatment is not able to eliminate defects, and therefore, they remain one of the key challenges limiting the use of AM parts in critically loaded components [36].

1.9.2. Microstructure of IN939

As mentioned before, the LPBF process consists in multiple laser scanning. The process generates a microstructure in which the laser tracks can be identified in the XY plane, perpendicular to the building direction (BD). These tracks, when seen on planes which are parallel to the BD (XZ and XY), appear as melt pools. Dimensions, shape and position of the melt pools can vary changing the process parameters and the scanning strategy [37], [38], [39]. An example of the different grain appearance on the XY and XY planes for the LPBF produced IN939 is reported in Fig. 6.

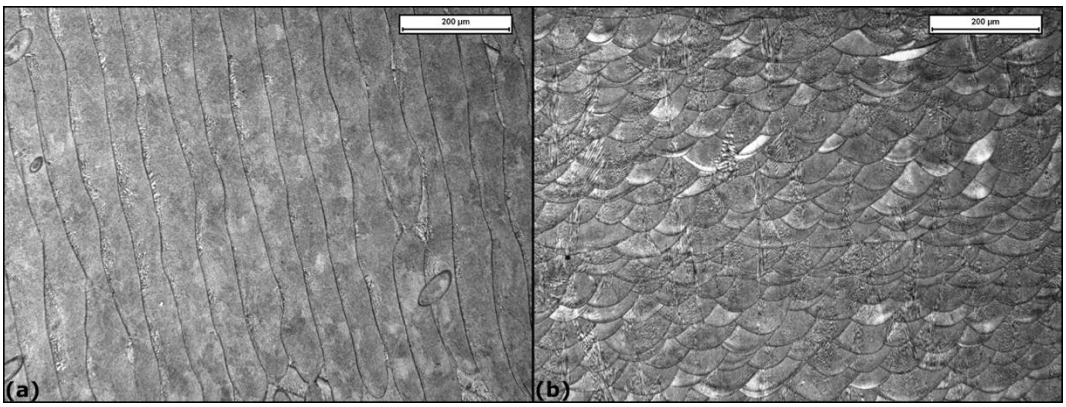

Fig. 6 (a, b) Optical micrographs of as-cast sample at 90° specimen with (a) perpendicular and (b) parallel to the build direction.

Dendrites growing along the build direction are clearly visible in sections parallel to the building direction, look at Fig. 7(b), and arrays of sub-micron sized particles at the interdendritic regions could be seen.

In sections perpendicular to the building direction, Fig. 7(c), the dendritic core and interdendritic region can be distinguished, and several small particles with various morphologies are visible at the interdendritic region [40].

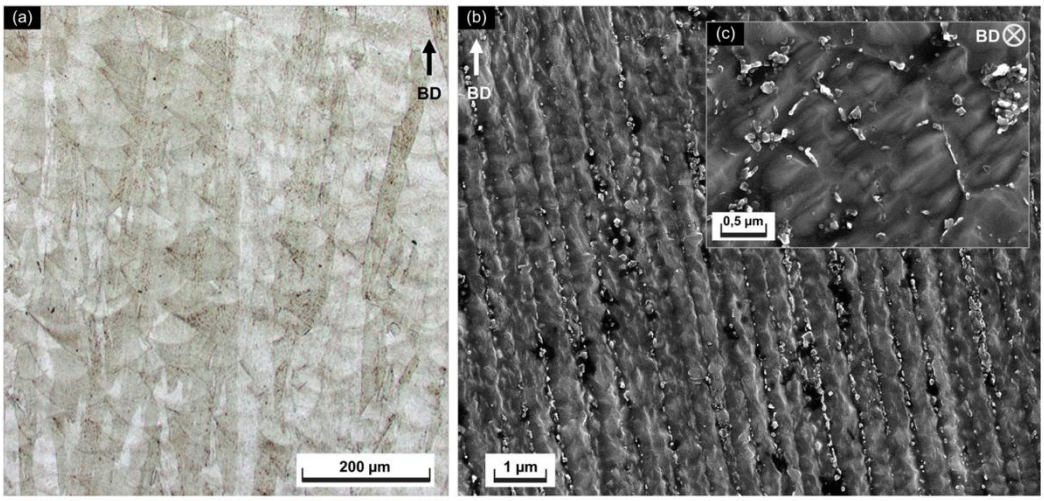

Fig. 7 Microstructure of IN939 in the as-built condition, (a) optical micrograph, (b, c) SEM micrographs with secondary electron detector. Kalling's 2 etch. Adapted from [40]

When the laser beam creates the melt pools, the columnar grains tend to be formed along the thermal flux orientation (towards the building platform). The majority of the grains grow along the z-axis, even though the overlapping between consecutive melt pools can give birth to smaller grains with different orientations. The melt pools are composed of fine dendritic/cellular architectures (Fig. 8a, b); the dendrites are characterized by sub-micrometric dimensions [41]. The extremely small dimension of these dendrites is caused by the extremely high cooling rate experienced by the alloy during the LPBF process (10^4 to 10^6 K/s). High-magnification views (Fig. 8c, d) reveal the presence of sub-micrometric precipitates with largest ones mainly located along the columnar grains. These precipitates are most likely to be MC carbides and γ' precipitates.

For Ni-based superalloys, the presence of interdendritic areas characterized by chemical segregations can influence the formation of the phases under heat treatments, promoting a different microstructure evolution with respect to the traditional conditions, i.e., casting or wrought states [42], [43], [44]. The formation of larger precipitates along the interdendritic areas is associated with the solidification process [41].

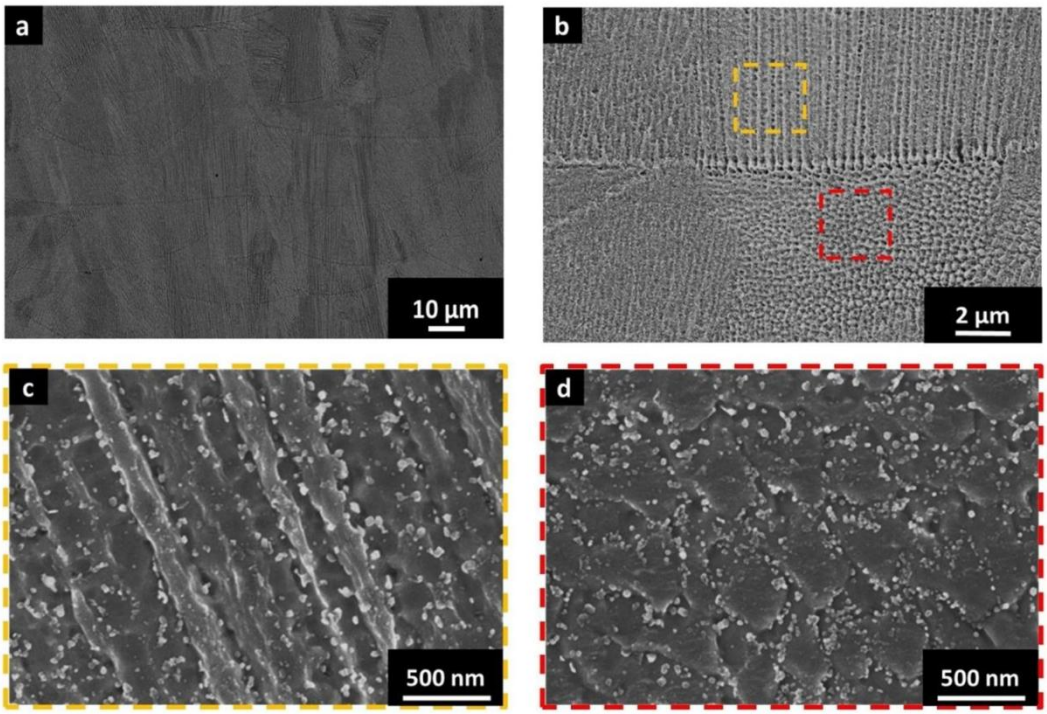

Fig. 8 (a, b) SEM images of the LPBFed IN939 showing the melt pools; (c, d) High-magnification SEM images showing fine dendritic/cellular architectures. Kalling's No.2 etchant was used [41].

1.10. Heat Treatments in Ni-based Superalloys

In industry, almost all functional AM parts are post-processed using heat treatment (HT). HT allows the modification of the microstructure through controlled heating and cooling of materials. By modifying the microstructure, materials can obtain enhanced mechanical properties [45]. Indeed, performance of AB material is poor because of surface integrity defects and unfavourable microstructural formation with secondary phases such as Laves phases. SLM processing has also been shown to strongly influence γ' precipitation behaviour. Due to very high cooling rate encountered during the solidification of SLM processed materials, post-SLM heat treatments are necessary to develop γ' precipitates with the desired size. Additionally, heat treatment may also be necessary to relieve the residual stresses generated because of differential thermal contraction of successive layers during deposition [46]. Hence, HTs are used to increase grain size [47], to obtain a more equiaxed microstructure and dissolve detrimental phases, like Laves phases [48], to form strengthening precipitates such as δ-phase, γ' and γ" [50,51], and to remove defects [49] in order to improve mechanical properties.

Another important aspect about HT concerns the mitigation of crystallographic anisotropy, a typical phenomenon found in LPBF components. However, according to the large amount of experimental investigations, the LPBF processed nickel-based superalloy shows very sluggish recrystallization kinetics. Generally, the static recrystallization temperature of the nickel-based superalloy is in the range of 1000-1100 °C and under this temperature, recrystallization will gradually take place. Nevertheless, the grain structure remains very stable below the "recrystallization" temperature, and then turned to a near-fully recrystallized condition when the post-processing temperature reaches an extremely high but uncertain temperature (super-γ'-solvus temperature for LPBF IN939).

1.10.1. Typical heat treatments for Ni-based superalloys

The heat treatments typically used on a variety of superalloys are given in Table 4; as it can be seen from this table, heat treatment can range from very simple schemes for solid-solution-hardened alloys, to the most complex procedures for advanced single-crystal alloys [16].

Table 4 Common superalloys heat treatment. Adapted from [16].

Alloy	Alloy type	Solutioning(a)	Aging(a)
A-286	Wrought, Ni-Fe	980 °C/1 h/OQ	720 °C/16 h/AC
Discaloy	Wrought, Ni-Fe	1010 °C/2 h/OQ	730 °C /20 h/AC + 650 °C/20 h/AC
N-155	Wrought, Ni-Fe	1175 °C/1 h/WQ	815 °C/4 h/AC
Astroloy	Wrought, Ni	1175 °C/4 h/AC + 1080 °C/4 h/AC	845 °C/24 h/AC + 760 °C/16 h/AC
Inconel 901	Wrought, Ni	1095 °C/2 h/WQ	790 °C/2 h/AC + 720 °C/24 h/AC
Inconel 625	Wrought, Ni	1150 °C/2 h/RQ	…
Inconel 713	Cast, Ni	Used in as-cast condition	…
Inconel 718	Wrought, Ni	980 °C/1 h/AC	720 °C/8 h/FC + 620 °C/8 h/FC
Inconel 718	Cast, Ni	1095 °C/1 h/AC	955 °C/1 h/AC + 720 °C/8 h/FC + 620 °C/8 h/AC
Inconel 738	Cast, Ni	1120 °C/2 h/AC	845 °C/24 h/AC
Nimonic 80A	Wrought, Ni	1080 °C/8 h/AC	705 °C/16 h/AC
Waspaloy	Wrought/cast, Ni	1080 °C/4 h/AC	845 °C/24 h/AC + 760 °C/16 h/AC
Haynes 25	Wrought, Co	1230 °C/1 h/RAC	…
Haynes 188	Wrought, Co	1230 °C/0.5 h/RAC	…
S-816	Wrought, Co	1175 °C/1 h/RQ	760 °C/12 h/AC
CMSX-2	Cast, Ni (single crystal)	1315 °C/3 h/GFQ	980 °C/5 h/AC + 870 °C/20 h/AC
PWA-1480		1290 °C/4 h/GFQ	1080 °C/4 h/AC + 870 °C/32 h/AC
CMSX-10	Cast, Ni (single crystal)	1316 °C/1 h + 1329 °C/2 h + 1327 °C/2 h + 1340 °C/2 h + 1346 °C/2 h + 1352 °C/3 h, 1357 °C/3 h + 1360 °C/5 h + 1363 °C/10 h + 1365 °C/15 h	1152 °C/6 h/AC + 871 °C/24 h/AC + 760 °C/30 h/AC

(a) AC = air cool, FC = furnace cool, GFQ = gas furnace quench, OQ = oil quench, RAC = rapid air cool, RQ = rapid quench to below 540 °C, WQ = water quench. Source: Ref 1, 37

Heat treatment procedures for nickel-based superalloys are applied to achieve chemical homogenization and to control the grain structure. Heat treatment is an important method for modifying the morphology of the precipitates in superalloys and they can be divided in 4 types, according to the time and temperature condition and to the objective of the treatment.

a) Stress Relieving Treatment

This heat treatment is performed on superalloys in order to reduce the stress carried by the material after the fabrication process. Temperatures used in this treatment are usually below the annealing or recrystallization temperatures, in order to avoid microstructural changes. The time and temperature cycles for stress relief may vary considerably, depending on the metallurgical characteristics of the alloy and on the type and magnitude of residual stresses developed by previous fabricating processes. Generally, temperatures for Ni-based superalloys, vary between 675 °C and 900 °C and with dwell times between 1 and 4 hours [50].

b) Annealing Treatment

Annealing treatment is generally applied to a superalloy at a temperature which starts grain growth and recrystallization mechanism, leading to a lower hardness of the material and to an increase in ductility to facilitate forming or machining. It also prepares the material for welding, relieves stresses after welding or soften age-hardened structures by resolution of second phases [50]. An annealing treatment can lead to different results based on the condition of:

- Reduction of the internal stress of the alloy.
- Homogenization of a cast microstructure.
- Improvement of the ductility and reduction of the hardness, improving workability.
- Dissolving part of the phases.

c) Solution Treatment

Solution heat treatment is performed at higher temperatures compared to stress relieving and annealing treatments, arriving near to the incipient melting temperature of the alloy. These temperatures may range from about 980 °C to 1230 °C. The main

goal of this treatment is intended to dissolve second phases to produce maximum corrosion resistance or to prepare an alloy for subsequent aging. The high temperature needed to the precipitate dissolution creates also the condition for the maximum elemental diffusion, homogenizing the alloy composition, removing the segregations present after the solidification and improving creep-rupture properties by increasing grain size [51], [52]. Each superalloy has its own solution treatment temperature and treatment time, and it is necessary to consult the datasheets for each material.

d) Precipitation hardening (aging) treatment

Aging treatments strengthen age-hardenable alloys by causing the precipitation of additional quantities of one or more phases from the supersaturated matrix, that is developed by solution treating. The common phases desirable for develop optimal mechanical properties are precipitates such as γ', γ" and secondary carbides. In the case of Ni-based superalloys, γ' and γ" have been observed to precipitate from the γ matrix when subjected to double aging treatment in the range of 600-900 °C [53]. Compared to the treatments described above, the ageing treatment requires much longer process times and can be divided into several steps [51].The main purpose of these complex treatments is to stabilize specific phases which, during the application of the material at high temperatures, can turn into other phases that deteriorate the mechanical and corrosive properties. Some examples are the transformation of γ' → η and γ" → δ and $M_{23}C_6$ growth.

1.10.2. Different type of treatment: Hot Isostatic Pressing

In the field of superalloys, hot isostatic pressing (HIP) has been used in powder metallurgical applications to densify the materials and, for single crystals, to reduce the porosity generated during the casting and homogenization processes. The main parameters are temperature, pressure and time. Several studies reveal that the internal porosity of laser consolidated, laser deposited and SLM processed parts made from different powder materials, is strongly reduced by means of HIP and thus the mechanical properties are enhanced. In addition to porosity reduction, the application of HIP enables a certain degree of homogenization of the alloy composition due to the high HIP-treatment temperatures. Some heat treatment schemes prefer the use of HIP after casting, in order to reduce the magnitude of the casting porosity.

HIP treatment involves the simultaneous application of high temperature and isostatic pressure to a workpiece. The used pressure medium is an inert gas such as argon or nitrogen, which is pumped into a pressure vessel and pressurised to up to 200 MPa, whilst a furnace in the vessel produces temperatures up to 2000 °C [54].

Normally, HIP post-processing is recommended to improve the fatigue resistance of LPBF parts. Even though HIP cannot completely remove porosity, it significantly decreases the defect population and its average size below the critical threshold value, leading to early crack initiation. This fact allows HIPed materials to reach fatigue performances similar to those of wrought alloys. For this thesis work, however, HIP treatment has been used, exceeding the solidus temperature of the IN939 superalloy and thus entering the field of incipient melting of the material. However, thanks to the action of high temperature, which allows a complete solubilisation of the γ' present in the As-built sample, but also increase the internal porosity due precisely to the continuous development of incipient melting, and the action of high isostatic pressure applied, it will be possible to mitigate the development of liquid zones and, at the same time, obtain an increase in grain size. This will produce a material with a large grain size and a decrease in porosity compared to the as-built material.

1.11. Incipient melting

As mentioned in the previous paragraphs, the main element present in superalloys is nickel, which has a melting temperature of 1453 °C. It is also known that the presence of other alloying elements, such as Cr, Mo, W, and Ti, leads to a variation in this melting temperature. In fact, a range of temperatures must be taken in consideration. The issue arises due to the presence of eutectic phases, that melt at lower temperatures respect to the main melting point; incipient melting is defined as the temperature range at which a liquid phase starts to form within the alloy, i.e., when any low-melting phases contained in the material, begin to melt. It has been observed that, according to Cormier and Gandin [55], the occurrence of incipient melting, during solution treatment, becomes a problem for nickel-based alloys with a high content of refractory elements such as Re, W, Ta, and Mo. Indeed, increasing the content of such elements leads to a higher degree of chemical segregation, resulting overall in a lower temperature for incipient melting in interdendritic spaces, while the solvus temperature of the γ' phase increases. Essentially, the heat treatment "window" becomes quite narrow if one wishes to dissolve as much of the γ/γ' eutectic pools as possible without reaching incipient melting. Another definition that can be given for incipient melting is the following: it is the melting that occurs in some part of the alloy that, when solidified, is not at the equilibrium composition and thus melts at a lower temperature than that at which it might otherwise melt [56]. Nickel-base superalloys may show incipient melting at temperatures as low as 1204 °C. Referring to the IN939 superalloy considered for this work, the solidus temperature has been reported at 1235 °C, temperature related to the material produced by LPBF, and which corresponds to the starting point of the general melting of the alloy. Jahangiri et al. showed the practical incipient melting temperature of the IN939 superalloy was around 1125 °C and 1150 °C. Furthermore, the segregation of alloying elements including B and Zr can promote the incipient melting phenomenon in Ni-base superalloys during solution treatment or welding [57].

Chapter 2

2. Materials and Methods

2.1. LPBFed IN939

The material covered in this thesis work is, as mentioned in the previous paragraphs, the nickel-based superalloy Inconel® 939, supplied by Siemens Energy, and the chemical composition previously reported in paragraph 1.8. Siemens has produced the following cylinder samples by laser powder bed fusion, using the EOS M290 or EOS M400 ¼ machine, shielding gas composed of Argon, layer thickness between 20 and 40 μm and typical wall thickness of 0.3 – 0.4 mm. All this L-PBF process parameters are based on Siemens internal developments.

2.2. Metallographic preparation of samples

The starting point of this work was to determine the volumetric porosity of the samples supplied by Siemens after being processed via LPBF. To do this, it was necessary to prepare the IN939 samples metallographically. The samples were originally cylindrical in shape with a diameter of 14 mm and a height of 120 mm. To carry out a porosity investigation along the two main building directions, plane XY and plane XZ, it was necessary to divide a single starting cylinder into several smaller cylinders (approx. 20 mm height each) using a disc saw. Then, the small cylinder was divided in two parts and the cuttings, shown in Fig. 9, were performed parallel to the building direction (Z) in order to see the XZ plane and perpendicular to the building direction (Y) to see the XY plane.

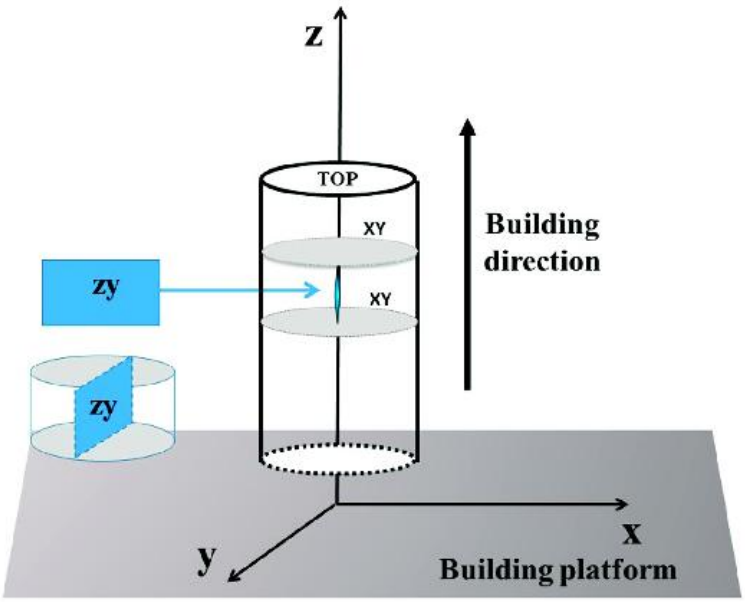

Fig. 9 Schematic representation of the as-built IN939 cylinders built along the building direction; the x-y plane is perpendicular to the building direction, while the x-z plane is parallel to the building direction.

In particular, three samples were considered from three different positions: the top, the centre and the tail of the cylinder. Afterwards, the samples were embedded in 20ml phenolic resin and treated at 155 °C for a process duration of 30 minutes. After embedding, the samples were polished with special paper from a grit size of 180 up to 2400. To finish, the samples were lapped using colloidal silica pastes in 3 different steps, from a suspension of 6 µm, then 3 µm and finally to 1 µm. Once the light microscope analysis was performed, the samples were attached with Kalling No.2; this enabled the SEM examination and sample grain size calculation.

2.3. Specimen Analysis

2.3.1. Optical Microscope

After embedding the samples, they were analysed using the Leica MEF4 optical microscope in incident light mode and without polarized lenses, at magnifications varying between 50x and 200x. For the As-Built samples, 10 images from the core and 5 images from the surface of the samples, were collected for the XY and XZ planes, respectively. After collection, the images were processed and analysed using the open-source software ImageJ. The software is capable of creating binary images, i.e. pictures with just two colours:

- White, which represents defects, porosities and eventually cracks.
- Black, which corresponds to dense material.

Using ImageJ, it is also possible to distinguish among gas defects, lack of fusions or cracks. This is done by calculating the aspect ratio of the individual defects: the aspect ratio is calculated as the ratio of the largest diagonal to the smallest diagonal of the smallest ellipse surrounding the defect. If the ratio of these two values equals 1, this means that the defect has a perfect spherical shape and can therefore be attributed to a gas porosity. On the other hand, the higher the ratio, the more the defect is elongated in a certain direction, i.e. it is more elliptical. Another considered parameter is the Feret's diameter, this represents the distance between the two parallels tangent to the perimeter of the area projected by the defect. Lastly, the % Area parameter was also taken into account, which represents the percentage of the total area of the defects within the image.

2.3.2. Scanning Electron Microscopy (SEM)

The samples were etched and then examined using a Zeiss Evo 15 Scanning Electron Microscope (SEM). By this instrument, fine detail of the microstructure was assessed with particular attention to γ' and the carbides. Additionally, an EDS probe was used to gain a compositional assessment of specific phases. Focusing more on the used procedure, images were taken with both secondary and backscattered electrons and at magnifications varying between 5Kx and 20Kx.

2.4. Grain Size Analysis

Kalling etchants were used for grain size calculation as well. Five photos were taken for each sample, and ImageJ software was used for the analysis. The average grain size was calculated using ASTM E112-13 (2021). The procedure can be divided into several steps, that are shown below:

- Three main diagonals were sketched, and their relative lengths were calculated.
- The number of grains were calculated, counting how many times the diagonal crossed a grain. When the line crosses the grain twice, the grain is considered as a whole, when the line crosses a grain only once, it is counted as a half.

- A value is obtained by taking the ratio of the diagonal's length to the number of grains counted. Then, this value is compared to those ones in the table provided by the standard, in the mean intercept's column. Intermediate values were obtained via a linear interpolation among the values contained in table 4 of the ASTM E112.
- The mean intercept was used to calculate the G value.

2.5. Differential Scanning Calorimetry (DSC)

Some important temperatures of the material, such as the solidus temperature and the incipient melting temperature region, can be determined with differential scanning calorimetry (DSC). DSC was used on the As-Built samples to figure out these temperature values. The test was conducted in a Setaram DSC/TGA furnace on a specimen of 50 mg, starting from 20 °C up to 1350 °C. Both heating and cooling were performed with a scan rate of 20 °C/min.

2.6. Air-furnace Heat Treatment

Through DSC, it was possible to determine the temperature range in which incipient melting occurs. However, the DSC test alone cannot definitively establish the temperatures at which liquid-phase zones begin to form. To address this issue, five tests were conducted in a static air furnace at temperatures ranging from 1270 °C to 1300 °C, with an operational duration of 1 hour, followed by air cooling, taking into account the results obtained from the DSC test. The fifth test, however, was conducted at the solubilization temperature of IN939, which is 1160 °C, also this one for 1 hour, with subsequent air cooling. This temperature is usually preferred to heat treated IN939 obtained with traditional casting or forging for annealing. Consequently, this heat treatment is useful for understanding how the material behaves at the given temperature, particularly to determine whether solid-state diffusion phenomena leading to grain recrystallization might begin or not.

2.7. DOE, Taguchi Method and Minitab

As reported in literature, hot isostatic pressing can effectively reduce microstructure defects, such as micropores and thus further improve the high temperature performance of nickel-based superalloys. However, it continues to be a very costly procedure. Therefore, a specific

strategy known as Design of Experiment (DOE) was employed in order to minimize the number of experiments while also accelerating the experimenting process. The design of experiments is a tool for planning, designing and analysing the experiments, so that valid and objective conclusions can be drawn efficiently and effectively from results of the experiments. The Taguchi method is one of the types of design of experiment that exists and was developed by Dr. Genichi Taguchi. This method investigates how different parameters affect the mean and variance of a process performance characteristic that defines how well the process is functioning. The process-influencing parameters and the levels at which they should be varied are arranged using orthogonal arrays. The Taguchi approach tests pairs of possibilities rather than needing to test every conceivable combination, as the factorial design does. This saves time and money by enabling the gathering of the data required to identify the elements that have the biggest effects on product quality with the least amount of experimentation [58].

In order to set all the necessary parameters for the DOE, it was necessary to use Minitab software. Minitab is a software used for data analysis. It is extensively utilized in many different sectors, including industry, education, and healthcare. Minitab provides users with tools to perform statistical analysis, including hypothesis testing, regression analysis, and especially the standard statistical technique called analysis of variance (ANOVA), that is routinely used to provide a measure of confidence. This technique does not directly analyse the data but rather determines the variability (variance) of the data [59].

It also offers a number of graphical features to assist users in visualizing data. For an optimal analysis, the 3 main parameters of HIP process, namely temperature, pressure and time, were set by the software, and for each parameter 3 values were given. Then the software provided a total of 9 trials as an answer, given by the combination of each parameter with the values.

Chapter 3

3. Results and discussion of IN939

3.1. Microstructural evaluation of IN939 As Built

Fig. 10 and Fig. 11 show the microstructure of the as-built samples of IN939. The following images are representative of the top and bottom sections of the sample and, for each section, two building directions: XY and XZ. What can be observed is the presence of various defects within the microstructure.

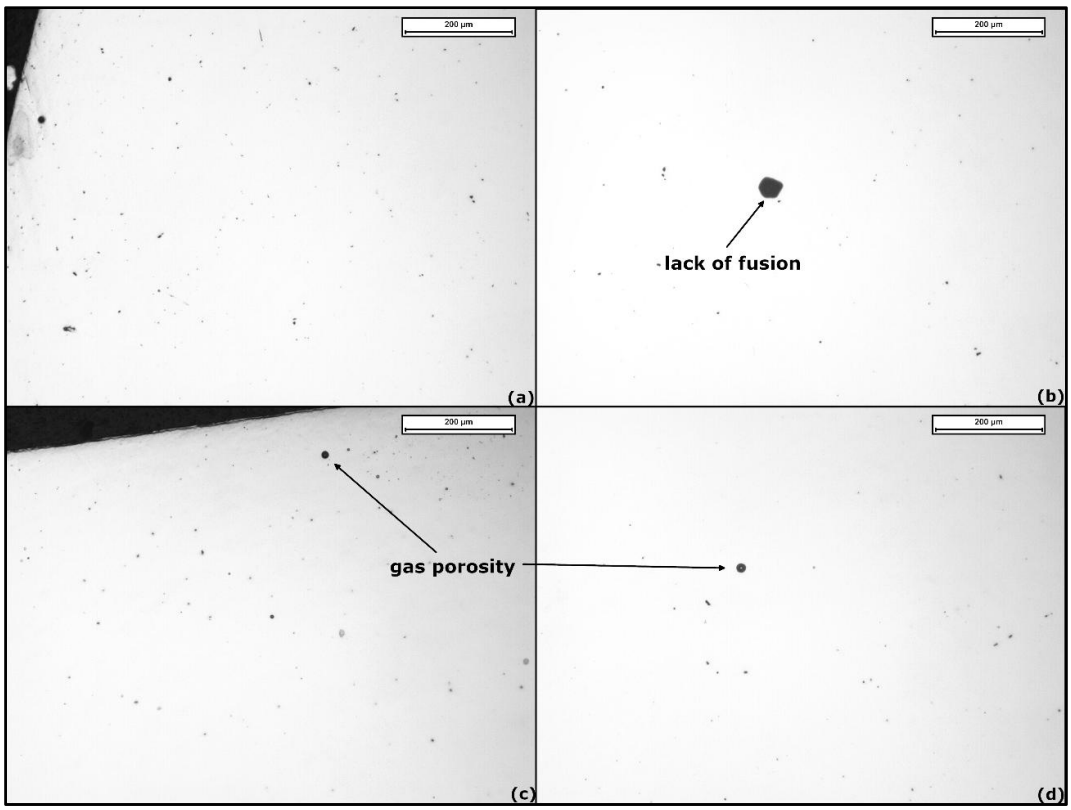

Fig. 10 Optical microscope image of top sample of IN939: (a) Surface XY, (b) Core XY, (c) Surface XZ, (d) Core XZ

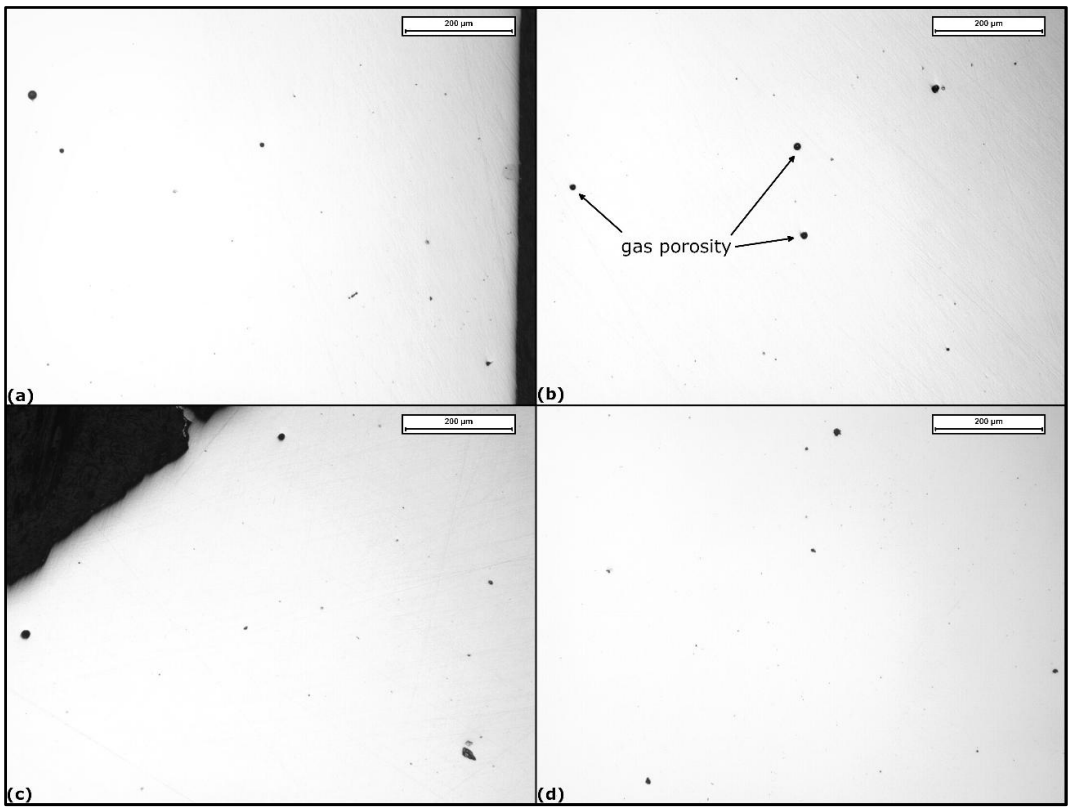

Fig. 11 Optical microscope image of bottom sample of IN939: (a) Surface XY, (b) Core XY, (c) Surface XZ, (d) Core XZ

In the as built specimens of IN939, the most frequent defects are lack of fusions, shown in Fig. 10(b) and gas porosities, shown in Fig. 11(b). From the analysis of the 3 initial samples, it was possible to determine the concentration and morphology of these defects present, in particular residual porosity and aspect ratio data were collected. The aspect ratio and residual porosity data are shown in the figures here below. The maximum density of data is found in the 1.1 – 1.3 class, which indicates that the majority of the porosities present are spherical in size or just slightly vary from spherical, according to the aspect ratio histograms displayed in Fig. 12. Both building planes XY and XZ exhibit this behaviour as well.

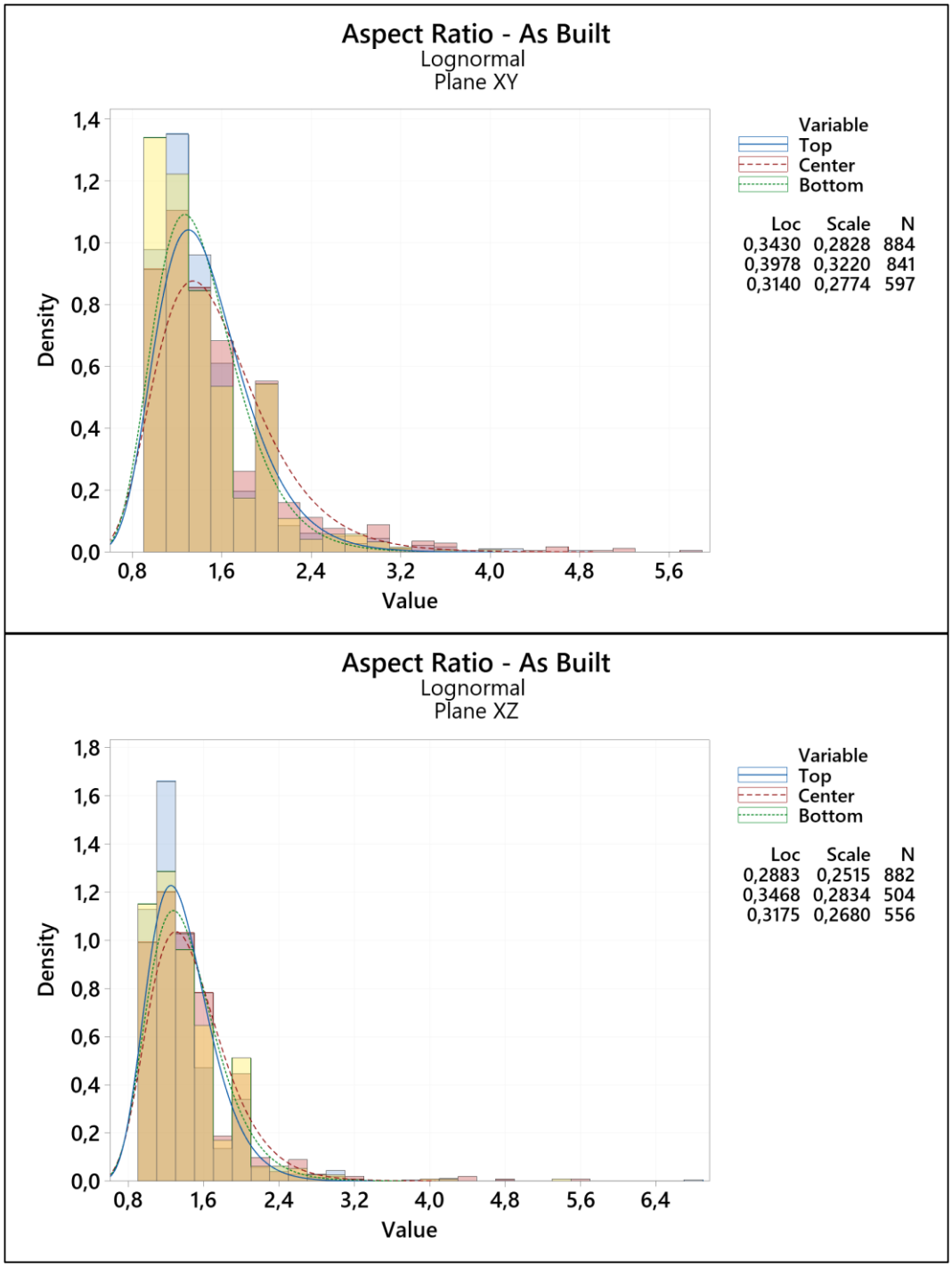

Fig. 12 Aspect ratio histogram of the as-built IN939 sample in the three sections: Top, Centre and Bottom

Fig. 13 displays the residual porosity, which is represented by a boxplot graph. This graph shows that, with a few small exceptions, the residual porosity measured values range from 0.05 to 0.1%, indicating that the material, in the three sections considered, has an

exceptionally high density, and also that overall, the defect is homogeneously distributed throughout the material.

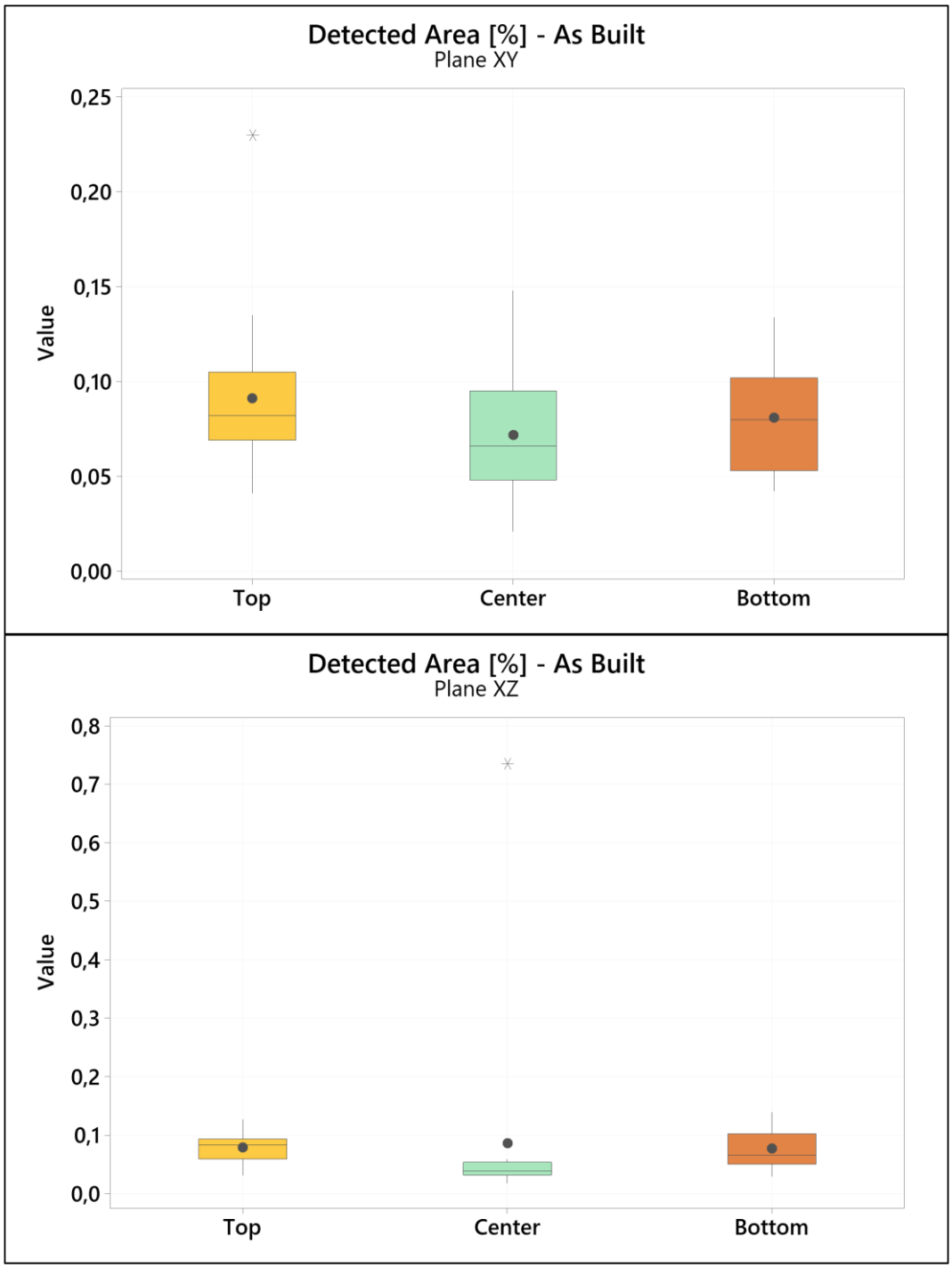

Fig. 13 Residual porosity boxplot of as built samples in the three sections: top, centre and bottom in the XY and XZ plane

After being etched, the samples exhibit the usual microstructure of AM grains made by LPBF. Two features in particular are seen in Fig. 14(a), where the various laser pathways are visible in the XY plane, which is perpendicular to the building plane. In contrast, the XZ plane, parallel to the building direction, is depicted in Fig. 14(b), where columnar grains elongated along the building direction are visible, together with a fine dendritic microstructure. Finally, melt pools typical of the AM building process could be seen in the XZ plane, too.

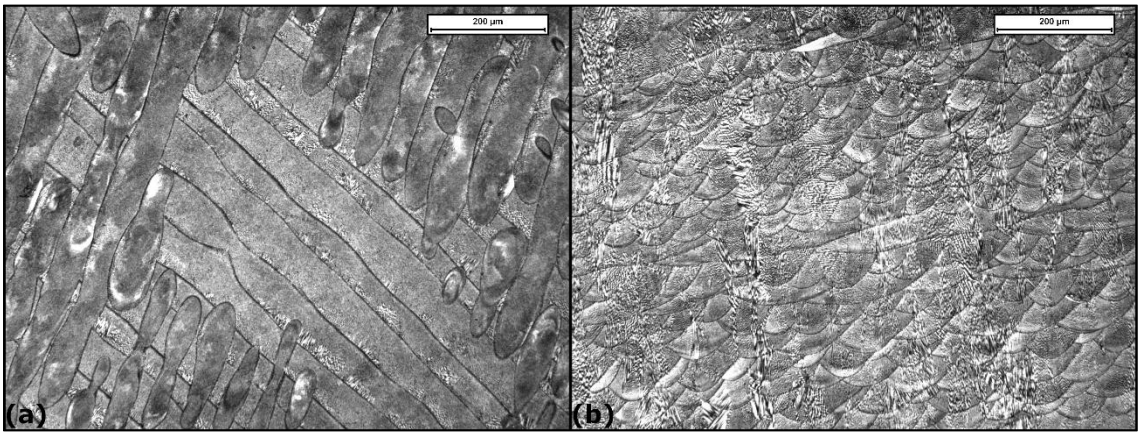

Fig. 14 Grain microstructure of as built sample: (a) Bottom sample, XY-plane (b) Head sample, XZ-plane

To conclude the analysis of the as-built specimens, Fig. 15 shows the analysis conducted by SEM, in which the microstructure was observed at higher magnifications. Fig. 15(a) confirms the presence of melt pools, which were composed of fine dendritic/cellular architectures. The dendrites were characterized by sub-micrometric dimensions. Fig. 15(b), obtained with backscattered electrons, shows the presence of brighter regions that may be related to the segregation of heavy elements, such as Ta and Nb. This may be linked to the high cooling rate, that did not allow them to form carbides or other different phases. From Fig. 15(c) it is possible to observe no preferred directions in the dendrite growth, in fact this aspect illustrates the anisotropic microstructure resulting from the laser powder bed fusion process. To conclude, Fig. 15(d) shows dendrites growing along the build direction, clearly visible in sections parallel to the building direction.

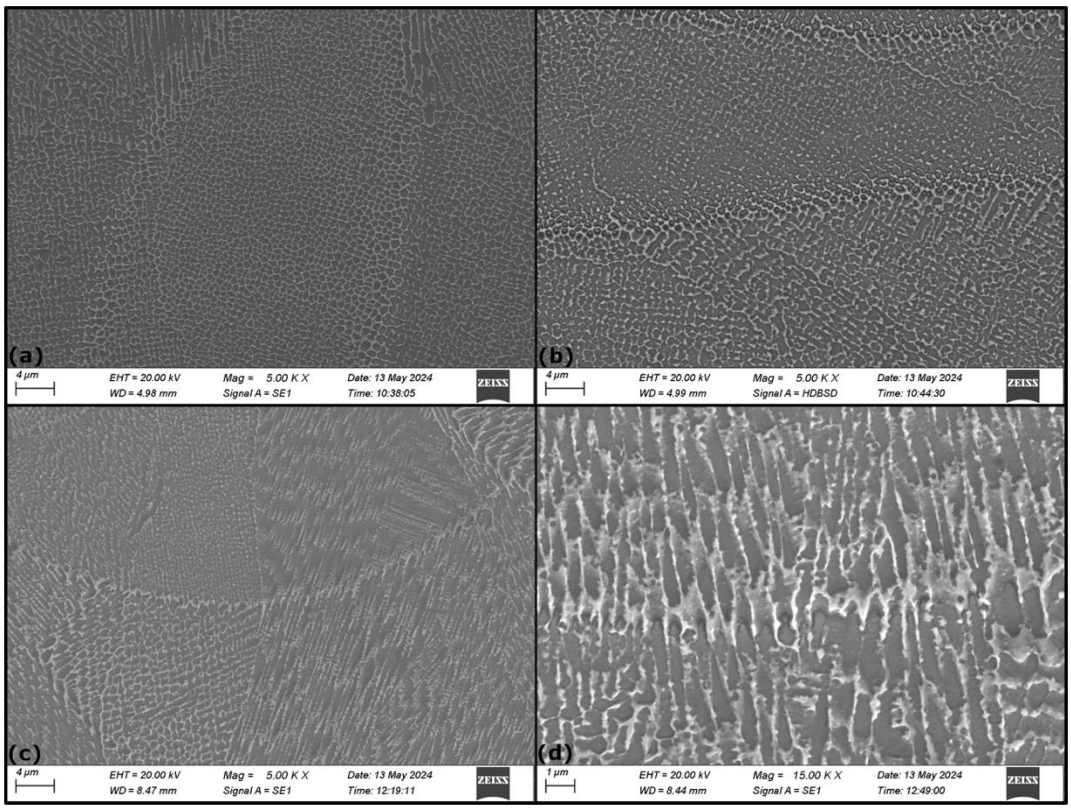

Fig. 15 SEM images of as-built LPBF IN939 specimens

3.2. Microstructure of air furnace heat treated specimens

As showed in the previous chapter, specimens were examined after either standard solution treatment or non-standard heat treatments after assessing the as-built specimens. Initially, the DSC research was carried out to comprehend the IN939 microstructure and liquid formation evolution from room temperature to melting. The DSC heating curve, which is displayed in Fig. 16, indicates that IN939 achieves its solidus point at 1274 °C. As this temperature is overcome, the amount of liquid formed increases considerably. On the other hand, by observing the cooling curve (in blue) it is possible to see the solidification and the formation of MC carbides. The two peaks tend to overlap, and a deconvolution calculation would be beneficial to locate them separately.

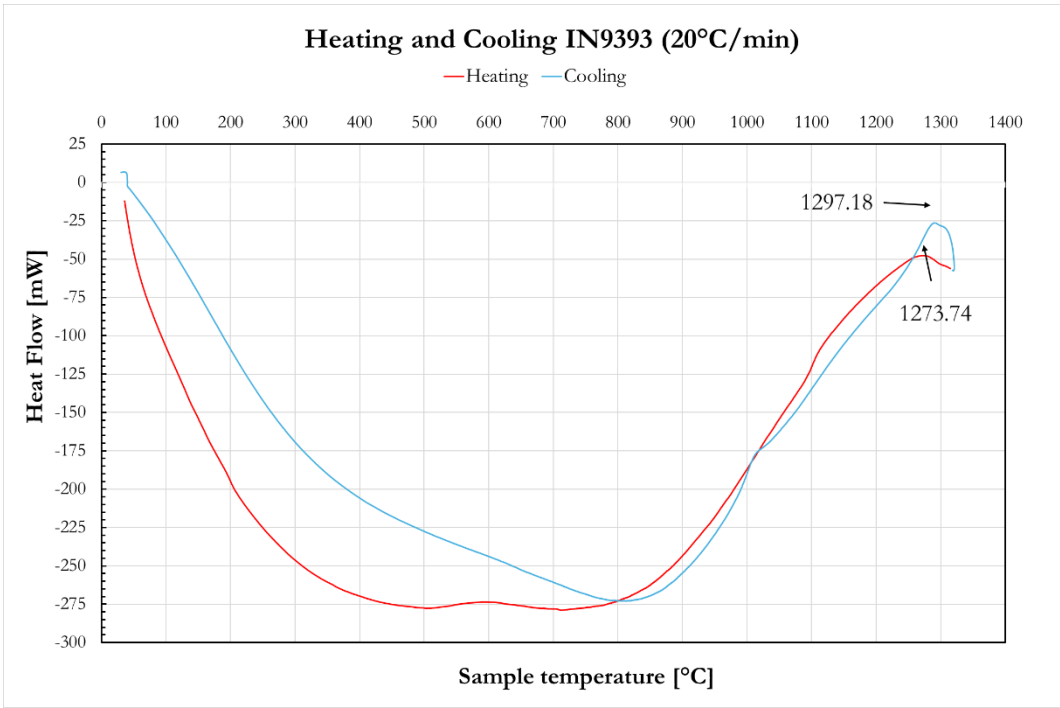

Fig. 16 DSC cooling and heating curves for IN939

However, additional tests were required before performing HIP. More specifically, five heat treatments were conducted, the first at the standard solubilization temperature at 1160 °C and the other four non-standard heat treatments through a working window between 1270 °C and 1300 °C. These heat treatments were performed into an air furnace without considering any effect brought by HIP pressure. For this reason, further heat treatments will be needed to understand if pressure may have any effect during the heat treatment of IN939. In other words, these heat treatments had the main scope of verifying at which temperature the liquid to develop.

3.2.1. Standard solution heat treatment

First of all, the results obtained from the standard solution treatment are reported. Observing Fig. 17, it is possible to see that small defects are always present which can be attributed to gas porosity or failed castings, but in addition to this, the appearance of the first extremely fine-sized carbides can be noted.

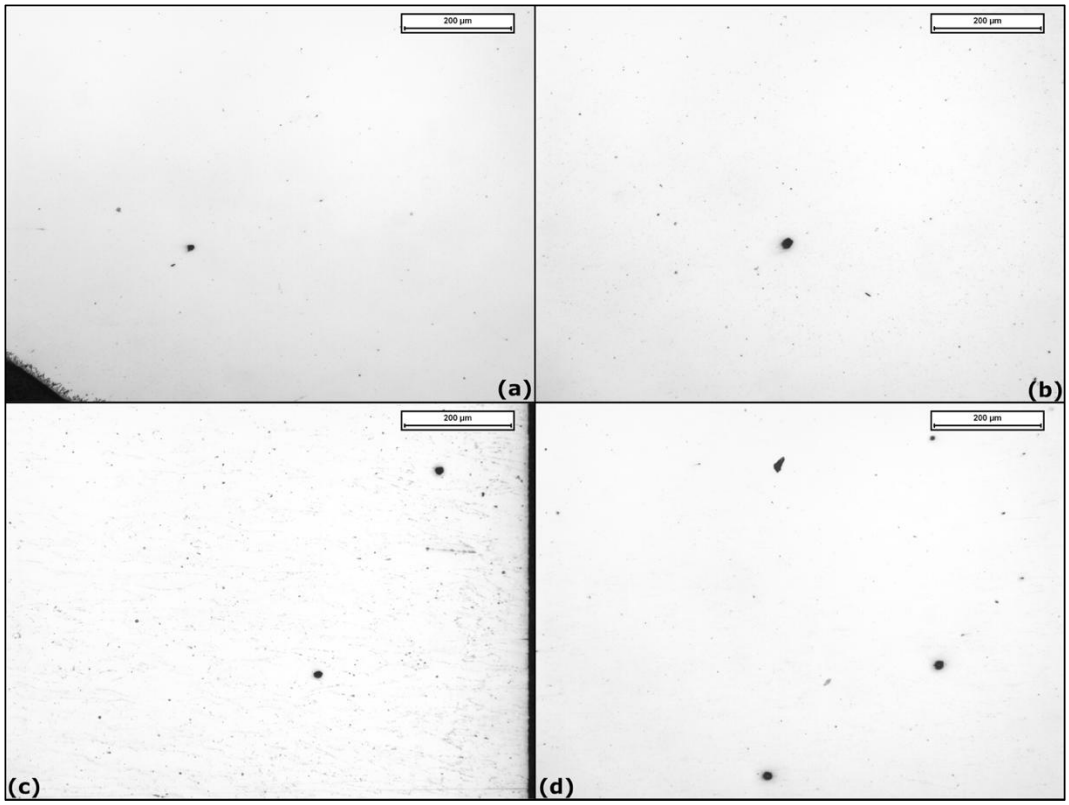

Fig. 17 Optical microscope image of solution heat-treated sample of IN939: (a) Surface XY, (b) Core XY, (c) Surface XZ, (d) Core XZ

Table 5 shows the results for average aspect ratio, residual porosity and defect diameter of the specimen. Note how the specimen surface, for both the XY and XZ planes, has a higher percentage of residual porosity than the core.

Table 5 Solutioning heat treated sample defect analysis summary

Solubilized sample	Av. Defects diameter [µm]	St. Dev.	Av. Vol. Porosities [%]	St. Dev.	Av. Aspect Ratio	St. Dev.
Surface XY	1.872	2.420	0.084	0.054	1.566	0.655
Core XY	2.318	2.837	0.045	0.018	1.496	0.558
Surface XZ	2.242	2.831	0.091	0.042	1.707	1.006
Core XZ	2.724	3.508	0.044	0.031	1.698	1.025

The aspect ratio, as depicted in Fig. 18, is still comparable to the specimens as built. In fact, from the peaks in the histogram, the class with the highest density of values is between 0.75 and 1.25; both in XY and XZ planes.

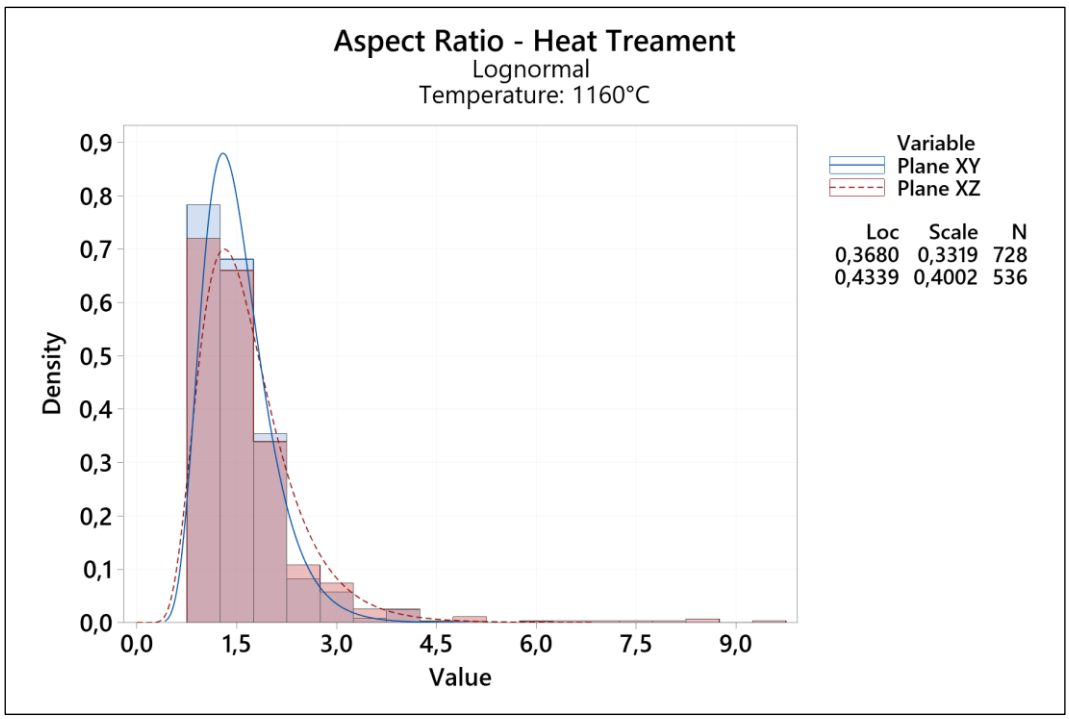

Fig. 18 Aspect ratio histogram of the solution heat-treated IN939 sample in the XY-plane and XZ-plane

In comparison with the as-built specimen, this indicated that IN939 did experience no grain recrystallization processes, whose morphology stayed the same. Fig. 19 displays the specimen's microstructure following etching.

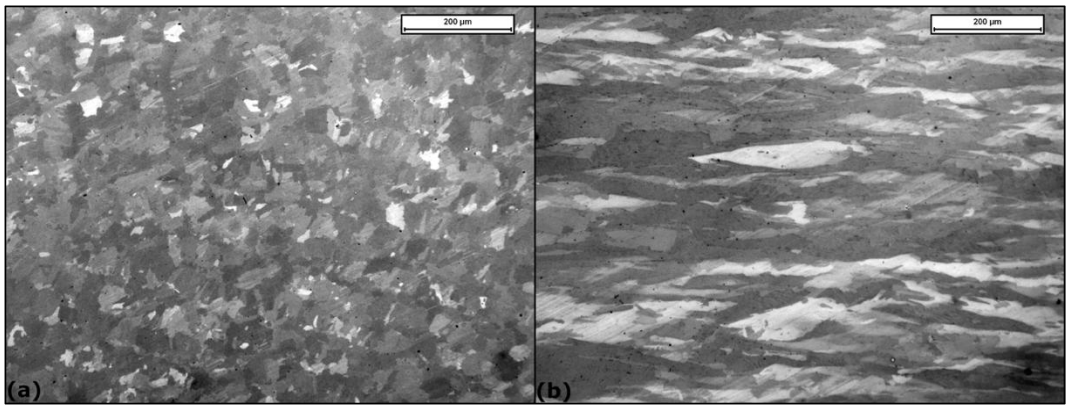

Fig. 19 Grain microstructure of solution heat-treated IN939 in the (a) XY-plane and (b) XZ-plane

It is evident that the microstructure of the two building planes differs significantly, particularly in the XZ plane where the columnar elongated grain, that was produced following the LPBF process, is still visible, whereas the equiaxial grain is visible in the XY plane. A possible explanation for this anisotropic microstructure could be related to the low processing temperature, which could be insufficient to trigger the recrystallization due to the higher stability of LPBF microstructure. Secondly, short soaking time i.e. 1 h, could be insufficient to provoke a full recrystallization.

3.2.2. Non-standard heat treatments and location of incipient melting range

As mentioned in section 2.5, the next four heat treatments, which were carried out in a static furnace, served to quantify the liquid phase formation in the temperature range identified from the DSC test. Fig. 20 shows an overview of images of the surfaces of the 4 specimens after the heat treatments along the XY plane.

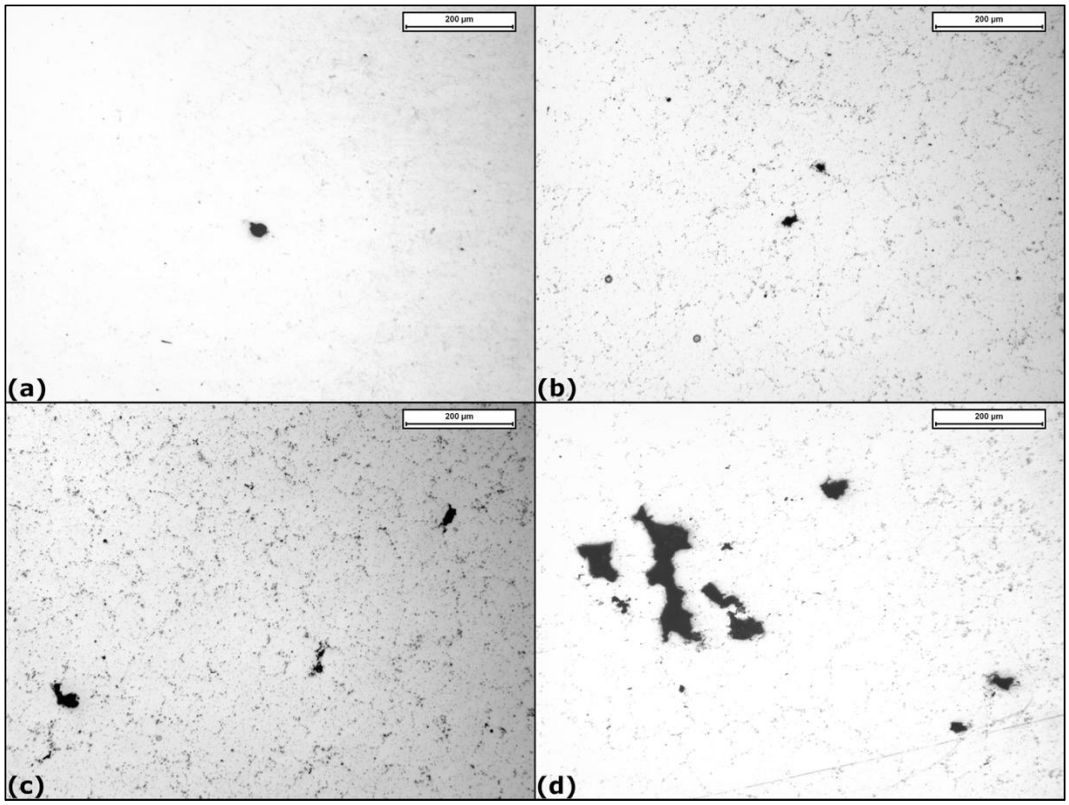

Fig. 20 Optical microscope image of non-standard heat-treated samples in XY-plane: (a) 1270 °C, (b) 1280 °C, (c) 1290 °C, (d) 1300 °C

For the specimens treated at 1270 °C, 1280 °C and 1290 °C respectively, there is not so much difference between the defects present. On the other hand, for the specimen treated at 1300 °C it is possible to observe porosity of considerable size due to incipient melting. Another aspect that can be seen is how, as the temperature increases, there is also an increase in carbides on the surface. The observations made earlier are valid for the XZ building plane, too; and the different surfaces can be observed in Fig. 21.

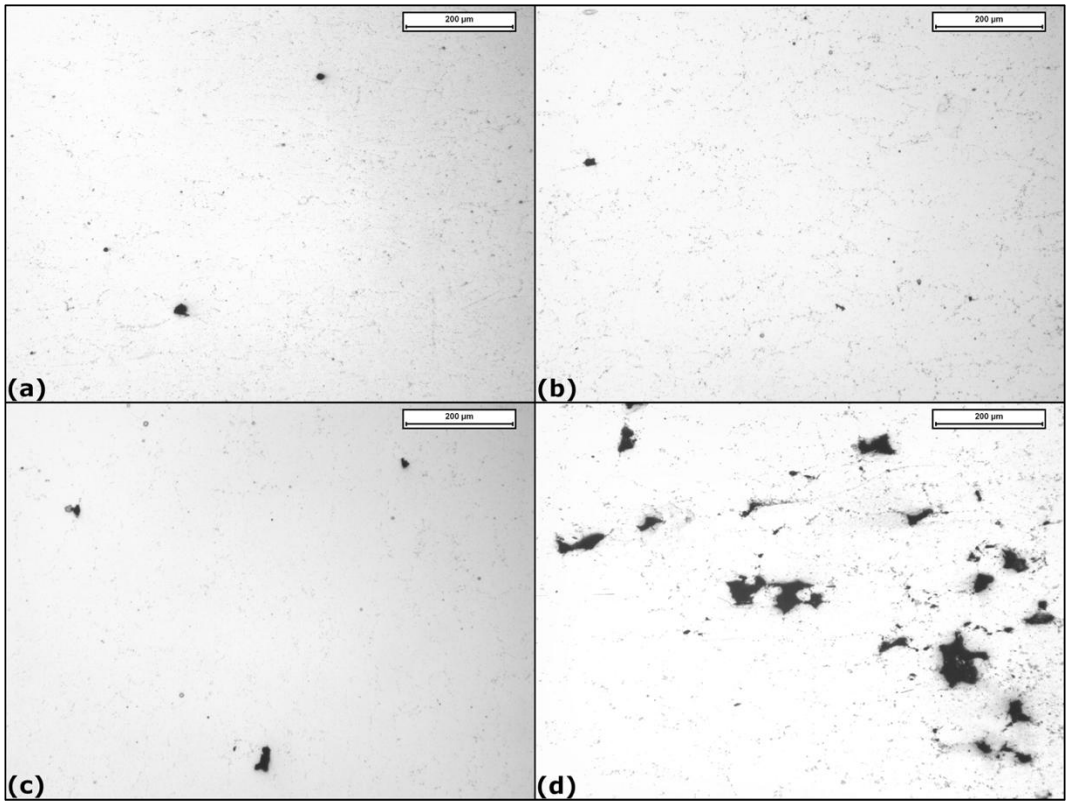

Fig. 21 Optical microscope image of non-standard heat-treated samples in XZ-plane: (a) 1270 °C, (b) 1280 °C, (c) 1290 °C, (d) 1300 °C

The following tables present the complete analysis conducted on the four samples. In particular, it can be observed that for the samples treated at 1270 °C and 1280 °C, the values of aspect ratio, average defect diameter, and residual porosity are very similar to each other in both the XY and XZ planes. However, at 1290 °C and 1300 °C, there is an increase in these values, especially concerning the residual porosity recorded at 1300 °C along the XZ plane. This is due to the presence of an abundant liquid phase at this temperature, which leads to uncontrolled porosity development during the cooling phase.

Table 6 Defect analysis summary of heat-treated temperature sample of 1270 °C

1270 °C	Av. Defects diameter [µm]	St. Dev.	Av. Vol. Porosities [%]	St. Dev.	Av. Aspect Ratio	St. Dev.
Surface XY	2.456	2.823	0.043	0.039	1.571	0.537
Core XY	2.643	9.912	0.043	0.029	1.575	0.759
Surface XZ	3.026	4.235	0.102	0.073	1.715	0.673
Core XZ	3.096	3.789	0.053	0.022	1.518	0.460

Table 7 Defect analysis summary of heat-treated temperature sample of 1280 °C

1280 °C	Av. Defects diameter [µm]	St. Dev.	Av. Vol. Porosities [%]	St. Dev.	Av. Aspect Ratio	St. Dev.
Surface XY	2.152	1.548	0.043	0.020	1.498	0.493
Core XY	1.548	1.455	0.062	0.032	1.517	0.595
Surface XZ	2.826	2.126	0.049	0.024	1.507	0.507
Core XZ	1.984	2.390	0.041	0.020	1.616	0.638

Table 8 Defect analysis summary of heat-treated temperature sample of 1290 °C

1290 °C	Av. Defects diameter [µm]	St. Dev.	Av. Vol. Porosities [%]	St. Dev.	Av. Aspect Ratio	St. Dev.
Surface XY	X	X	X	X	X	X
Core XY	3.184	4.775	0.268	0.053	1.751	0.768
Surface XZ	3.377	4.211	0.093	0.069	1.448	0.578
Core XZ	2.795	5.370	0.149	0.058	1.600	0.670

Table 9 Defect analysis summary of heat-treated temperature sample of 1300 °C

1300 °C	Av. Defects diameter [µm]	St. Dev.	Av. Vol. Porosities [%]	St. Dev.	Av. Aspect Ratio	St. Dev.
Surface XY	2.167	2.650	0.074	0.031	1.695	0.701
Core XY	5.136	10.299	0.627	0.863	1.901	0.930
Surface XZ	6.698	18.249	4.806	3.035	1.908	0.981
Core XZ	6.086	10.834	2.127	0.969	1.953	1.021

For a better data visualization, the residual porosity and aspect ratio are shown in Fig. 22 and Fig. 23 here below.

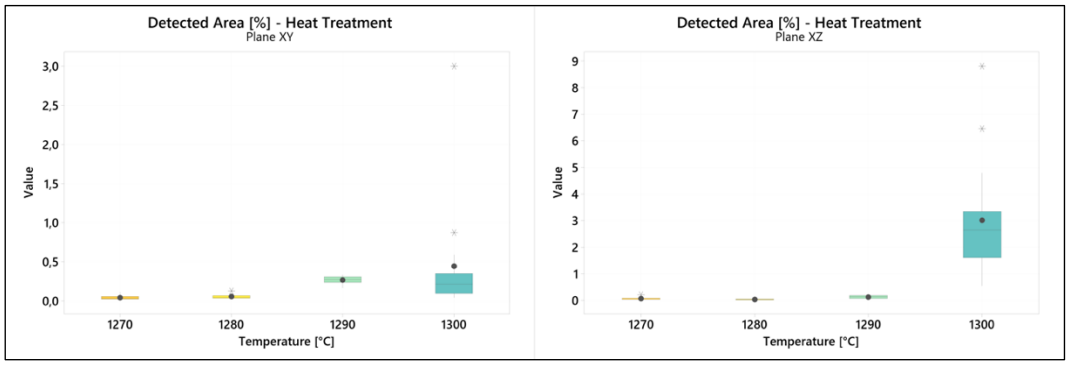

Fig. 22 Residual porosity boxplot of the non-standard heat-treated samples in the XY and XZ planes

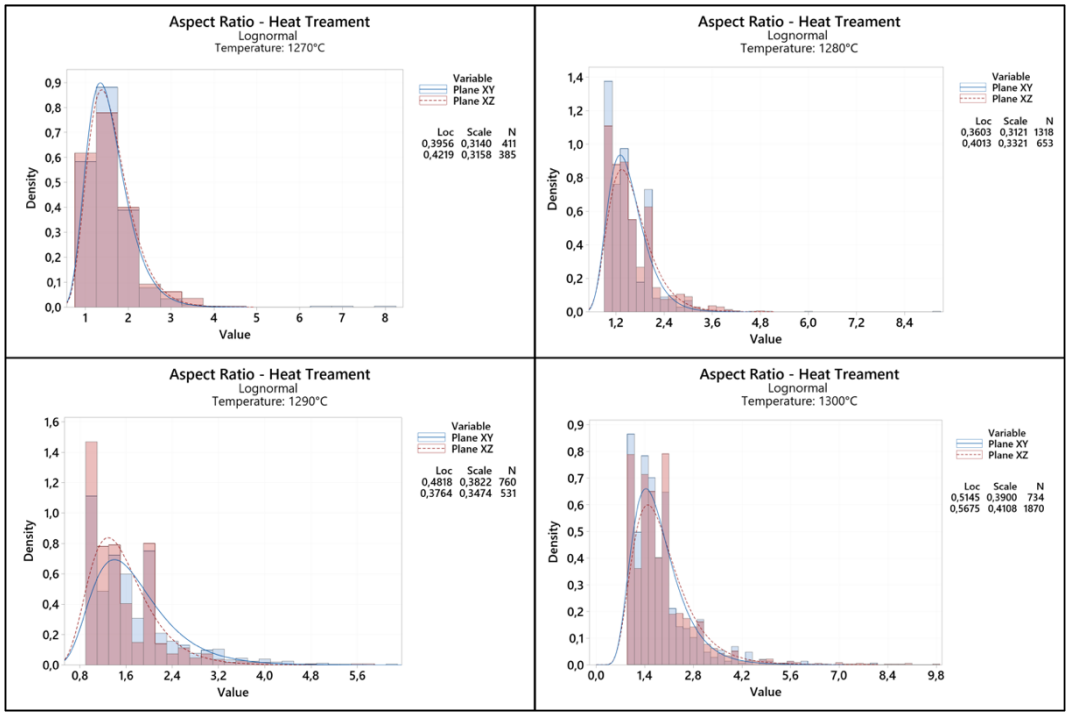

Fig. 23 Aspect ratio histogram of the non-standard heat-treated samples in the XY and XZ planes

Observing the histograms shown in Fig. 23, it is noticeable that for the samples treated at 1270 °C and 1280 °C, the highest density peaks are located in the 1.25 - 1.75 and 0.9 - 1.1 classes, respectively. This indicates that the porosity still maintains spherical shape. In the sample treated at 1290 °C, a second isolated peak is observed in the 1.9 - 2.1 class, distinct from the main one. This suggests the presence of a specific class of porosity with a different geometry, possibly linked to the formation of new pores due to the presence of a liquid phase formed at this temperature. As cooling ends, these pores may adopt a non-spherical geometry. In contrast, multiple peaks are present across different classes for the sample treated at 1300 °C, indicating the presence of porosities with geometries far from spherical form. In this case, the higher temperature has led to an even more extensive development of the liquid phase, which has allowed for the development of larger and more complex shaped porosities. To conclude, Fig. 24 shows the evolution of the grain microstructure in the XY and XZ building planes at different treatment temperatures. Comparing the grain microstructure at various temperatures, we can observe that at 1270 °C (Fig. 24 a, e) and at

1280 °C (Fig. 24 b, f), along the XZ plane, the grains continue to maintain their elongated shape, as given by the building process.

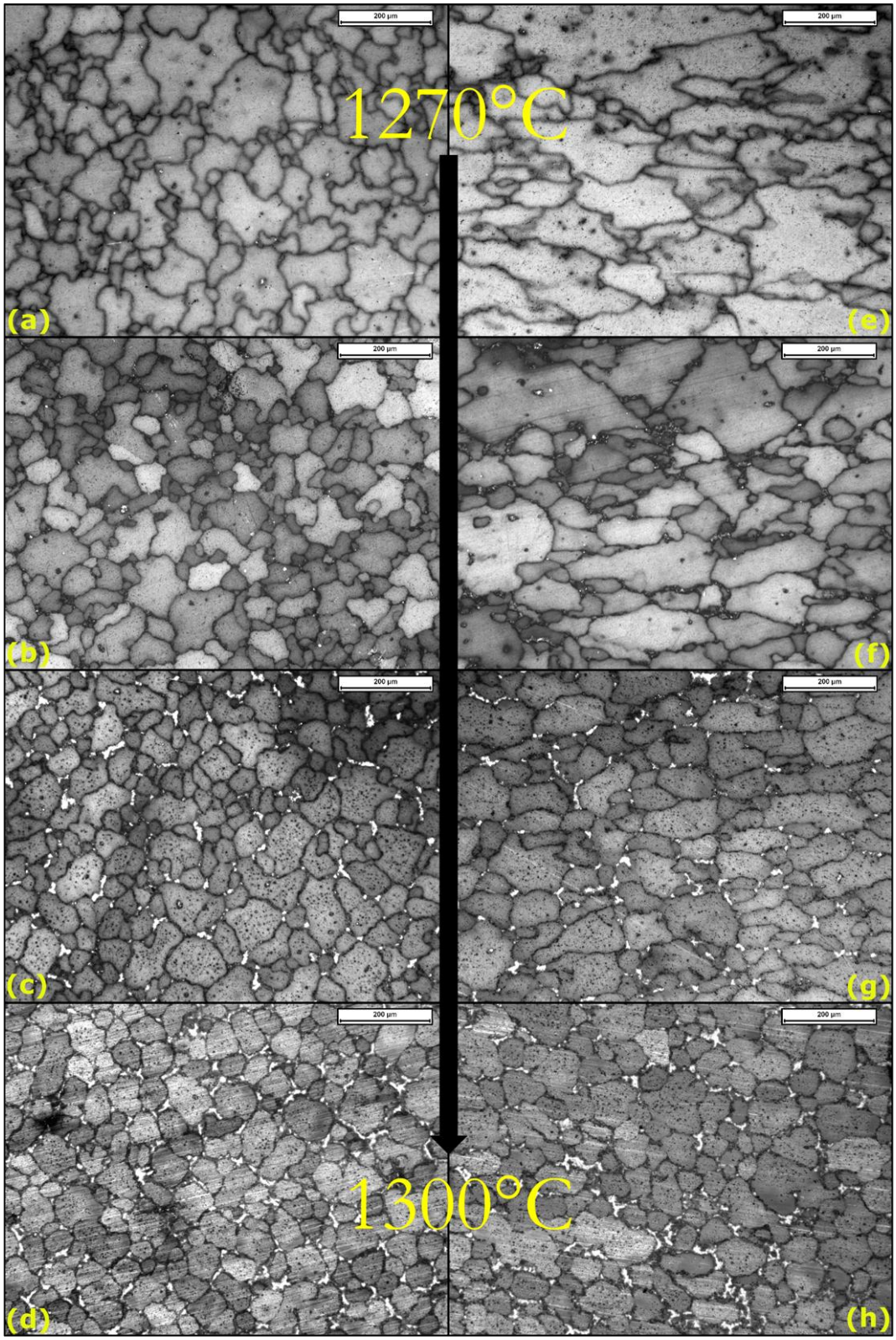

Fig. 24 Evolution of grain microstructure of non-standard heat-treated samples IN939 in the XY (left) and XZ (right) planes at temperature of: (a, e) 1270 °C, (b, f) 1280 °C, (c, g) 1290 °C and (d, h) 1300 °C

Furthermore, a bimodal grain distribution is evident, with larger grains surrounded by smaller ones. At 1290 °C (Fig. 24 c, g), however, two different phenomena can be observed: first, the grains begin to lose their elongated shape and become more equiaxed. Secondly, there are lighter areas at the grain boundaries, which may indicate the formation of precipitated carbides along the grain boundaries. Finally, in the sample treated at 1300 °C (Fig. 24 d, h), we see that the grains have reached a similar geometry in both the XY and XZ planes, with an increased presence of carbides along the grain boundaries. This phenomenon may be due to the fact that up to 1270 °C, IN939 undergoes only a grain growth process, driven by the temperature increase. When this temperature is exceeded, the alloy undergoes a process of solubilization and subsequent grain recrystallization, causing it to progressively lose its elongated shape along the XZ plane up to 1300 °C, where an equiaxed grain structure is observed in both the XY and XZ planes. This is confirmed by Fig. 25, which shows the average grain diameter at different temperatures.

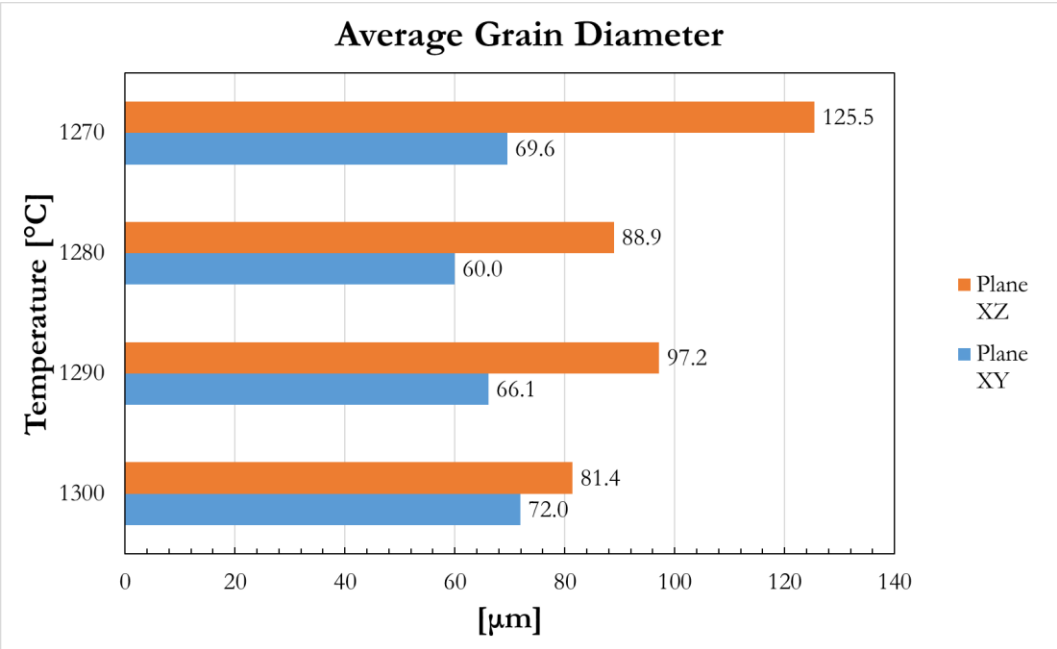

Fig. 25 Comparison of non-standard heat-treated average grain diameters samples

3.3. Microstructural assessment of HIPped samples

The main purpose of this thesis is to assess whether the hot isostatic pressing process above the solidus temperature of IN939 is feasible. Two conditions must be met: achieving a defect-less or nearly defect-less material by eliminating residual porosity and, at the same time, improving the grain microstructure compared to the as-built state resulting from the AM process. Three main variables were considered that can influence the material's microstructure and can be set during HIP: temperature, pressure, and time. To determine the optimal values to be used in HIP, the Design of Experiment (DOE) approach was applied by using the Taguchi method. This approach provided consistent results while minimizing the number of tests performed. The values included in the DOE take into account all previous test results. In particular, the heat treatments revealed that the temperature of 1300 °C resulted in the formation of an extensive liquid-phase region throughout the sample. To avoid HIP failures, this temperature was discarded; instead, temperatures of 1270 °C, 1280 °C, and 1290 °C were considered. Literature indicates that the pressure typically applied to Ni-based superalloys is above 100 MPa, so the selected values were 150 MPa, 125 MPa, and 100 MPa. For the last parameter, i.e. process time, three main values were considered: 80, 160, and 240 minutes. These values considered observations from the solution heat treatment, where a certain degree of grain recrystallization was observed. Once the 9 values for the study were defined, the software provided the 9 tests to be conducted to HIP. Table 10 presents a summary of the variables used for each test.

Table 10 Summary of DOE results

Sample	Temperature [°C]	Pressure [MPa]	Time [min]
1	1290	150	240
2	1290	125	160
3	1290	100	80
4	1280	150	160
5	1280	125	80
6	1280	100	240
7	1270	150	80
8	1270	125	240
9	1270	100	160

Fig. 26 shows the thermogram with temperature and pressure trends over time, for a test conducted with HIP.

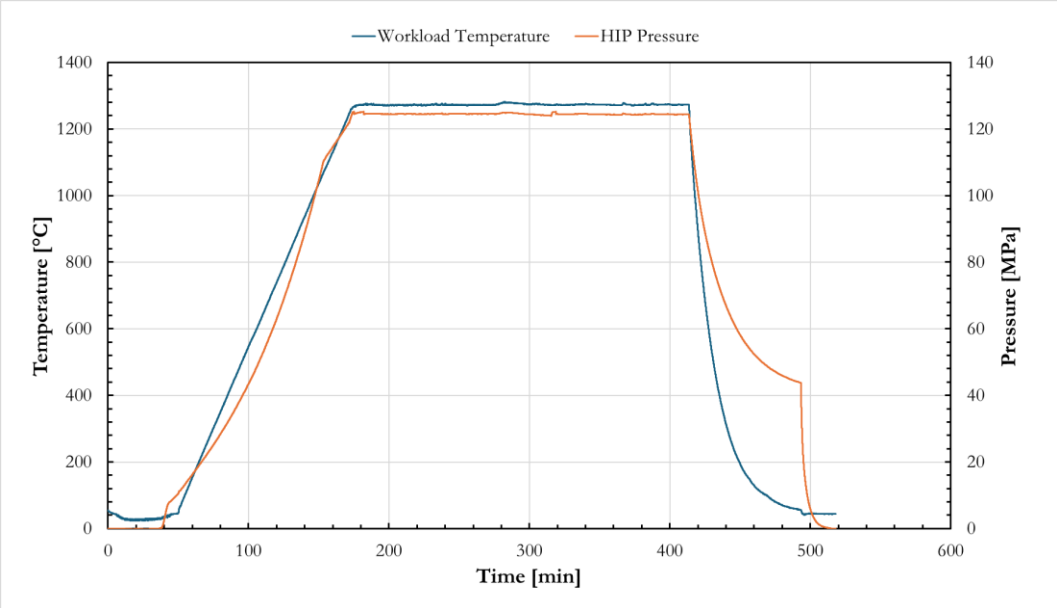

Fig. 26 Temperature and pressure curves in a HIP cycle

For all the analyses that will be presented, i.e. microstructure, grain size, and related SEM images, only the XY building plane has been considered.

3.3.1. Sample 1: 1290 °C – 150 MPa – 240 min

Fig. 27 shows the remaining defectiveness in the sample 1, near the surface and in the core, respectively. Table 11, on the other hand, provides a summary of the data from the internal porosity analysis.

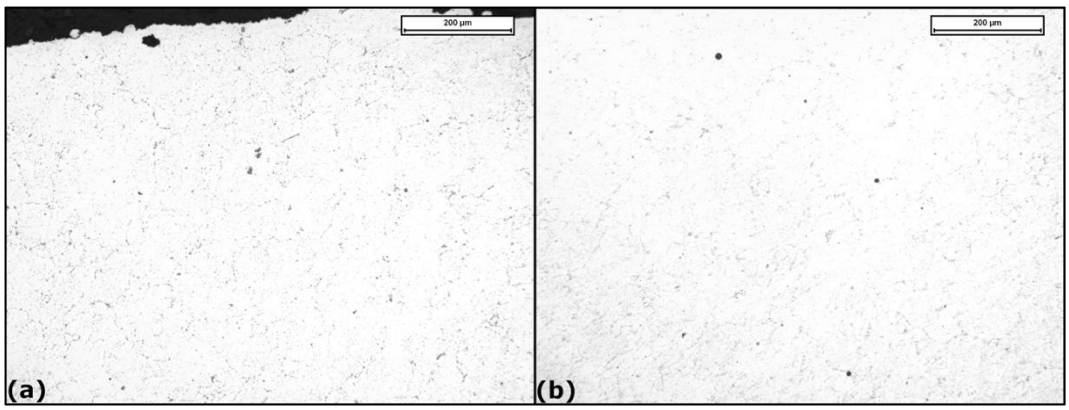

Fig. 27 Density analysis of sample 1 along (a) surface and (b) core

Table 11 Defect analysis summary of Sample 1

Sample 1	Av. Defects diameter [µm]	St. Dev.	Av. Vol. Porosities [%]	St. Dev.	Av. Aspect Ratio	St. Dev.
Surface	3.391	6.433	0.101	0.074	1.641	0.699
Core	3.357	3.865	0.063	0.032	1.466	0.555

Based on the obtained data, it is observed that both the residual porosity and the aspect ratio values are similar to or slightly lower than those of the as-built samples. Fig. 27(a) shows the presence of extremely fine carbides across the entire surface. From the histogram shown in Fig. 28, which displays the trend of the aspect ratio, we can conclude that the most relevant class falls between 0.9 and 1.1, suggesting that the porosities present predominantly exhibit a circular morphology.

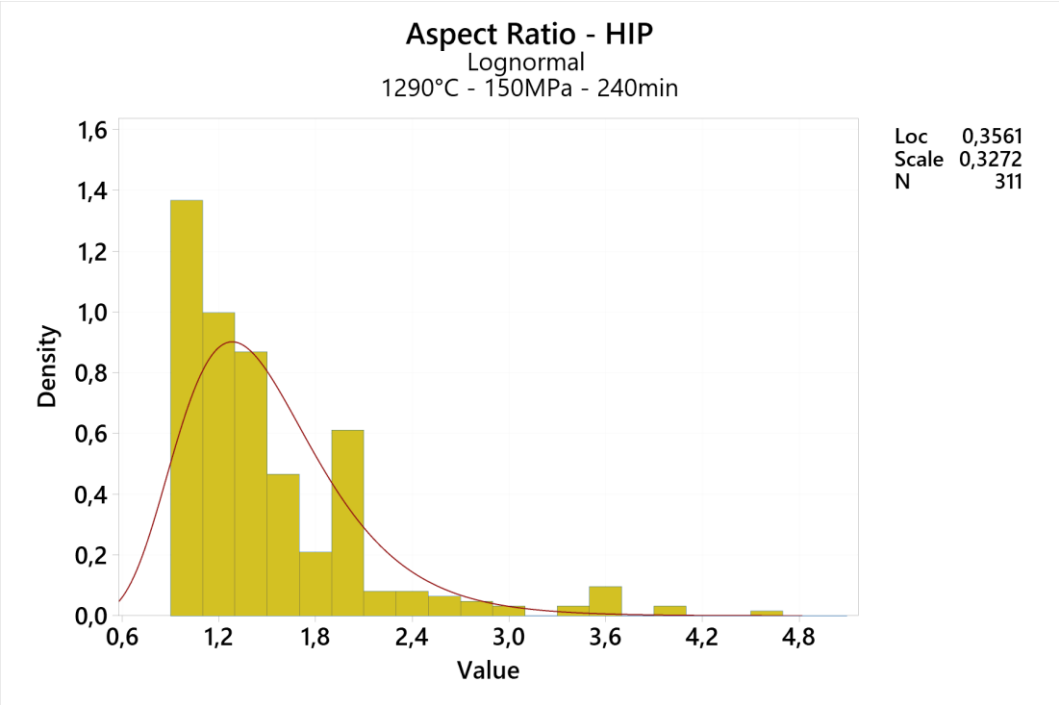

Fig. 28 Aspect ratio histogram of the Sample 1: 1290 °C – 150 MPa – 240 min

Fig. 29 shows the grain microstructure.

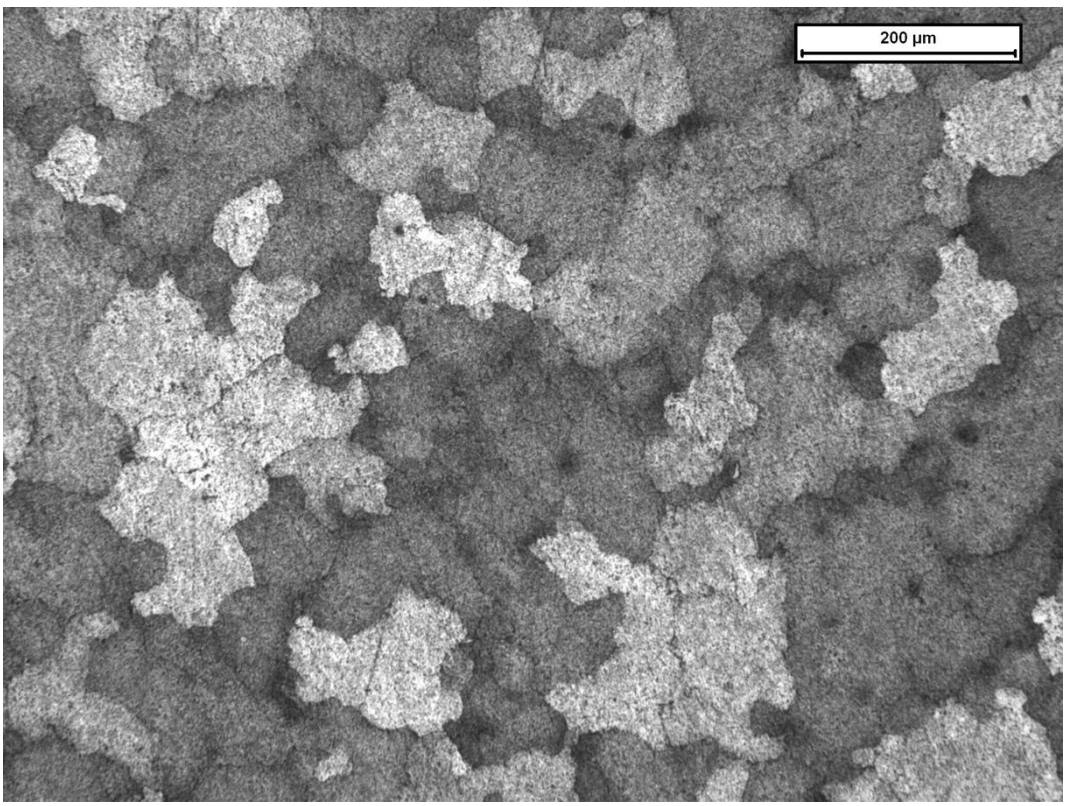

Fig. 29 Grain microstructure of Sample 1 with optical microscope at 100x magnification

Calculations indicate that the average grain size for this sample is approximately 105 μm. In conclusion, the SEM analysis shown in Fig. 30 highlights the presence of Ti, Ta, and Nb carbides across the entire inspect surface, both at the grain boundaries and intragranular.

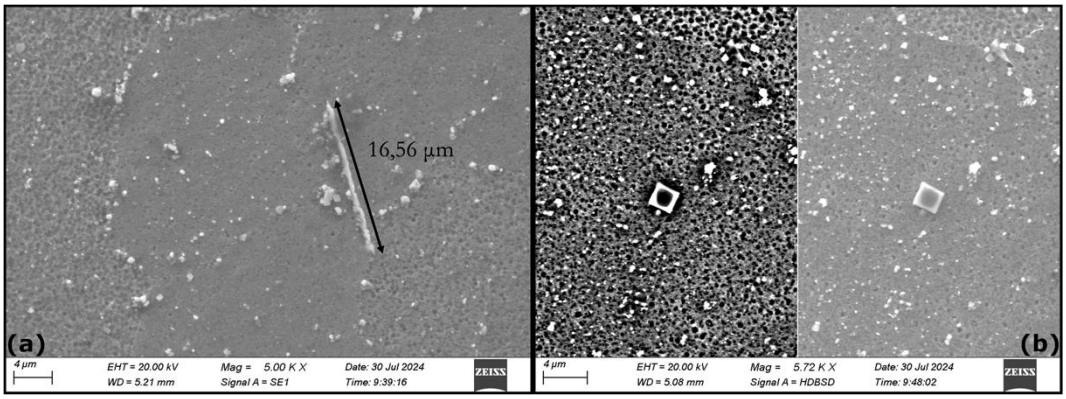

Fig. 30 (a) SE1 signal and (b) BSD signal of different types of carbides presents in the Sample 1

In particular, the grain boundary carbides can be associated with $M_{23}C_6$, while for intragranular carbides, the presence of spherical morphology M_6C carbide is observed. Notably, in Fig. 30(a), the $M_{23}C_6$ carbide exhibits an elongated shape, indicating a high aspect ratio with a length of approximately 16μm. In Fig. 30(b), there is evidence of a possible titanium carbonitride, confirmed by the backscattered electron image, which shows a darker central area (indicating a lighter element) and a brighter outer area (indicating a heavier element). Additional evidence is provided by the EDS analysis, which confirmed the findings mentioned above. Fig. 31(a), on the other hand, shows the presence of another $M_{23}C_6$ carbides at the grain boundaries. What is more interesting can be observed in Fig. 31(b), where residual porosity can be seen with a possible M_6C carbide inside.

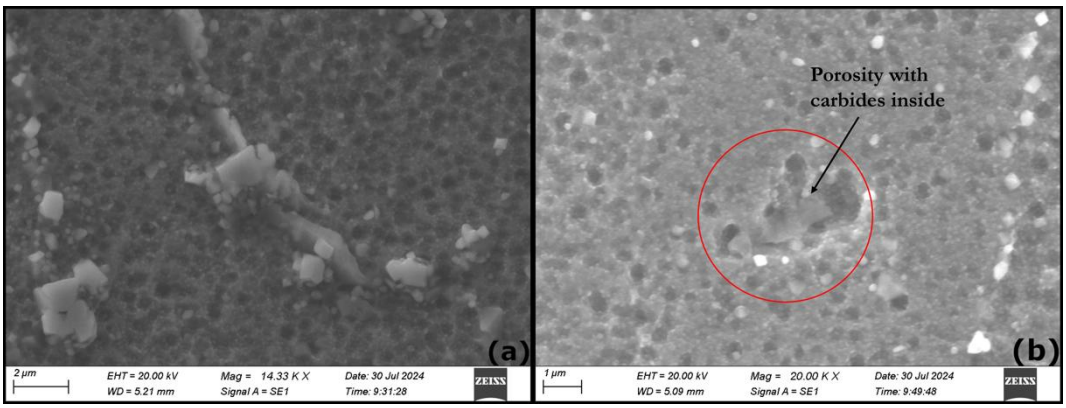

Fig. 31 (a) SE1 Signal of $M_{23}C_6$ carbides and (b) SE1 signal of residual porosity with carbides inside in the sample 1

It is likely that during the HIP phase, the pore could not be completely closed precisely, due to the presence of the carbide, which hindered its closure. To conclude the investigation of sample 1, SEM analysis revealed the presence of γ', with a homogeneous and monomodal distribution on the surface, exhibiting a spherical morphology.

3.3.2. Sample 2: 1290 °C – 125 MPa – 160 min

Fig. 32 shows images of the remaining defects in specimen 2, both near edge sample surface and core. Meanwhile, Table 12 provides a summary of the data related to the overall defectiveness of Sample 2.

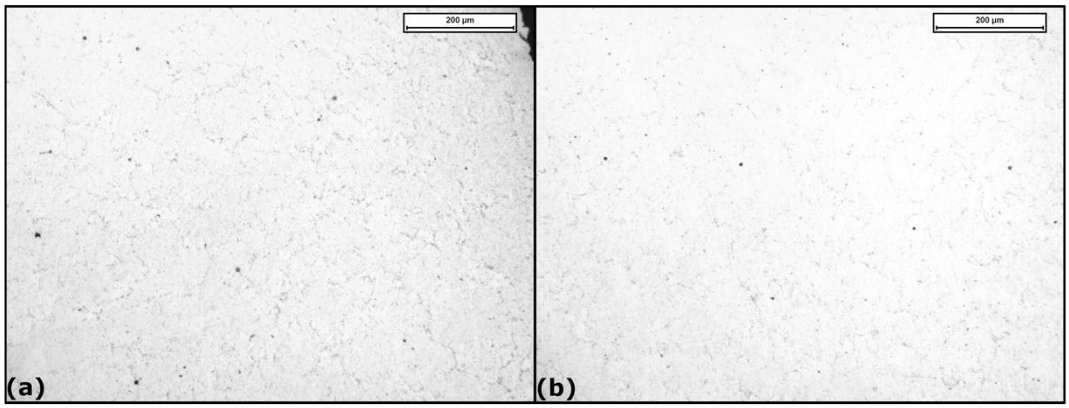

Fig. 32 Density analysis of sample 2 along (a) surface and (b) core

Table 12 Defect analysis summary of Sample 2

Sample 2	Av. Defects diameter [µm]	St. Dev.	Av. Vol. Porosities [%]	St. Dev.	Av. Aspect Ratio	St. Dev.
Surface	2.102	1.721	0.036	0.011	1.706	0.716
Core	2.121	2.353	0.032	0.039	1.617	0.619

From the above summary, it can be observed that defects show 1µm smaller diameter with respect to sample 1, this means that, considering the standard deviation as well, the values obtained between these two samples are similar. Furthermore, the average volume porosity is also significantly lower. This indicates that this sample is denser than the previous one. However, it should also be noted that the average value of the aspect ratio is higher than in sample 1.

From the histogram shown in Fig. 33, it can be seen that the peak with the highest density of recorded values corresponds to the 0.9 - 1.1 range. Similarly, there are two other peaks for higher value ranges, indicating the presence of porosity with a shape ratio that diverges from the unitary value.

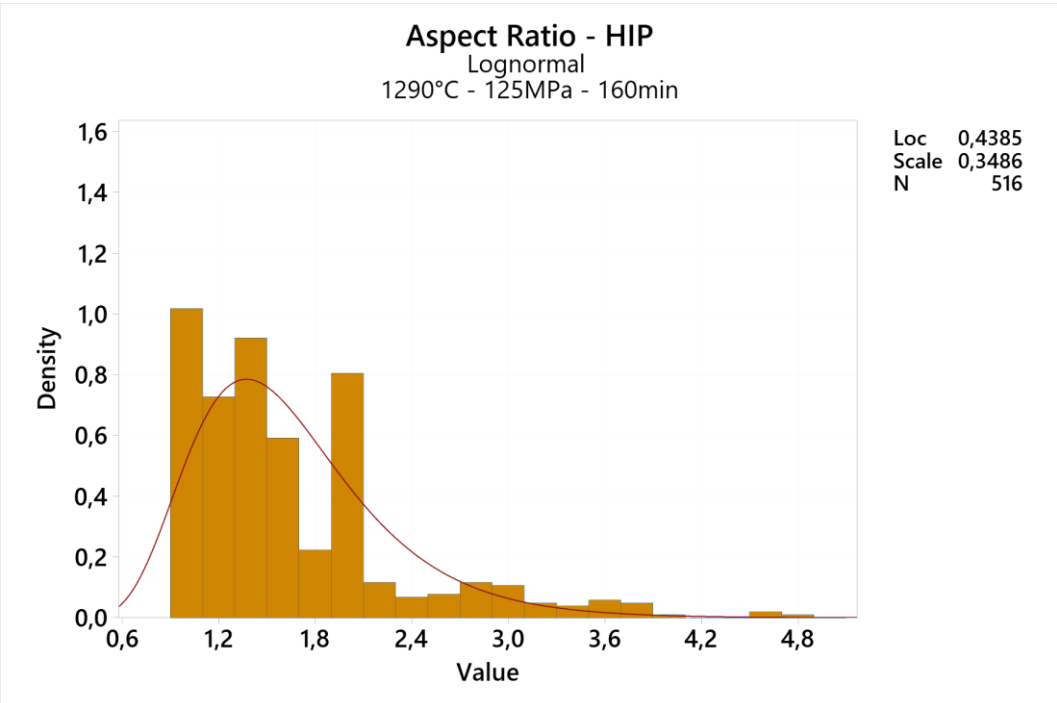

Fig. 33 Aspect ratio histogram of the Sample 2: 1290 °C – 125 MPa – 160 min

Fig. 34 shows the microstructure of the grains, and it can be seen that this is quite similar to that observed in sample 1. A slightly lower average grain value of 73 μm was recorded. The fact that the average grain size is smaller is probably related to the shorter process time, i.e. less time for grain growth during the recrystallisation phase.

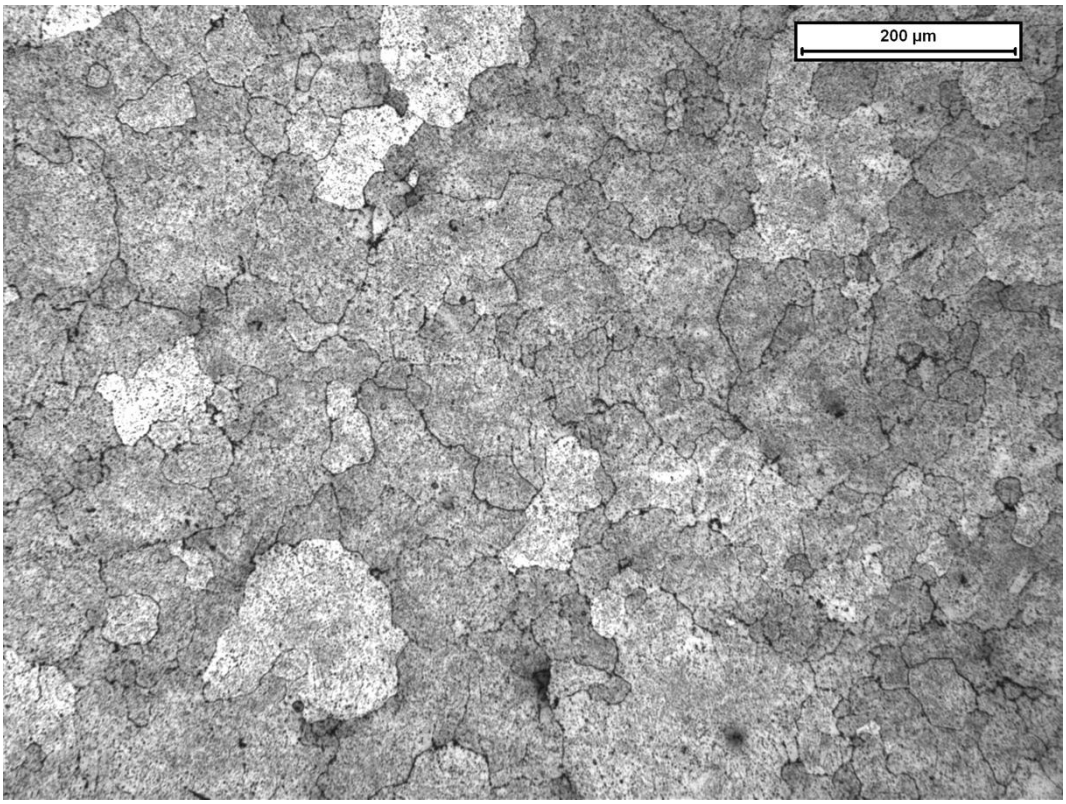

Fig. 34 Grain microstructure of Sample 2 with optical microscope at 100x magnification

The SEM analysis showed that this sample has a microstructure different from that one previously observed in sample 1. Specifically, it is possible to observe, in both images shown in Fig. 35, a greater presence of carbides homogeneously distributed across the entire surface.

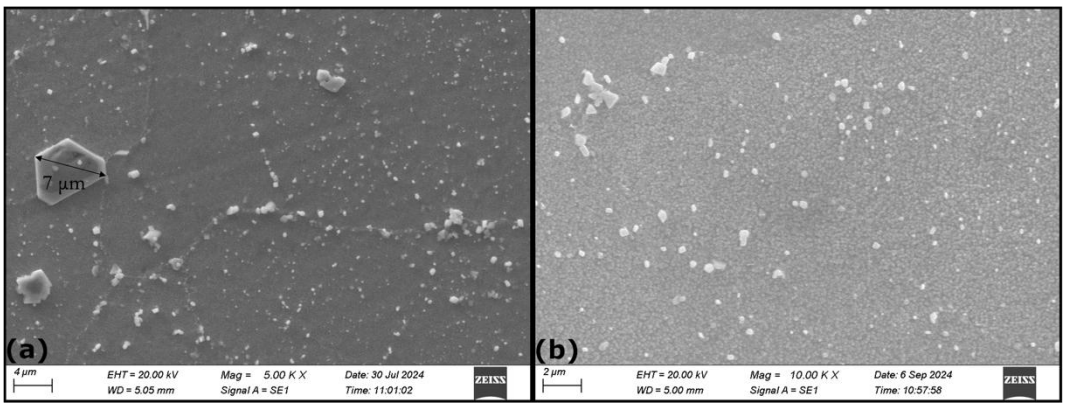

Fig. 35 SE1 signals at different magnifications of sample 2 where it is possible to observe different types of carbides, such as $M_{23}C_6$ (a) and M_6C (b)

The grain boundaries contain a higher quantity of $M_{23}C_6$ carbides compared to sample 1, and within the grains, a greater quantity of spherical and small MC carbides can also be seen. The increased quantity of carbides compared to sample 1 can be related to the precipitation temperature of 1293 °C, obtained from the DSC test. However, it is particularly likely that the shorter processing time, compared to sample 1, favoured the nucleation of a greater amount of smaller carbides, predominantly intragranular and of the M_6C type. Finally, in Fig. 36(a), which shows the microstructure at a higher magnification respect to the previous figure, the presence of homogeneously distributed γ' with an extremely fine structure can be observed. In the last image, in Fig. 36(b), an additional area is shown where $M_{23}C_6$ carbides of various sizes are present along the grain boundary.

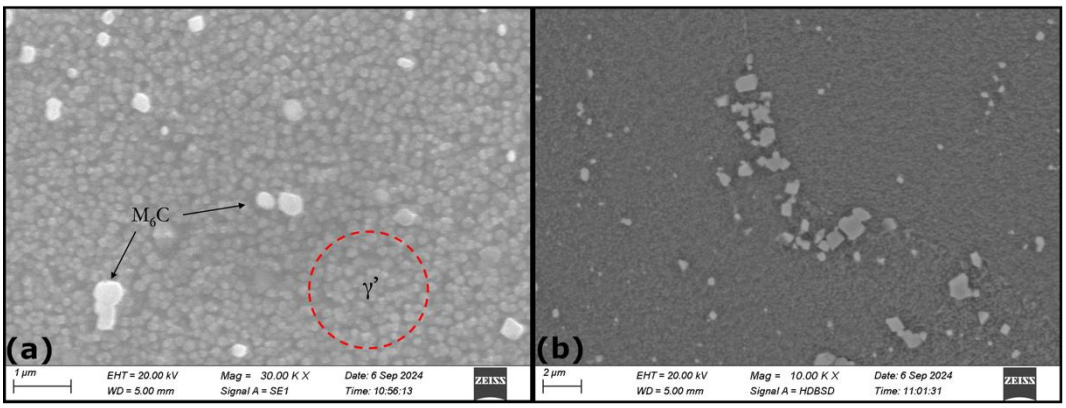

Fig. 36 (a) SE1 signal of M_6C carbides and γ' phase and (b) BSD signal of $M_{23}C_6$ carbides along the grain boundary

3.3.3. Sample 3: 1290 °C – 100 MPa – 80 min

Fig. 37 shows illustrative images of sample 3 surfaces near the edge, Fig. 37(a), and core, Fig. 37(b). Table 13 shows the density analysis of the specimen.

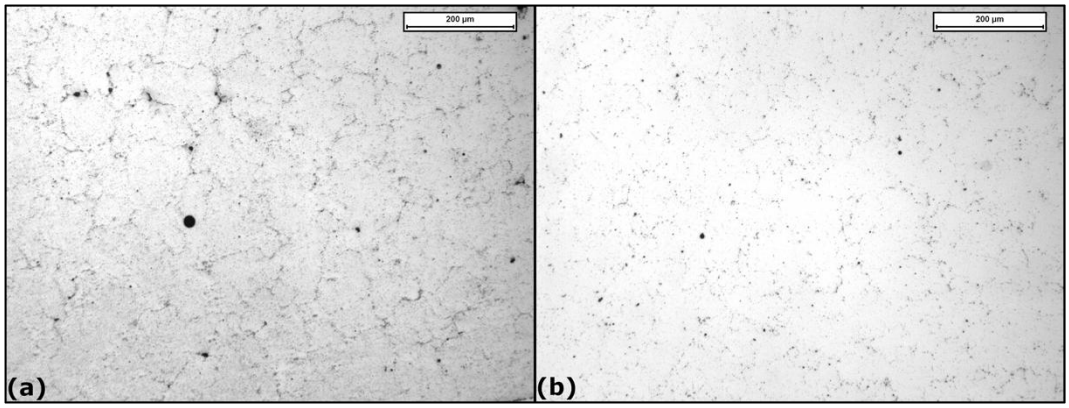

Fig. 37 Density analysis of sample 3 along (a) surface and (b) core

Table 13 Defect analysis summary of Sample 3

Sample 3	Av. Defects diameter [µm]	St. Dev.	Av. Vol. Porosities [%]	St. Dev.	Av. Aspect Ratio	St. Dev.
Surface	2.381	2.615	0.103	0.057	1.660	0.626
Core	1.532	1.371	0.029	0.013	1.465	0.507

From the analysis of the density of the following sample, it can be observed that the average diameter of the defects shows a lower value compared to previous samples, and the same applies to the shape ratio. In particular, a similarity with sample 1 can be noted for all three studied parameters. Regarding the residual porosity, a value similar to that recorded in sample 1 is observed at the edge, while the lowest value among the samples hipped at 1290 °C is recorded at the core. Noteworthy, carbides are more numerous and observable with the optical microscope along the entire surface compared to previous samples. Finally, from the histogram shown in Fig. 38, it can be seen that the peak consistently corresponds to the 0.9 - 1.1 range. Additionally, in this case, a second peak can be observed in a higher value class, indicating the presence of defects with a higher shape ratio and, therefore, a more elongated structure.

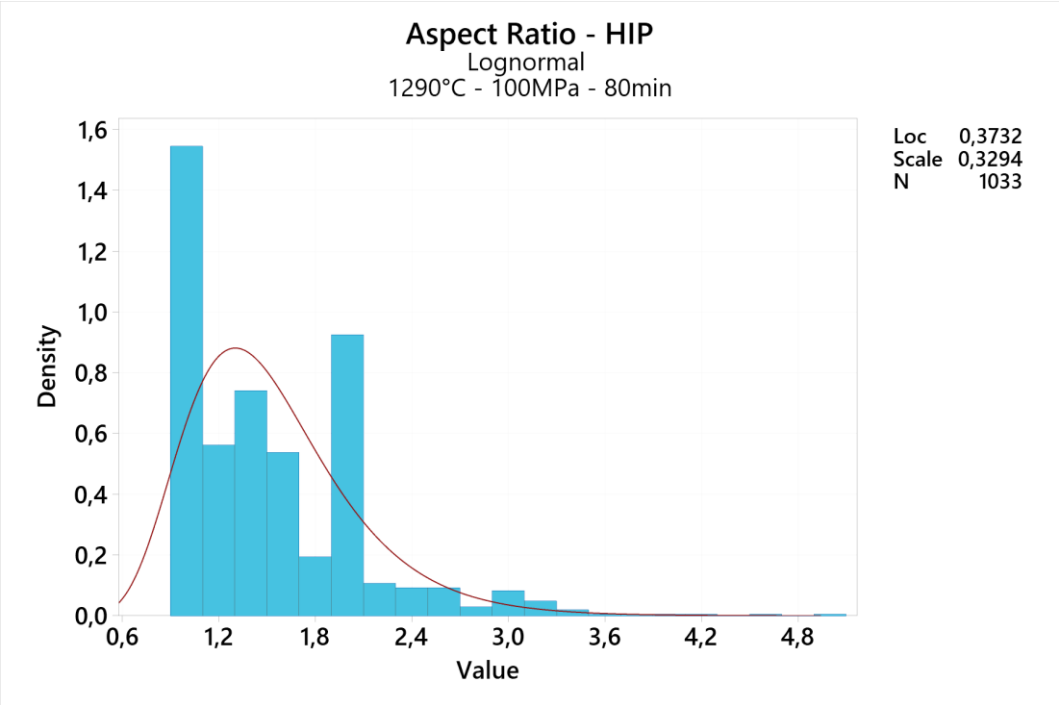

Fig. 38 Aspect ratio histogram of the Sample 3: 1290 °C – 100 MPa – 80 min

Fig. 39 shows the microstructure of the sample 3, highlighting the grain structure and size.

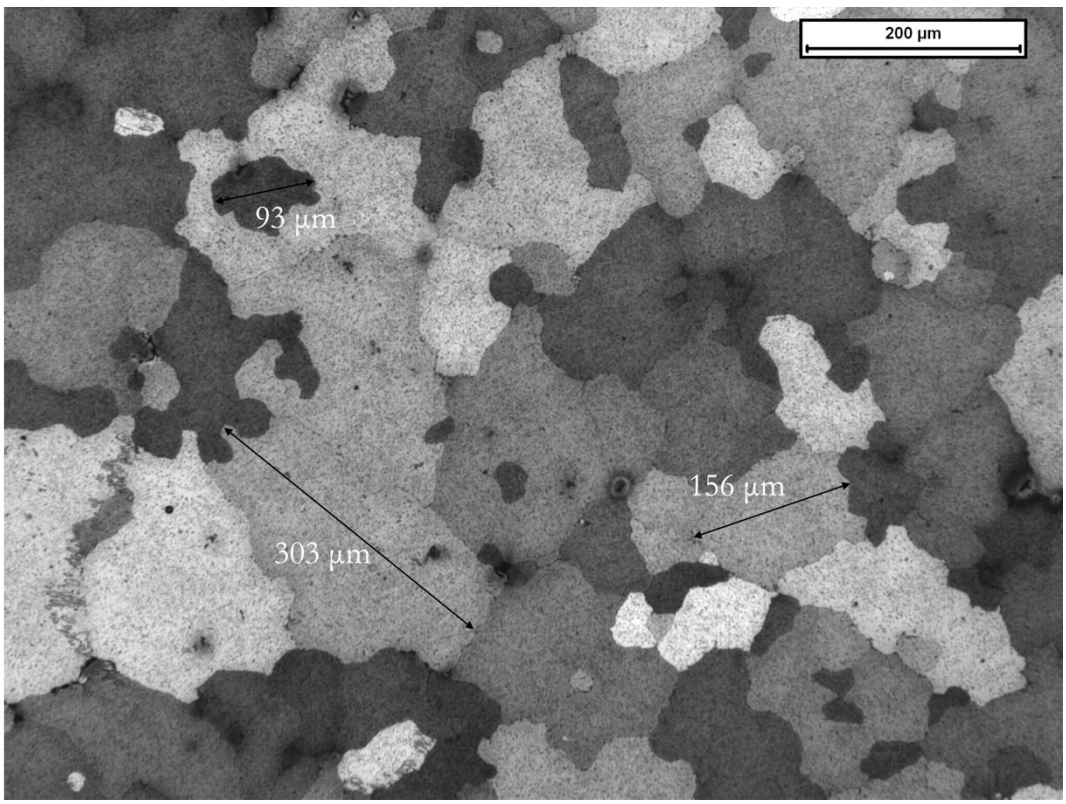

Fig. 39 Grain microstructure of Sample 3 with optical microscope at 100x magnification

It can be observed that the average grain size for this sample is 88 µm. Interestingly, there is a bimodal distribution of grain size in this case, with larger grains surrounded by smaller ones. From SEM observation of the following sample, it is evident that the γ' phase no longer exhibits a uniform size compared to previous observations. In Fig. 40(a), a bimodal size distribution is visible, with a higher presence of smaller γ' particles and a lower presence of larger γ' particles.

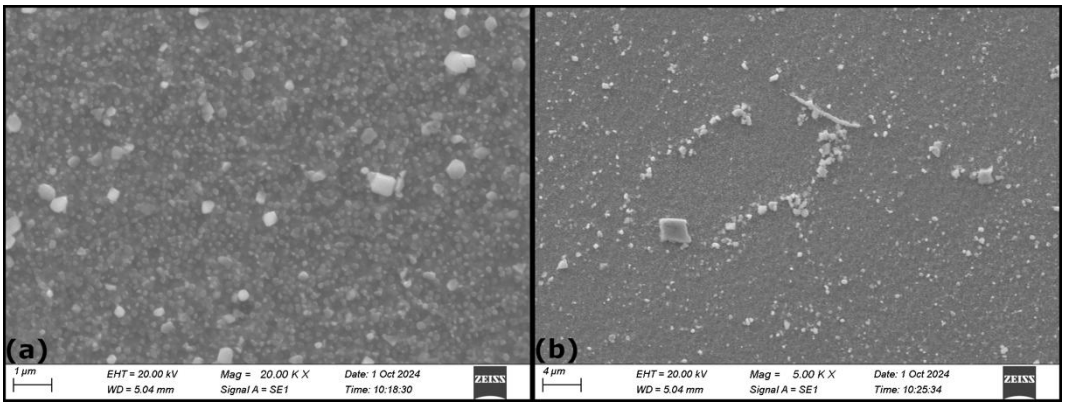

Fig. 40 (a) SE1 signal showing bimodal dimension distribution of γ' phase, (b) SE1 signal of $M_{23}C_6$ and M_6C carbides present in the microstructure

Additionally, as shown in Fig. 40(b), this sample also displays a high concentration of elongated $M_{23}C_6$ carbides at the grain boundaries and M_6C carbides within the grains. Furthermore, the analysis revealed additional types of precipitated phases. In particular, Fig. 41(a) shows the presence of an $M_{23}C_6$ carbide approximately 12 µm in length.

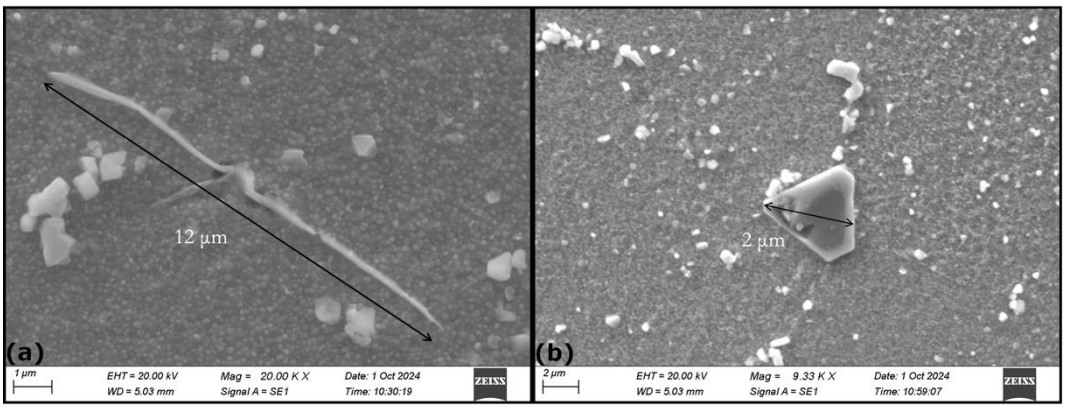

Fig. 41 (a) SE1 signal of $M_{23}C_6$ with high aspect ratio, (b) SE1 signal of carbonitride in the sample 3

This is confirmed by EDS analysis, shown in Fig. 42(b), which detected Cr, Co, C, and a smaller percentage of Ti, indicating Ti segregation in the carbide, located at the grain

boundary rather than within the γ' phase, i.e. a phenomenon that will have a greater impact on samples treated at 1280 °C. Lastly, Fig. 41(b) displays a mixed precipitate, consisting of Ti nitride internally and externally of a mixed Ti-Ta carbide, with a smaller amount of Nb. In this case as well, the semi-quantitative composition was provided by EDS analysis, and it is shown in Fig. 42.

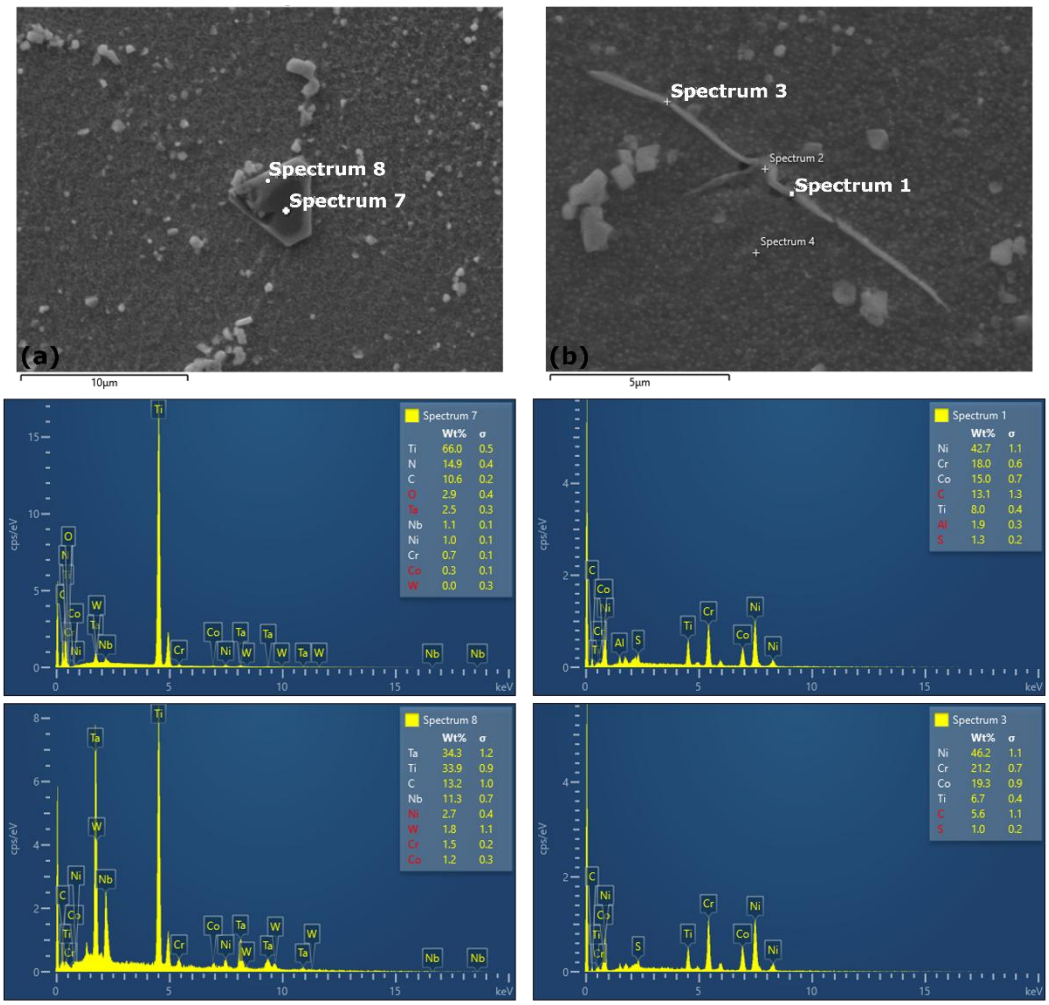

Fig. 42 EDS analysis highlighting (a) the presence of a titanium carbonitride and (b) the presence of an $M_{23}C_6$ carbide

Here is a comparison of the three HIP treatments performed at the same temperature. Specifically, Fig. 43 and Fig. 44 show, respectively, the histogram comparing the aspect ratio of the three samples and the boxplot of residual porosity. The histogram reveals that the density peaks all correspond to the same range of values, indicating that the porosities in all three samples exhibit a similar morphology.

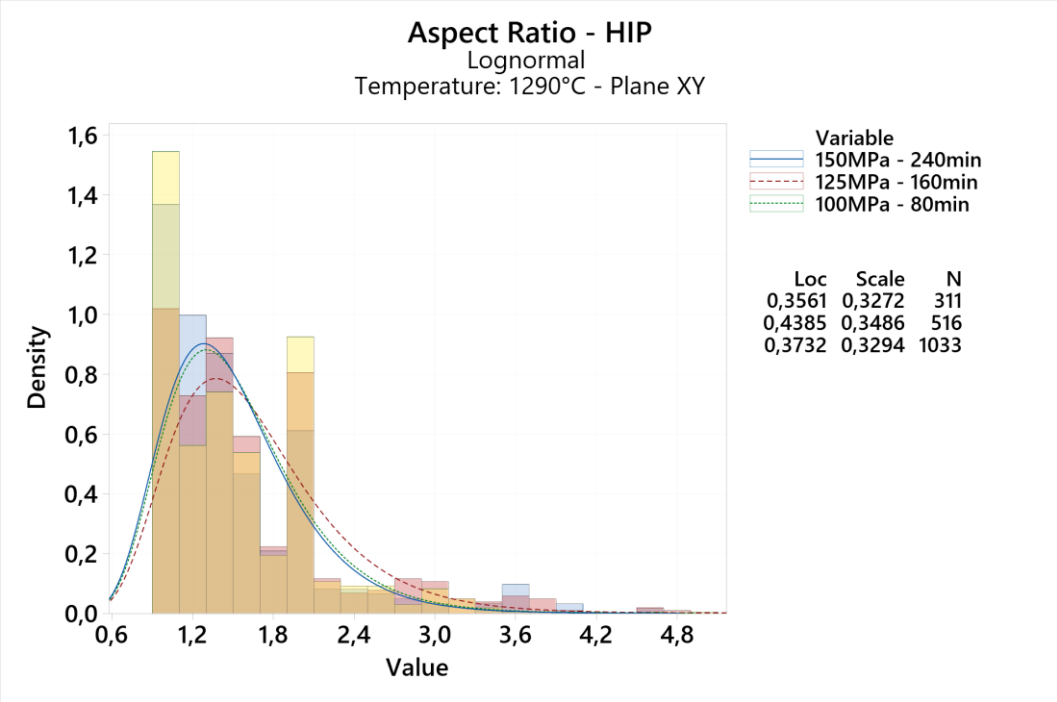

Fig. 43 Summary aspect ratio histogram of the sample 1, 2 and 3 with the same process temperature, i.e. 1290 °C

On the other hand, the boxplot shows that, compared to the initial "as-built" sample, the residual porosity values are significantly lower, indicating the effectiveness of HIP in repairing the material and eliminating defects from the LPBF process.

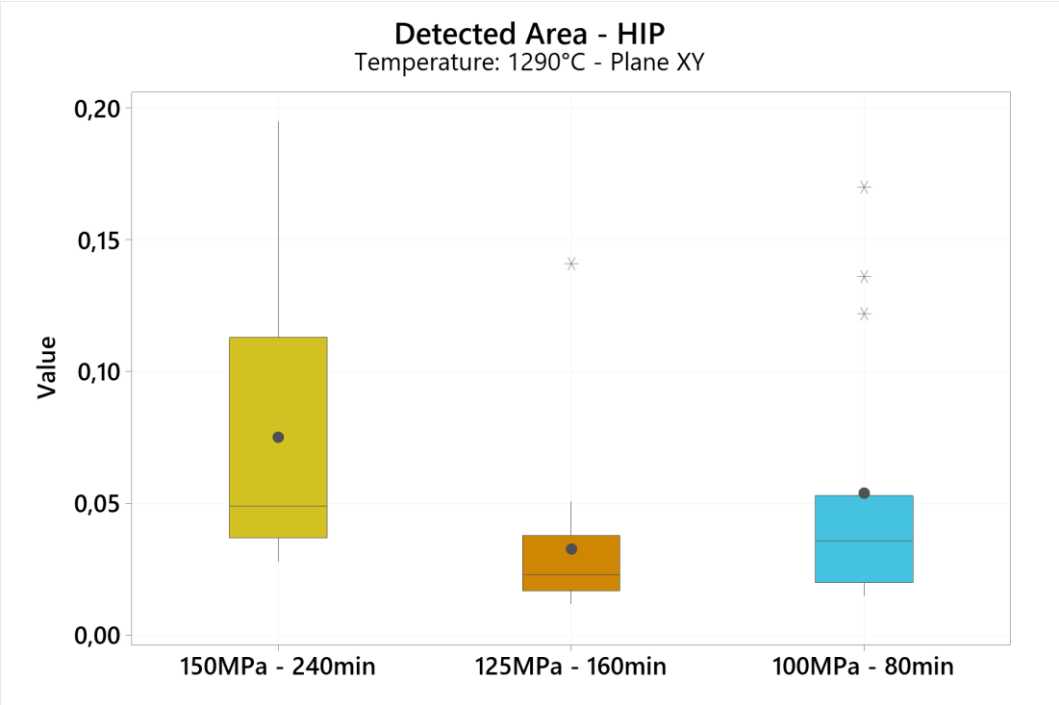

Fig. 44 Summary boxplot of residual porosity of the sample 1, 2 and 3 with the same process temperature, i.e. 1290 °C

Finally, Fig. 45 shows the comparison of the average grain sizes of the three samples. From the graph, it can be seen that Sample 1, treated for 240 minutes, achieves the largest average grain diameter. However, it can also be observed that as the processing time increases from 80 to 160 minutes, the average grain size decreases.

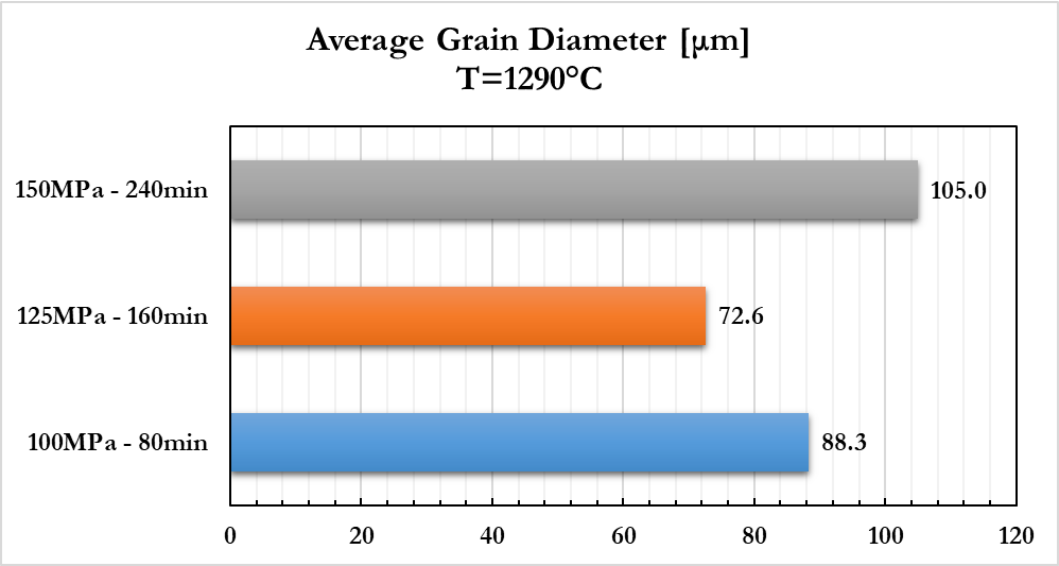

Fig. 45 Summary average grain diameter histogram of the sample 1, 2 and 3 with the same process temperature, i.e. 1290 °C

It is difficult to understand the reason behind this behaviour. A possible cause could be related to the complete absence of grain boundary regulators such as $M_{23}C_6$- and MC-type carbides, as well as the γ' phase, in sample 1, which corresponds to the 240 minutes processing time. This means that the grains can grow freely and significantly increase in size compared to the other two samples. Moreover, as observed in the SEM images in Fig. 46, samples 2 and 3 show a higher concentration of carbides on their surfaces, indicating a greater pinning effect exerted by the carbides on grain growth. In contrast, this concentration is lower in sample 1, confirming the observations mentioned earlier.

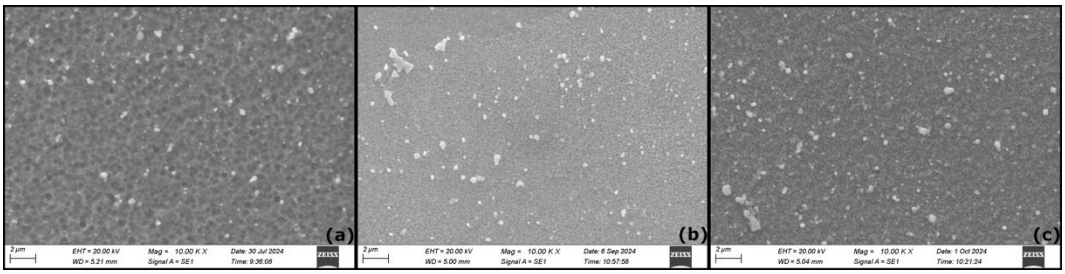

Fig. 46 SE1 signal comparison between samples treated at 1290 °C with different concentration of carbides on the surface: (a) sample 1 with 240 minutes of time process, (b) sample 2 with 160 minutes of time process and (c) sample 3 with 80 minutes of time process

3.3.4. Sample 4: 1280 °C – 150 MPa – 160 min

The optical microscope observation is shown in Fig. 47, where the surface at the sample edge and at the core is displayed. Table 14 shows the summary of the specimen density analysis.

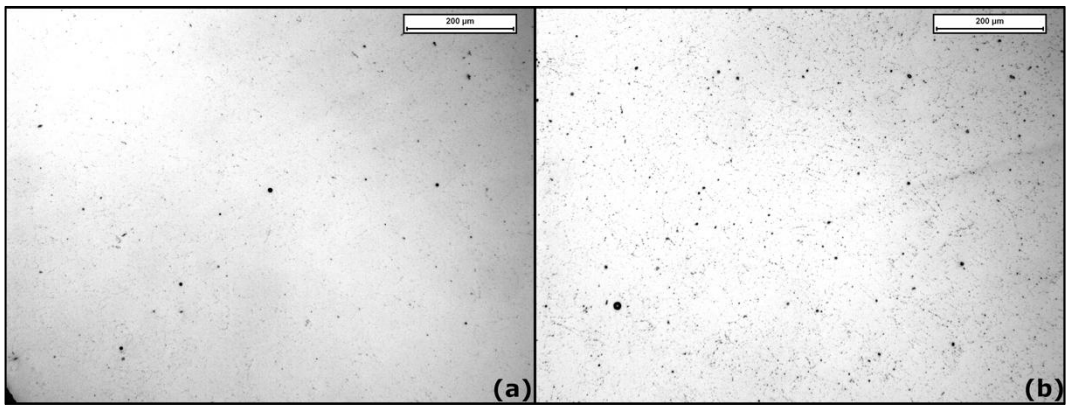

Fig. 47 Density analysis of sample 4 along (a) surface and (b) core

Table 14 Defect analysis summary of Sample 4

Sample 4	Av. Defects diameter [µm]	St. Dev.	Av. Vol. Porosities [%]	St. Dev.	Av. Aspect Ratio	St. Dev.
Surface	1.939	2.636	0.085	0.109	1.570	0.686
Core	2.428	2.010	0.120	0.048	1.422	0.464

From the density analysis of sample 4, it is observed that the average defect diameter, both along the edge and in the core, is similar to previously recorded values. However, there is a higher amount of residual porosity in this sample, especially in the core. Nevertheless, analysing the average shape ratio reveals that these defects are slightly more spherical compared to those recorded in previous samples. This is further confirmed by the histogram shown in Fig. 48, where it is evident that the highest density value class is between 0.9 and 1.1. For this sample, it is also important to note the presence of a second high-density value class in the range of 1.9 - 2.1, indicating the presence of some porosities with a higher shape ratio and, therefore, a less spherical morphology.

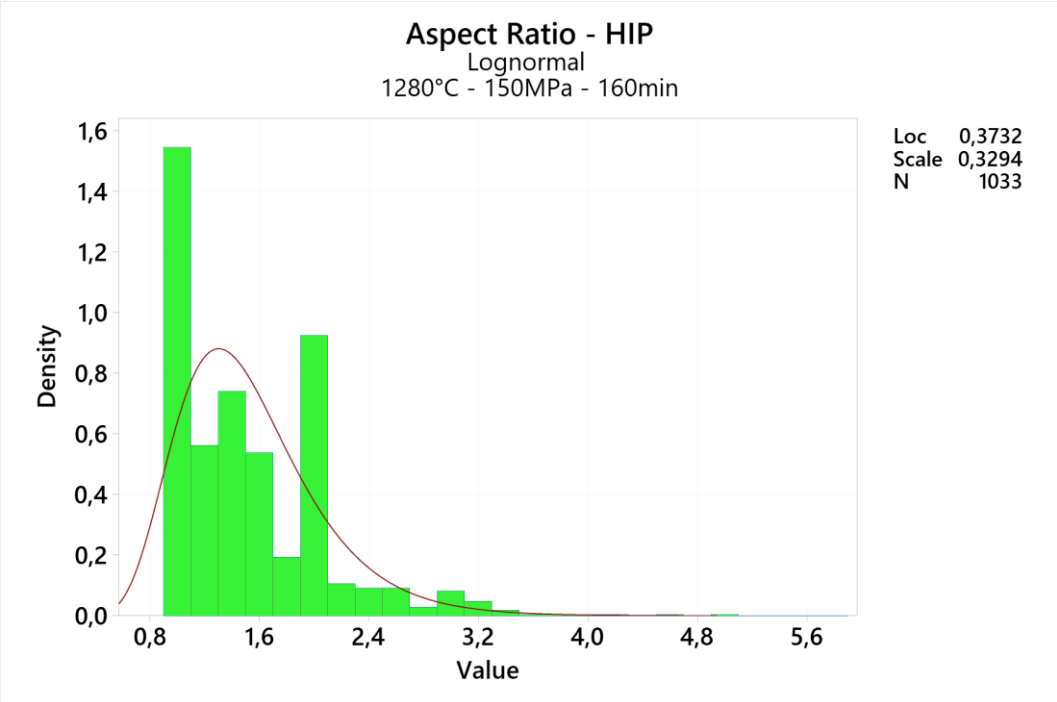

Fig. 48 Aspect ratio histogram of the Sample 4: 1280 °C - 150 MPa - 160 min

In Fig. 49, the grain microstructure of sample 4 is shown. In this case, a bimodal grain size distribution can be qualitatively observed, with larger grains surrounded by smaller ones. The average grain diameter was recorded around 102 μm, which is higher than those recorded for samples treated at 1290 °C. In addition, it is reported how grain growth in specimens treated at temperatures above 1270 °C, is inhibited by the presence of second phases, especially MC-type carbides, since the inert precipitates exert a stable pinning force on the grain boundaries [60]. The latter could be verified by SEM analysis.

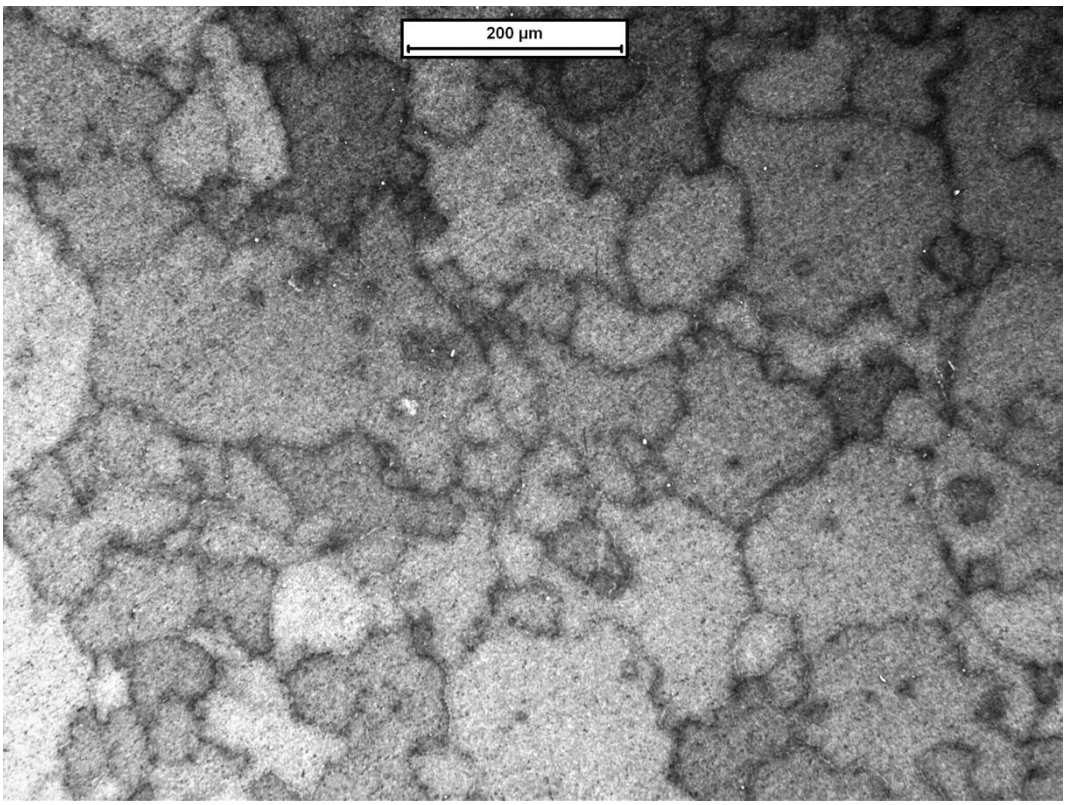

Fig. 49 Grain microstructure of Sample 4 with optical microscope at 100× magnification

The previously made observations can be confirmed by the SEM analysis of the following sample. In Fig. 50 it is shown the presence of the γ' phase of very fine dimensions and homogeneously distributed over the entire surface. Additionally, it is noticeable that, in this case, carbides of various sizes are present. Furthermore, to revealing the grain boundaries using Kalling as a chemical etchant, was particularly challenging.

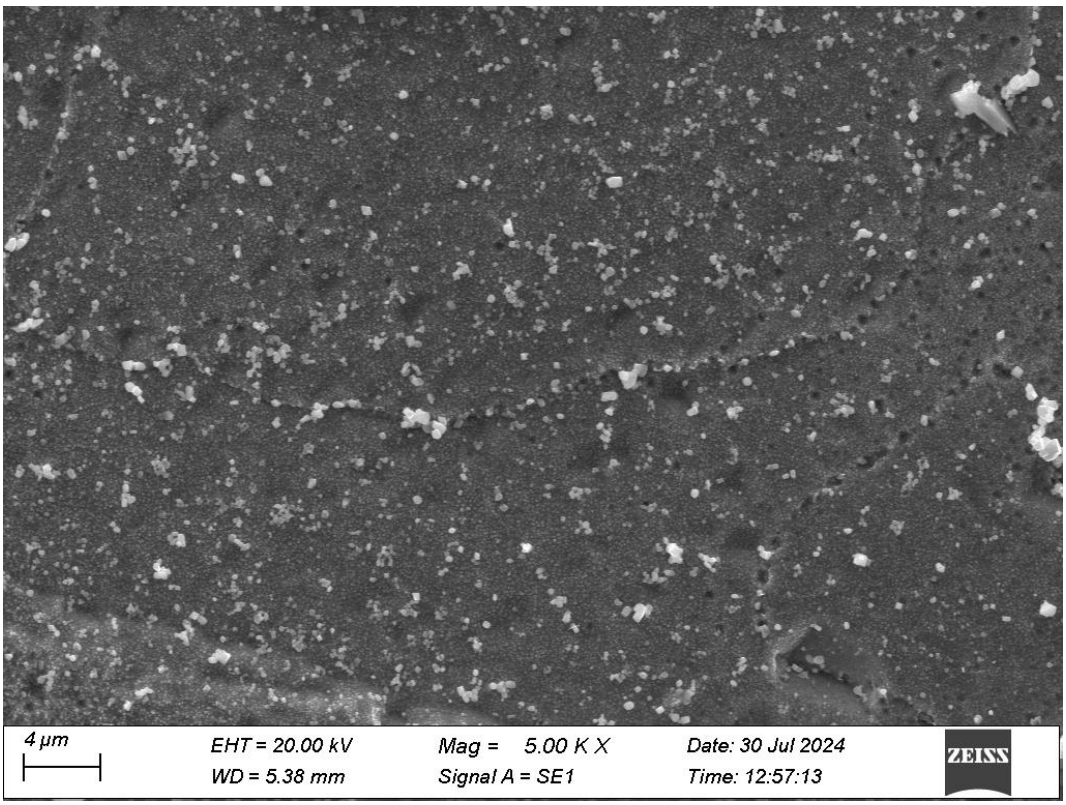

Fig. 50 SE1 signal showing the presence of a considerable amount of carbides over the entire surface of the sample 4

Moreover, when observing the areas adjacent to the carbides at higher magnifications, a marked decrease in the γ' phase can be seen near the carbides or, at most, it is present with nanometric dimensions. Additional confirmation is provided by Fig. 51, where this phenomenon can be observed even more clearly.

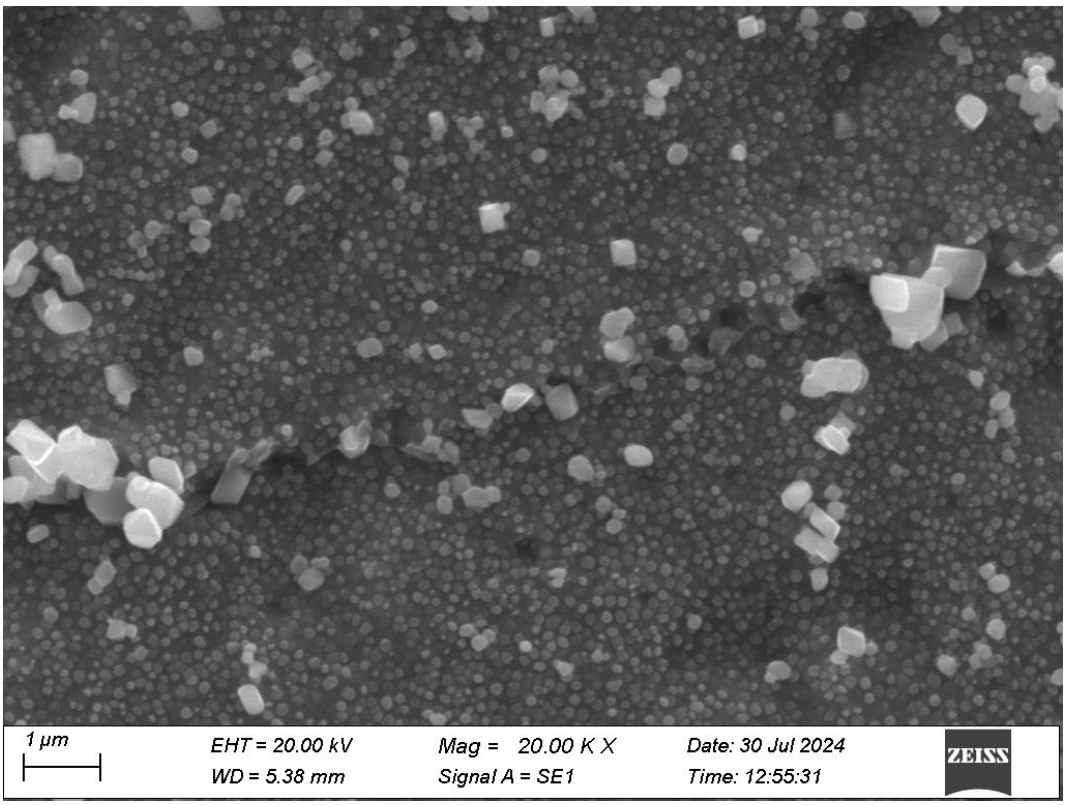

Fig. 51 SE1 signal showing a higher magnification of γ' phase nanometric structure

A possible explanation for this behaviour could be that, at 1280 °C, this alloy exhibits greater Ti segregation at the grain boundaries, resulting in the formation of MC and $M_{23}C_6$ carbides. This also coincides with a reduction in Ti in the γ' phase, which could explain why it has a smaller size compared to samples treated at 1290 °C, and why the electrolytic etchant, rather than Kalling, was used to reveal the grain microstructure. It is important to remember that Kalling has the effect of removing γ', while the electrolytic etchant acts on the γ matrix.

3.3.5. Sample 5: 1280 °C – 125 MPa – 80 min

Fig. 52 shows representative defect images for both near-edge sample 5 surface, Fig. 52(a) and core, Fig. 52(b). Table 15, on other hand, shows a summary of sample's flaws data.

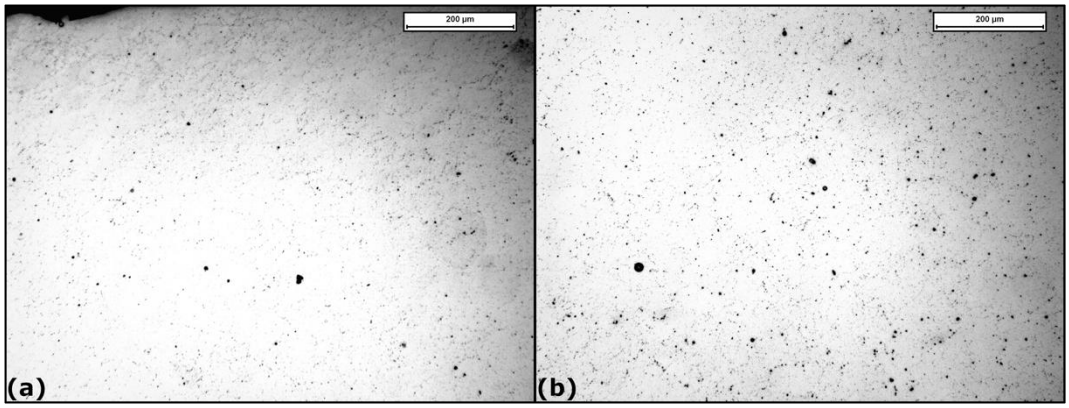

Fig. 52 Density analysis of sample 5 along surface (a) and core (b)

Table 15 Defect analysis summary of Sample 5

Sample 5	Av. Defects diameter [µm]	St. Dev.	Av. Vol. Porosities [%]	St. Dev.	Av. Aspect Ratio	St. Dev.
Surface	3.018	2.272	0.112	0.059	1.457	0.590
Core	3.240	2.359	0.184	0.087	1.396	0.471

In Table 15 the data show that this sample has the highest mean residual porosity, both on the surface and at the core. This is also evident from the images in Fig. 52, where a greater concentration of carbides can be qualitatively observed across the surface. Additionally, it is noticeable that the average defect diameter is significantly larger than that in the previous sample, while the shape ratio has decreased, reaching values below 1.5. This suggests that a higher amount of porosity remains after HIP treatment, but at the same time, the residual porosity has a more circular shape, indicating it may be gas porosity. This is further confirmed by the histogram in Fig. 53, where the highest density peak corresponds to the class range of 1.1 - 1.3; although the greatest density of recorded values falls within a shape ratio range of 0.9 to 1.5.

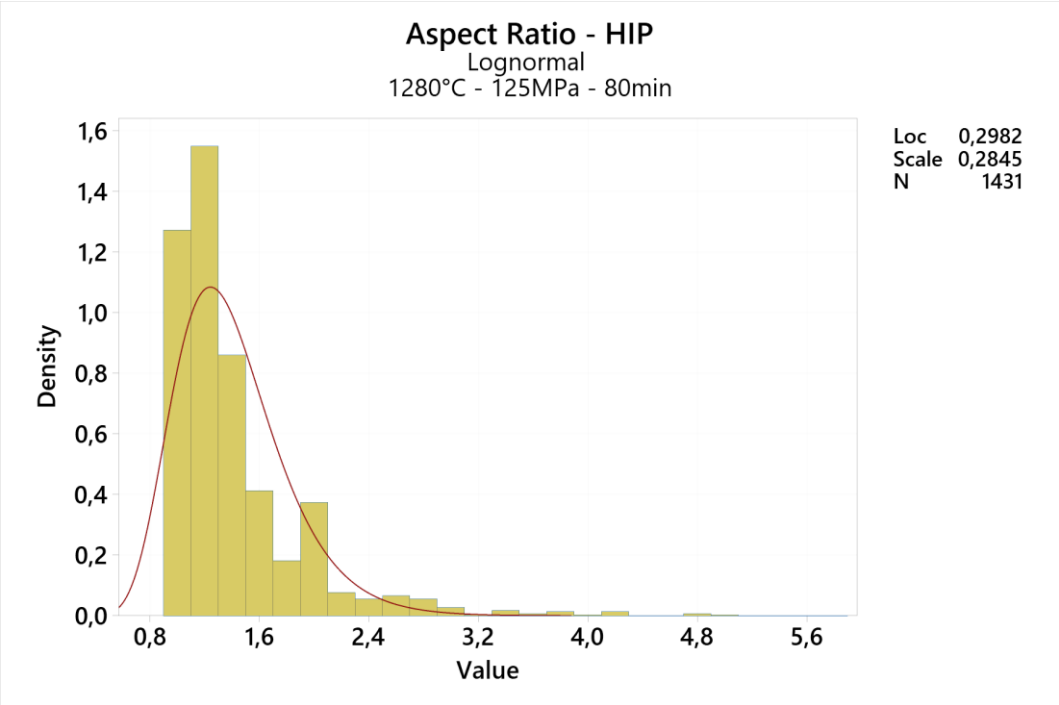

Fig. 53 Aspect ratio histogram of the Sample 5: 1280 °C - 125 MPa - 80 min

Fig. 54 shows the grain microstructure of sample 5. From the following image, it can be seen that, overall, the grains in this sample have reached a considerable size. This suggests that, for this HIP treatment, significant grain recrystallization occurred. As a result, this sample has a higher average grain diameter compared to previously recorded values, reaching 110 µm. However, this behaviour is different from that observed with sample 4; the grain morphology is no longer distinctly bimodal, and it is more challenging to distinguish the presence of grain boundaries.

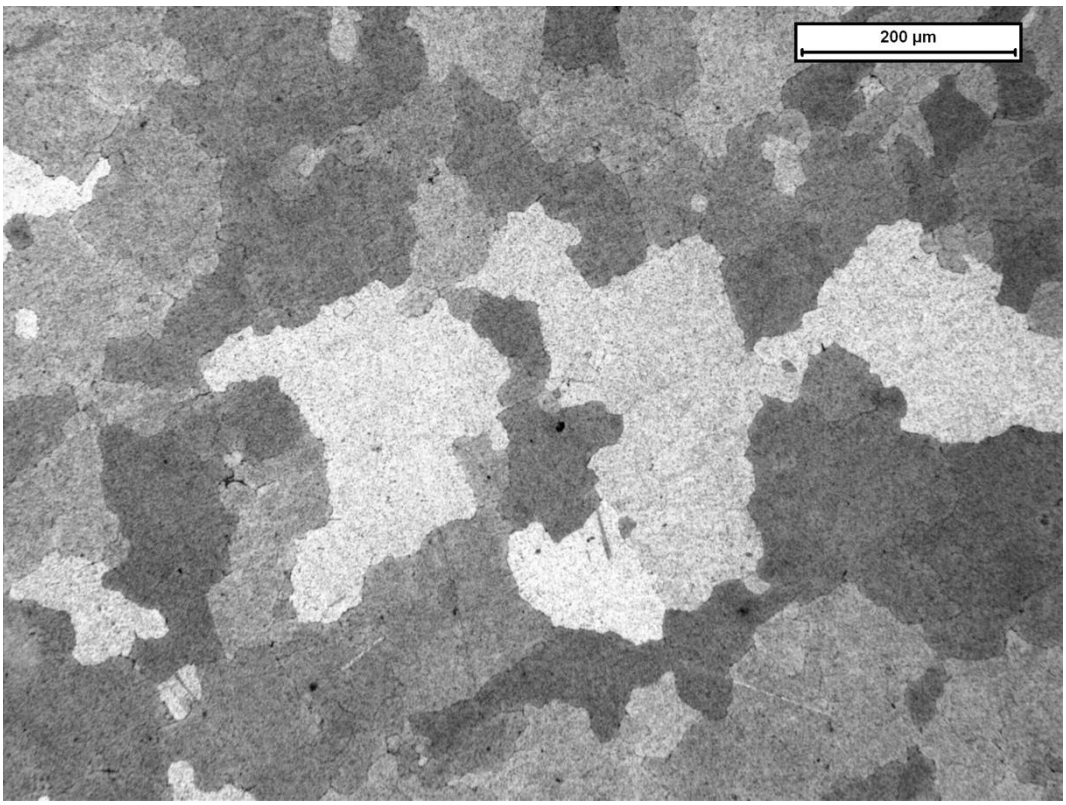

Fig. 54 Grain microstructure of Sample 5 with optical microscope at 100x magnification

One aspect to consider is that, compared to the previous sample, in this case it was possible to highlight the grain microstructure using Kalling as a chemical etchant. This could suggest that, in this sample, Ti is not predominantly present in the carbides, but also in the γ' phase.

This can be confirmed by analysing the sample using SEM. Observing Fig. 55, it can be seen that, unlikely what was previously observed, an extremely fine γ' phase and a higher concentration of carbides are consistently present. Moreover, the carbides are no longer positioned along the grain boundaries but are randomly dispersed across the entire surface.

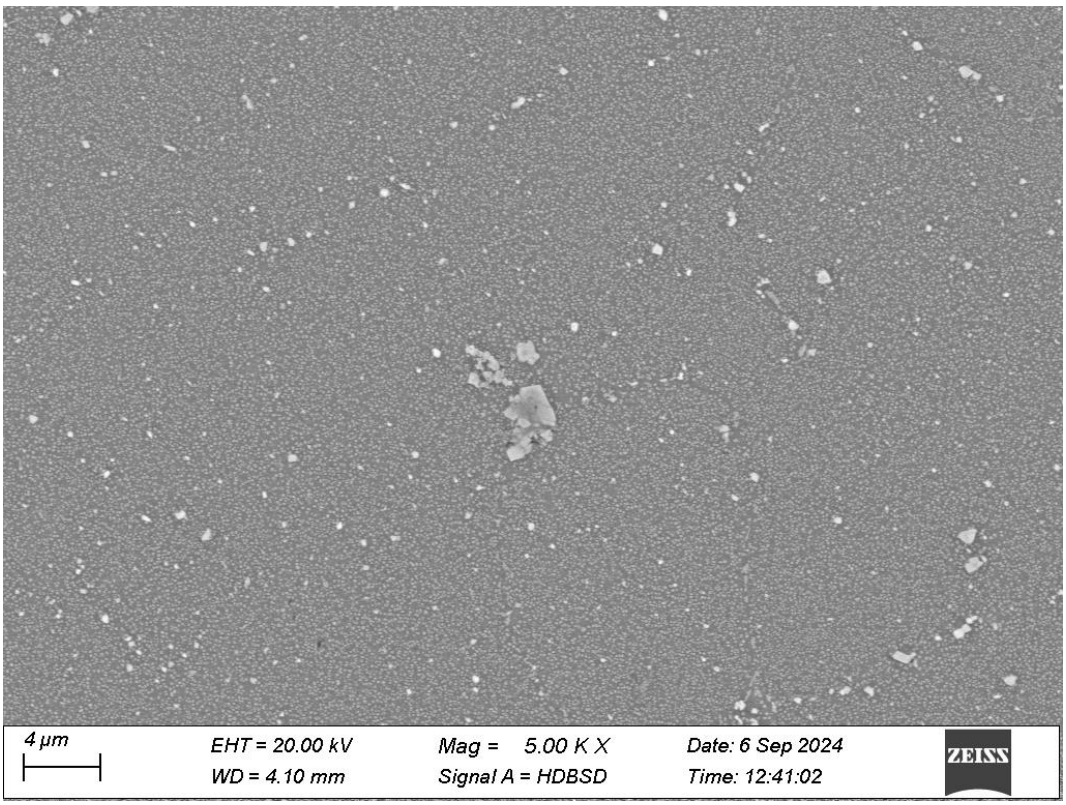

Fig. 55 BSD signal showing the uniform dispersion of fine γ' within the grain structure and the random distribution of carbides

In addition, in Fig. 56(a), which shows a close-up of a possible set of MC-type carbides, it can be noted that γ' is no longer present around the carbides or, if present, only in nanometric dimensions. This phenomenon could still be linked to Ti segregation, as introduced with the previous sample. In Fig. 56(b), there is an area where this effect is even more pronounced and visible.

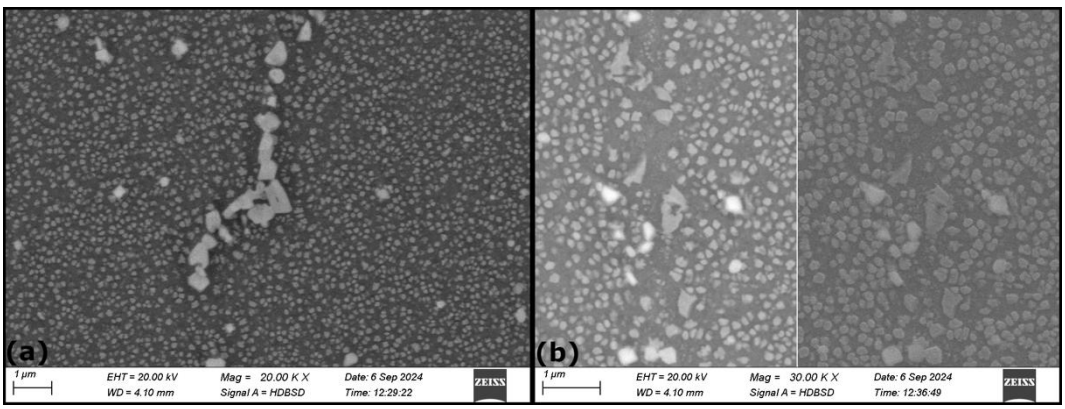

Fig. 56 BSD signal showing (a) no presence of γ' phase around the MC carbides and (b) higher magnification, of different spot, with no γ' phase along the centre zone

However, unlike before, here Kalling's etching still managed to reveal the granular microstructure. This contradiction might be related to the holding time at the temperature of 1280 °C. In fact, by halving the process time, it is likely that Ti segregation occurred only near the previously formed carbides, whereas in areas distant from the carbides, the Ti present in the γ' phase remained in solution within it.

3.3.6. Sample 6: 1280 °C – 100 MPa – 240 min

Fig. 57 shows images of the remaining defects both near edge sample surface, Fig. 57(a), and core, Fig. 57(b). Instead, Table 16 provides a summary of the analysis conducted on the density of the following sample.

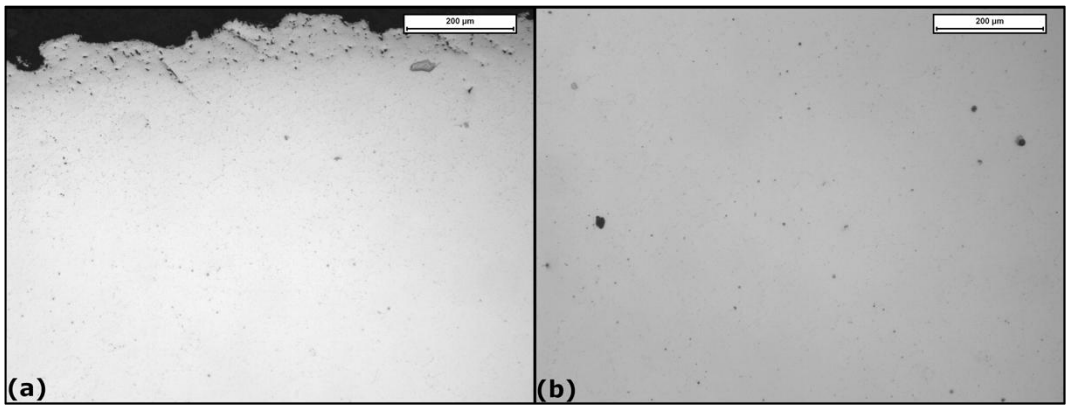

Fig. 57 Density analysis of sample 6 along surface (a) and core (b)

Table 16 Defect analysis summary of Sample 6

Sample 6	Av. Defects diameter [µm]	St. Dev.	Av. Vol. Porosities [%]	St. Dev.	Av. Aspect Ratio	St. Dev.
Surface	1.880	1.412	0.070	0.054	1.550	0.549
Core	2.191	1.886	0.070	0.040	1.494	0.551

Analysing the data presented in Table 16 summary, it is evident that this sample has the same average residual porosity, both along the edge and at the core. The defects present have an average shape ratio of approximately 1.5, indicating a spherical morphology likely associated with gas porosity.

The average defect diameter also shows values consistent with previous observations, with a slightly higher value at the core compared to the edge of the surface. Finally, the histogram in Fig. 58 shows that the highest density of recorded values falls within the 0.9 - 1.1 range, confirming a greater presence of defects attributable to gas porosity. It is also interesting to note a second peak in the 1.9 - 2.1 range, which corresponds to porosity with a more complex shape.

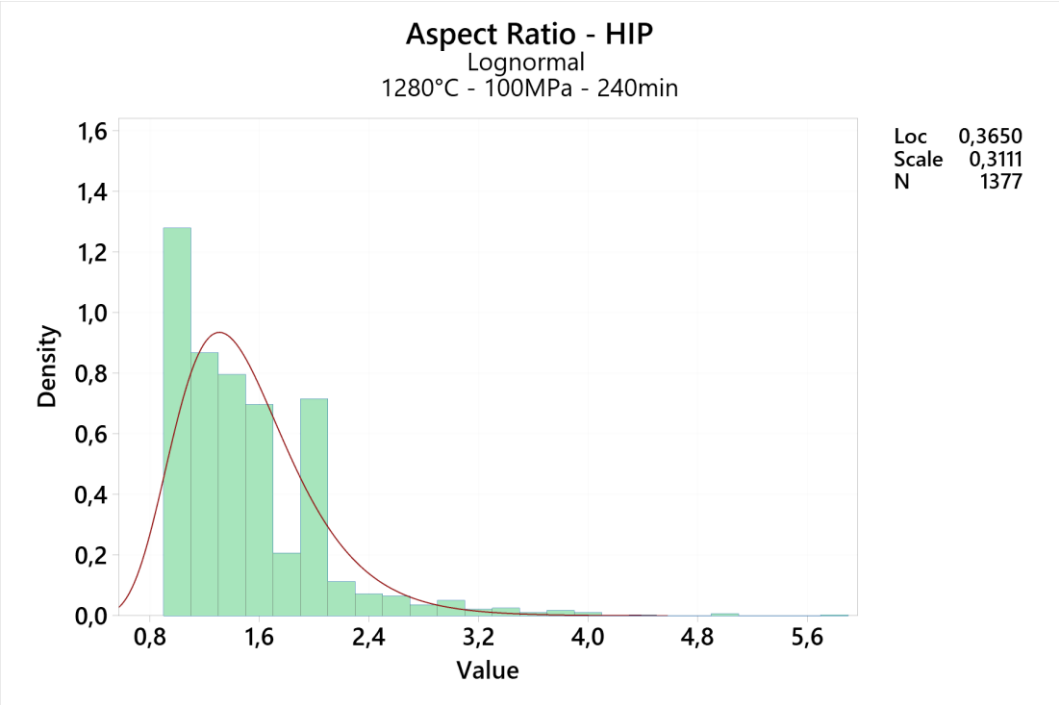

Fig. 58 Aspect ratio histogram of the Sample 6: 1280 °C – 100 MPa – 240 min

Fig. 59 shows the grain microstructure of the following sample. From this microstructure, various pieces of information can be inferred, linking to the discussion of other samples treated at 1280 °C. Firstly, we observe again a bimodal grain size distribution, with larger grains surrounded by many smaller grains and a mean grain diameter value of 89 µm is recorded, the lowest parameter among the three samples treated at 1280 °C. At this magnification, it is possible to see several precipitates at the grain boundaries (appearing as white dots), which may indicate the presence of carbides. As mentioned previously, these carbides inhibit grain growth by exerting a pinning force on the grain boundaries.

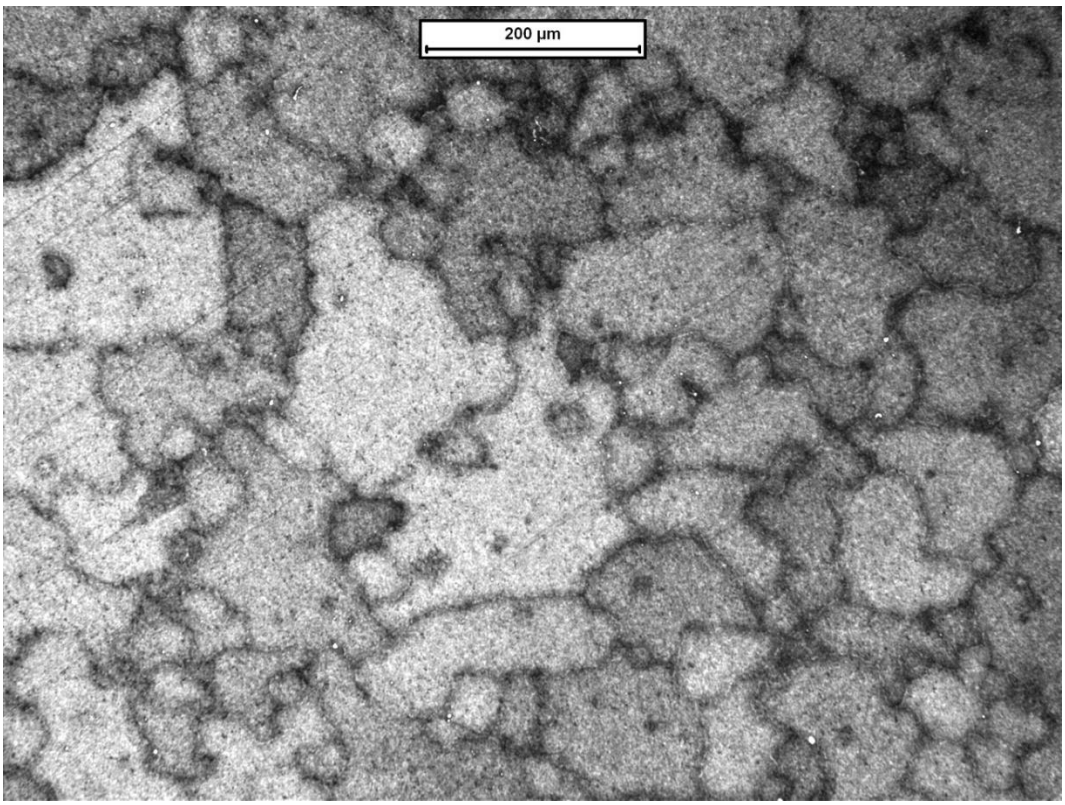

Fig. 59 Grain microstructure of Sample 6 with optical microscope at 100× magnification

Lastly, the image was obtained using electrolytic etching rather than Kalling's reagent, indicating titanium segregation towards the carbides and reducing the presence of the γ' phase. This last observation will be analysed in detail using SEM analysis. In Fig. 60, images of the sample surface are shown, confirming the previous observations.

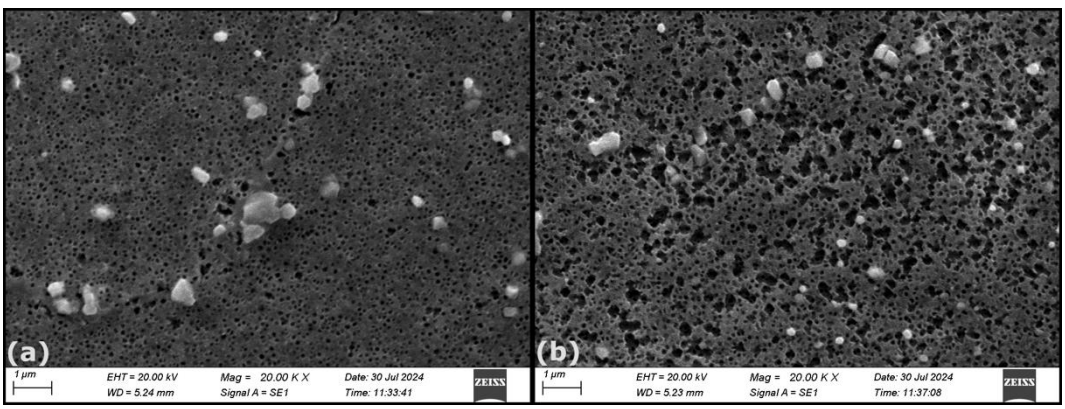

Fig. 60 SE1 signal (a) showing the total absence of γ' phase in the sample, and (b) further magnification highlighting a high concentration of voids due to the lack of γ'.

In fact, from Fig. 60(a), it is evident that the γ' phase is no longer present on the sample surface, only its imprints remain. This phenomenon indicates that, in this case, the processing time was sufficient to allow a complete segregation of Ti from the γ' phase into carbides. Additionally, a high concentration of $M_{23}C_6$ and MC carbides was observed across the entire surface. In Fig. 60(b), this phenomenon is displayed even more prominently, showing a high density of voids present. SEM observation also revealed additional features in this sample, which are shown in Fig. 61.

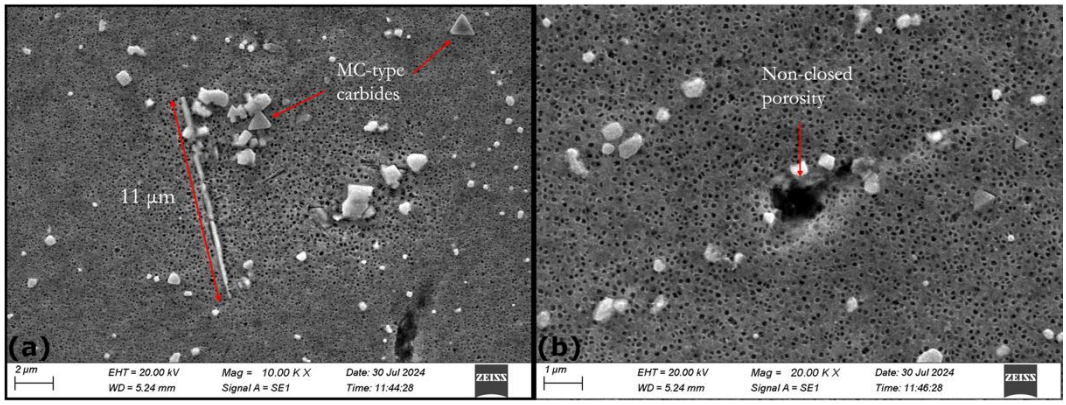

Fig. 61 SE1 signal showing (a) the appearance of a well-developed acicular $M_{23}C_6$ carbide and (b) gas porosity trapped during the LPBF process and not healed during the HIP treatment.

Specifically, Fig. 61(a) displays an $M_{23}C_6$ carbide with a needle-like morphology, approximately 11 µm in length. The acicular form of this carbide is detrimental to the mechanical properties, as the pointed ends could act as initiation sites for possible cracks. However, this specific carbide is not problematic on its own, as the material will undergo further heat treatments before being put into service to homogenize the microstructure. Another noteworthy observation in this image is the presence of other types of carbides, specifically triangular-shaped ones associated with MC carbides and more complexly shaped ones, belonging to the M_6C class. Finally, in Fig. 61(b), there is an indication of what could be residual porosity from the printing process, with an area of approximately 2 µm², likely resulting from trapped gas.

In summary, for the last three samples treated at 1280 °C, a very different behaviour was observed compared to those treated at 1290 °C, particularly regarding the phenomenon of Ti segregation, which was not present in the first three samples. It is also possible to make observations related to the presence of residual porosities and their aspect ratios. In Fig. 62, boxplot diagrams show a comparison of the total porosities recorded in the three samples, with values slightly higher than those obtained for the samples treated at 1290 °C.

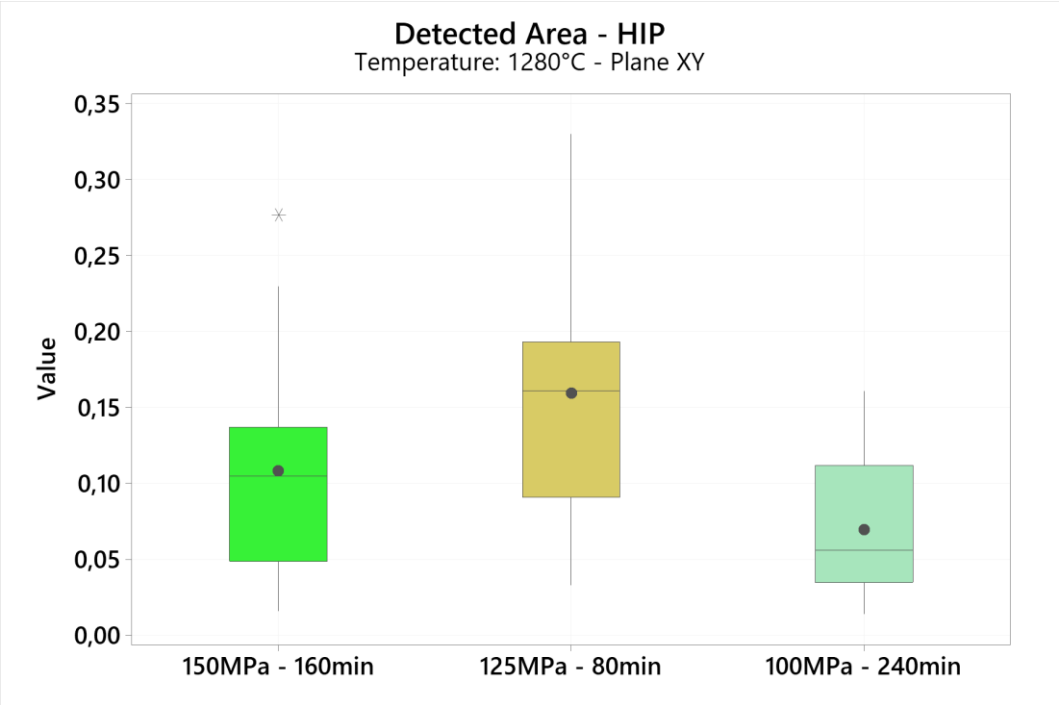

Fig. 62 Summary boxplot of residual porosity of the sample 4, 5 and 6 with the same process temperature, i.e. 1280 °C

Nonetheless, even at this temperature, an overall decrease in residual porosity was observed compared to the as-built samples. Additionally, the histogram in Fig. 63 shows that almost all recorded aspect ratio values fall within the ranges of 0.9 - 1.1 and 1.9 - 2.1, indicating that the observed porosities do not deviate significantly from those typically associated with gas porosities, with only a few exceptions.

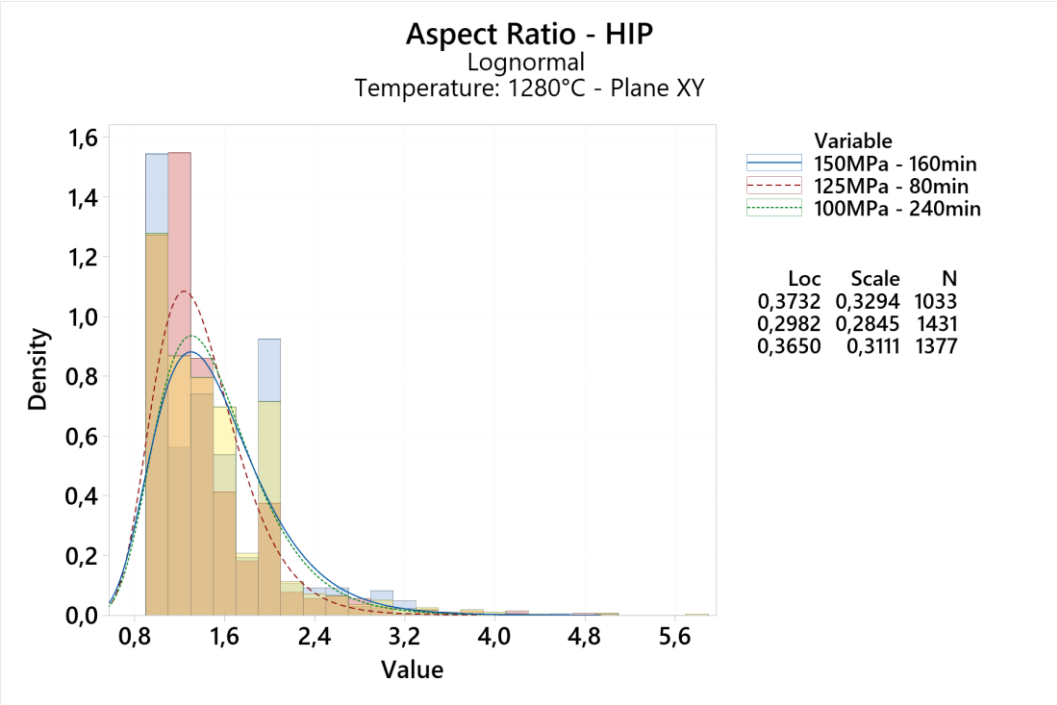

Fig. 63 Summary aspect ratio histogram of the sample 4, 5 and 6 with the same process temperature, i.e. 1280 °C

Finally, Fig. 64 shows a comparison of the average grain diameters recorded, revealing that the values obtained are generally higher than those for the treatment at 1290 °C, indicating greater grain development and growth at 1280 °C.

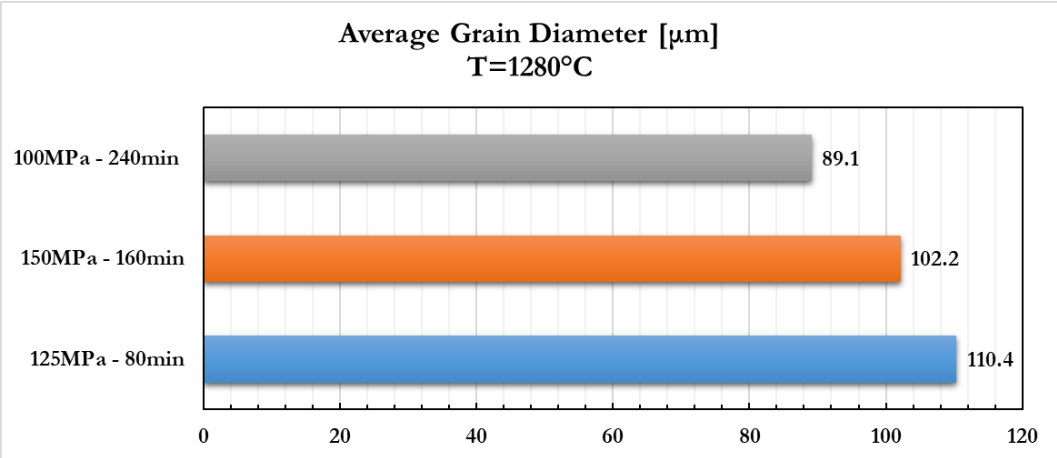

Fig. 64 Summary average grain diameter histogram of the sample 4, 5 and 6 with the same process temperature, i.e. 1280 °C

It is also interesting to note that as the process duration increases, the average grain diameter decreases. This phenomenon could be related to the increased concentration of carbides, which act as regulators of grain growth by exerting a pinning force on the grain boundaries. As is well known, grain enrichment improves resistance to viscous flow, thus preventing high-temperature viscous sliding and serving as anchoring points for adjacent grains.

3.3.7. Sample 7: 1270 °C – 150 MPa – 80 min

Fig. 65 shows illustrative images of the sample's flaws located both near the edge, Fig. 65(a) and at the core, Fig. 65(b). Meanwhile, Table 17 provides a summary with data related to the residual defect analysis.

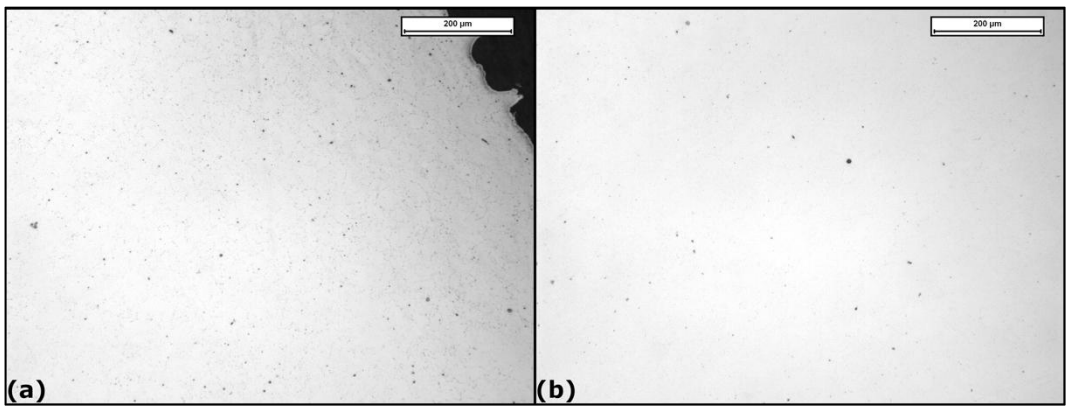

Fig. 65 Density analysis of sample 7 along surface (a) and core (b)

Table 17 Defect analysis summary of Sample 7

Sample 7	Av. Defects diameter [µm]	St. Dev.	Av. Vol. Porosities [%]	St. Dev.	Av. Aspect Ratio	St. Dev.
Surface	2.099	1.407	0.042	0.023	1.483	0.486
Core	2.128	1.555	0.029	0.013	1.543	0.547

The results obtained from the defect analysis of the sample reveal a microstructure with the lowest percentage of residual porosity recorded among all samples, both near the edge and at the core. The average values related to the diameters of the porosities are also lower compared to previous samples, and the average shape ratio indicates that these defects have a similar parameter at both the edge and core, around 1.5. This suggests that the defects

mainly result from gas porosity remaining from the LPBF process. Moreover, observing the histogram shown in Fig. 66, it can be seen that the highest density of recorded values is distributed between two classes, namely 0.9 - 1.1 and 1.3 - 1.5, further confirming the presence of primarily spherical, non-damaging defects for the material. Additionally, for this sample, a lower density peak is observed in the 1.9 - 2.1 class, indicating a smaller amount of porosity with a more complex morphology.

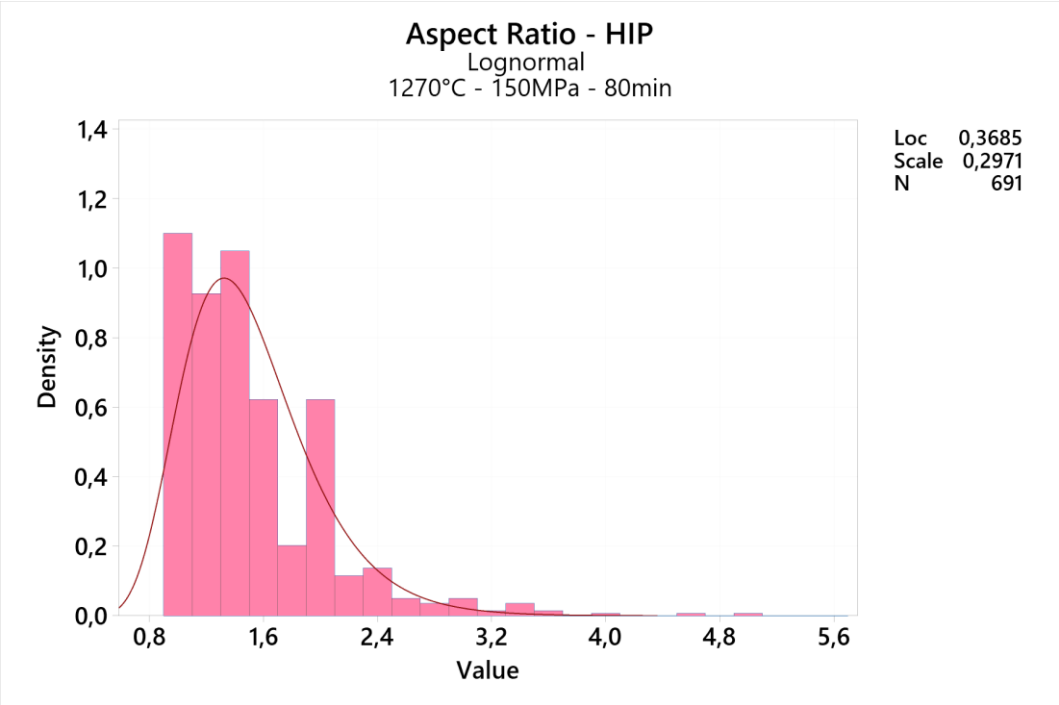

Fig. 66 Aspect ratio histogram of the Sample 7: 1270 °C – 150 MPa – 80 min

The next step was to analyse the grain microstructure obtained, as shown in Fig. 67. The first observation concerns the average grain size which, compared to previous samples, is significantly smaller, recording a value of 35 µm. This substantial size difference could be related to the fact that at a temperature of 1270 °C, the material enters the recrystallization zone. This is confirmed by the fact that, compared to the as-built material, the characteristic microstructure left by the LPBF process has been completely replaced by small, randomly oriented grains. However, it seems that the short processing time the sample was subjected to, may not have been sufficient to allow the development of larger grains.

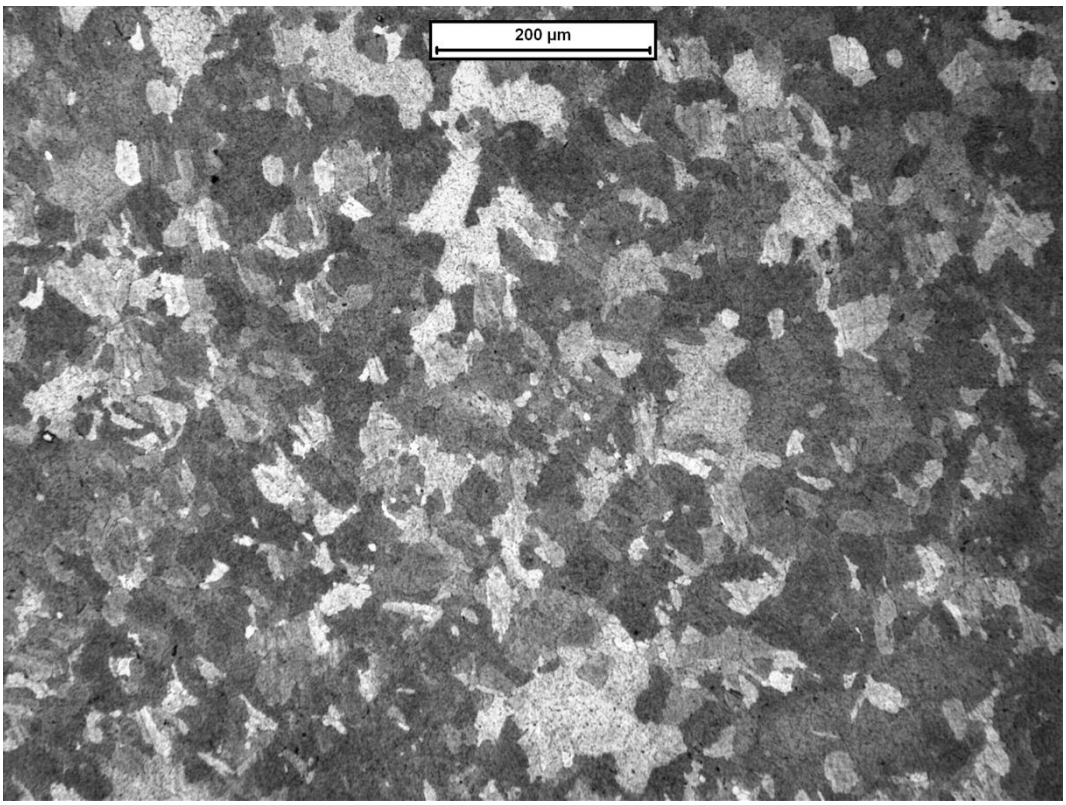

Fig. 67 Grain microstructure of Sample 7 with optical microscope at 100× magnification

Of course, the fact that the grains are not as developed as, for example, in the case of sample 6, should not be associated with a high concentration of grain boundary carbides inhibiting grain growth, and this is confirmed by SEM observations of the following sample. In Fig. 68(a), a portion of the sample surface is shown using two different signals, SE and BSD.

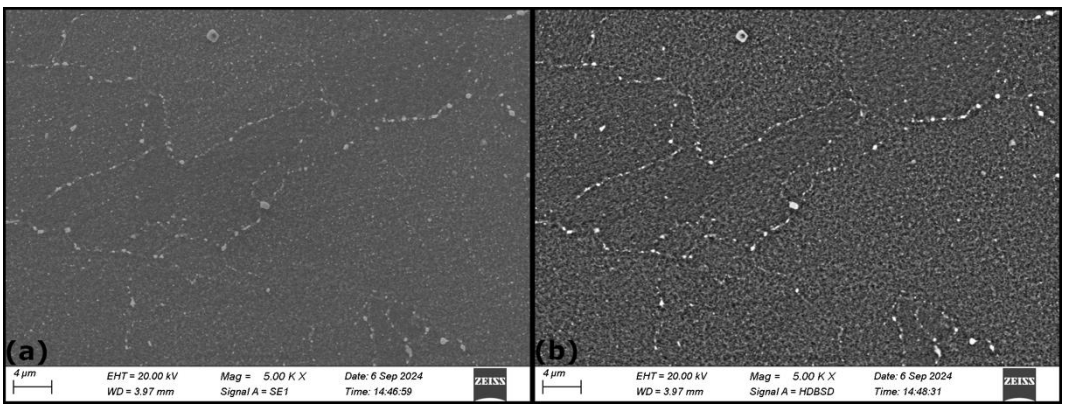

Fig. 68 Same spot analysed with (a) SE1 signal and (b) BSD signal showing the presence of decorated grain-boundaries with $M_{23}C_6$-type carbides

In particular, Fig. 68(b) shows that there is no high concentration of carbides (mainly of the $M_{23}C_6$ type) across the entire surface; rather, they are mainly concentrated at grain boundaries, enriching them. A small concentration of possible M_6C type carbides is also seen within the grain, and, finally, a fine and uniformly distributed γ' phase is present. The fine structure of γ' was also observed by Attallah and Terasaki, who found that the RR1000 superalloy, also a γ'-strengthened Ni-based superalloy produced by powder metallurgy and treated at 1270 °C, exhibited a uniform distribution of fine, rounded γ' within the grains [61]. Fig. 69 shows a further magnification of a contact point between different grains, where the enrichment from $M_{23}C_6$ carbides along the grain boundary is visible. Additionally, this image allows a more detailed observation of the fine size of the γ' phase.

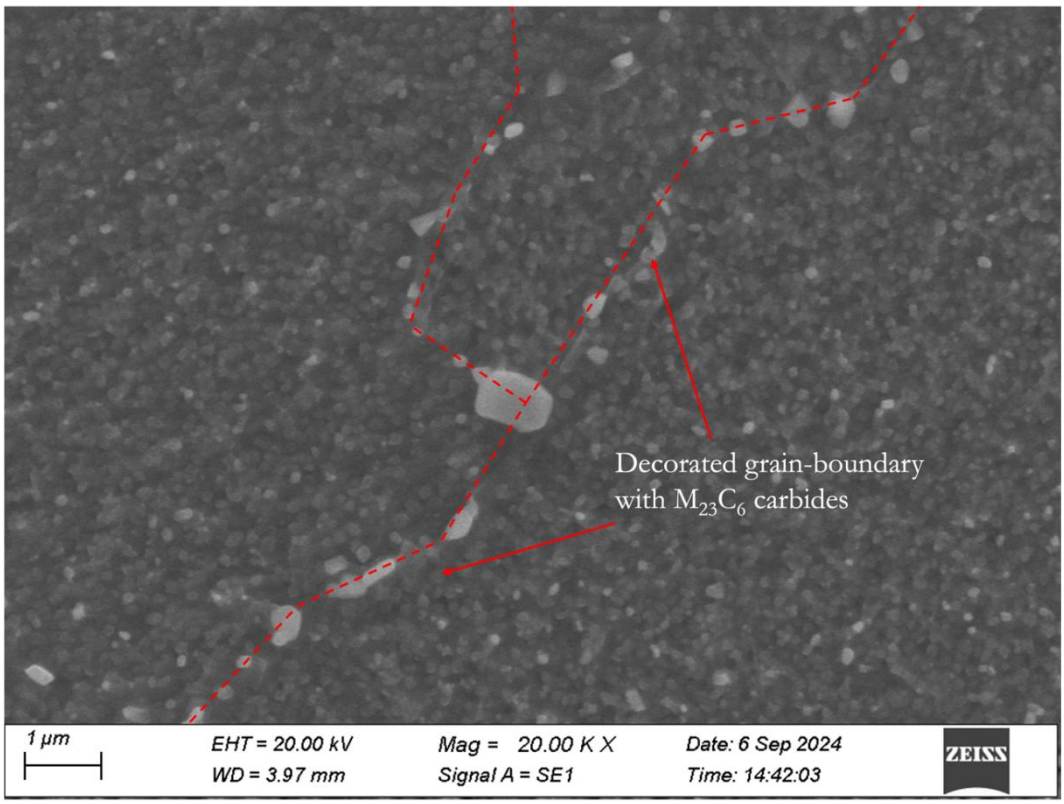

Fig. 69 SE1 signal showing a higher magnification of decorated grain-boundaries carbides

3.3.8. Sample 8: 1270 °C – 125 MPa – 240 min

Fig. 70 shows sample 8 surfaces in the near-edge Fig. 70(a) and the core Fig. 70(b) location. Instead, Table 18 shows the summary of the specimen density analysis.

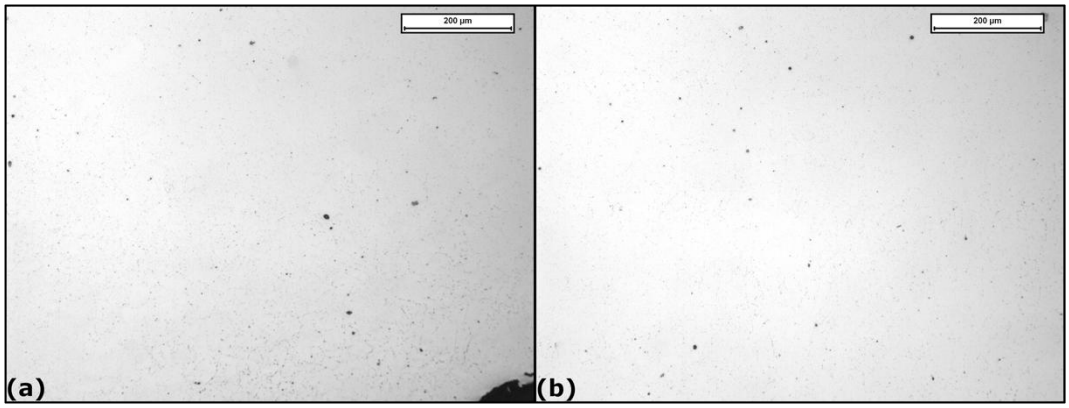

Fig. 70 Density analysis of sample 8 along surface (a) and core (b)

Table 18 Defect analysis summary of Sample 8

Sample 8	Av. Defects diameter [µm]	St. Dev.	Av. Vol. Porosities [%]	St. Dev.	Av. Aspect Ratio	St. Dev.
Surface	2.914	1.914	0.052	0.021	1.435	0.477
Core	2.287	1.739	0.040	0.012	1.562	0.560

From the data collected during the defect analysis, as shown in Table 18, it is evident that the average residual porosity is in line with the previous sample, with a slightly higher value recorded along the edge of the sample compared to the core. At the same time, an increase in the average diameter of defects can also be observed, especially for porosities located on the sample edge, where an average value of about 3 µm is recorded. Finally, for this sample, it can be concluded that, given the recorded mean shape ratio value of approximately 1.5 (for both the edge and the core), the results are consistent.

Furthermore, as shown in Fig. 71, which displays the histogram of all values for the shape ratio, the peak with the highest density of values corresponds to the 1.1 - 1.3 range. It is also interesting to note that the peaks with lower density still fall within value classes that do not exceed 1.5; specifically, the 0.9 - 1.1 and 1.3 - 1.5 classes are observed. All this suggests that, for most defects, the morphology is approximately spherical and attributable to gas porosity formed during the LPBF process.

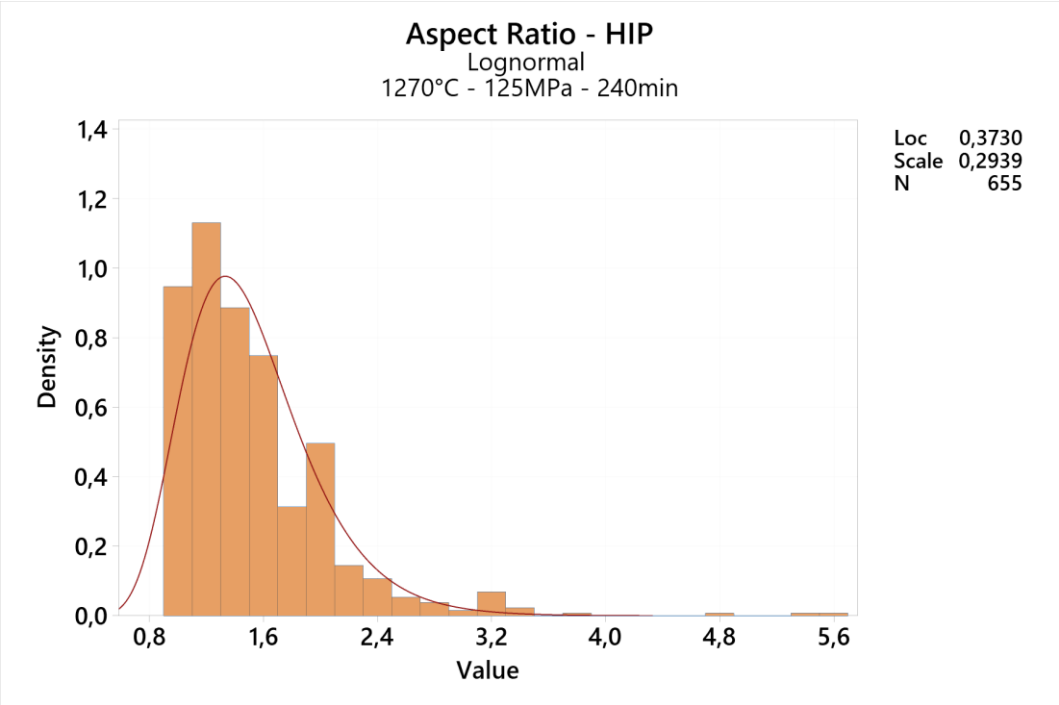

Fig. 71 Aspect ratio histogram of the Sample 8: 1270 °C – 125 MPa – 240 min

Fig. 72 shows the grain microstructure of sample 8. This sample recorded the highest absolute average grain diameter, approximately 160 µm. Complete recrystallization of the microstructure is observed, with equiaxed grains and a bimodal size distribution, as larger grains are surrounded by smaller ones.

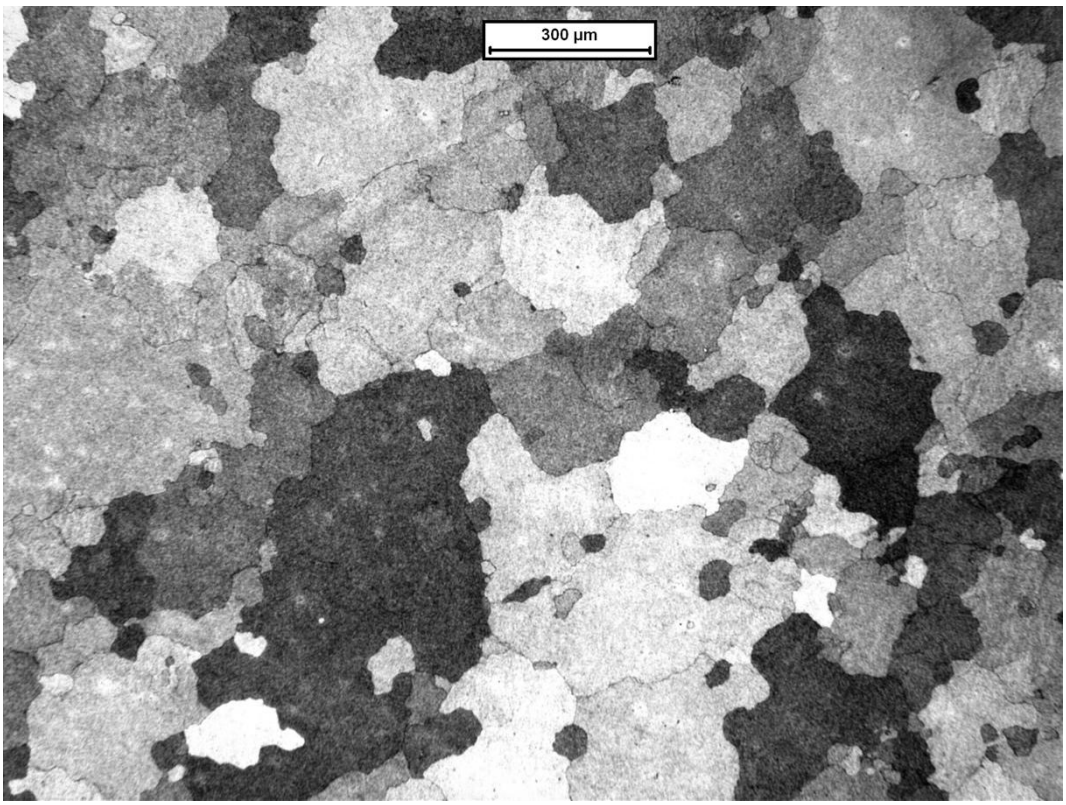

Fig. 72 Grain microstructure of Sample 8 with optical microscope at 50× magnification

The most likely hypothesis for this substantial grain growth could be the combination of temperature, Ti segregation at the grain boundary, and processing time. Specifically, according to the Arrhenius-type law that inversely correlates the diffusion rate of a given atom with temperature, the diffusion rate increases as temperature rises. Therefore, it is possible to hypothesize that at 1270 °C, Ti exhibits a lower diffusion rate, and segregation from the γ' phase toward the grain boundary occurs more slowly and over longer durations. This results in a reduced formation of $M_{23}C_6$ and MC carbides at the grain boundary. As previously mentioned, carbides at the grain boundary also play a role in regulating grain growth, exerting a pinning force on the boundary. Consequently, the reduced presence of these regulators allowed for greater grain growth. This hypothesis will need to be confirmed through SEM analysis of the sample.

In Fig. 73(a), a magnification of a spot within the grain is shown. It can be observed that nanometric MC carbides are uniformly dispersed over the surface; additionally, the presence of a fine, cuboidal γ' phase is also visible. Fig. 73(b) confirms previous observations, showing that $M_{23}C_6$-type carbides (typically elongated morphology) decorate the grain boundary, but compared to previously examined samples, are considerably smaller in size and significantly reduced in quantity. However, it is important to note that an enrichment at the grain boundary with carbides of different types, especially $M_{23}C_6$ and MC, as shown in the same figure, improves resistance to high-temperature creep deformation.

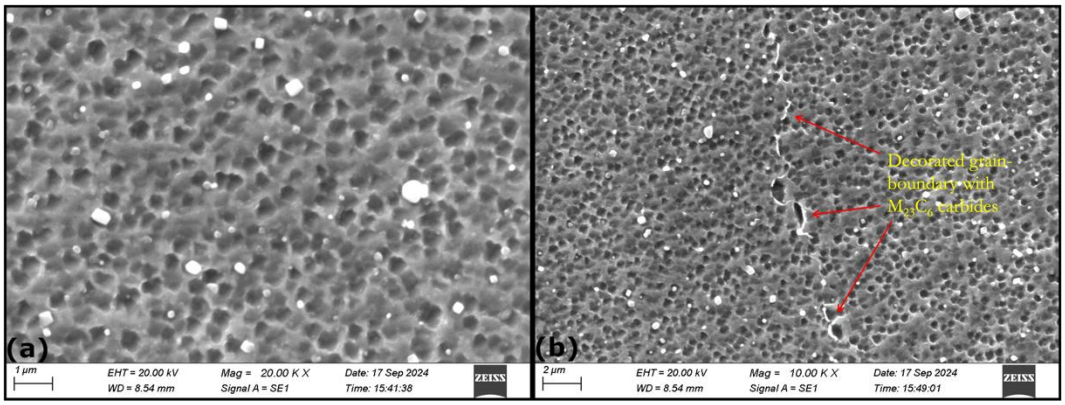

Fig. 73 SE1 signal showing (a) visible texture of cuboidal γ' phase and (b) fine $M_{23}C_6$-type carbides decorated grain boundary

3.3.9. Sample 9: 1270 °C – 100 MPa – 160 min

Fig. 74 shows defect analysis images from the sample 9 surface, both at near-edge Fig. 74(a) and core Fig. 74(b). The summary data resulting from the defects analysis is reported in Table 19.

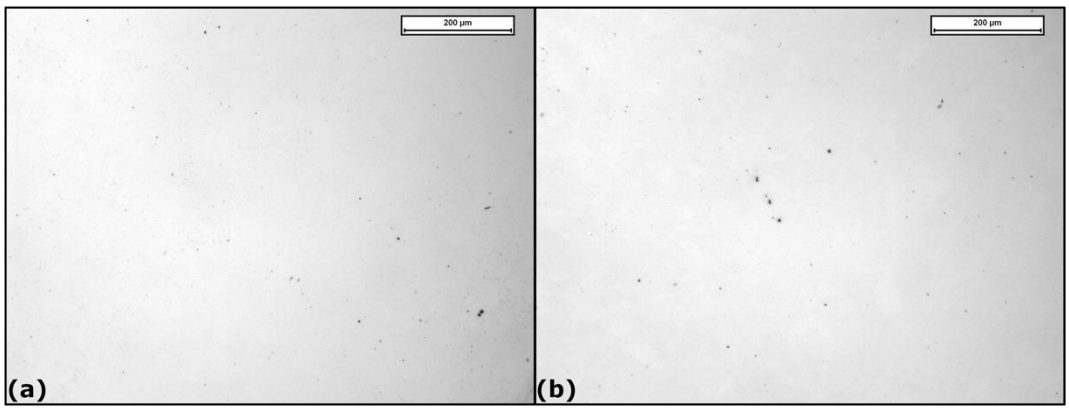

Fig. 74 Density analysis of sample 9 along surface (a) and core (b)

Table 19 Defect analysis summary of Sample 9

Sample 9	Av. Defects diameter [µm]	St. Dev.	Av. Vol. Porosities [%]	St. Dev.	Av. Aspect Ratio	St. Dev.
Surface	2.370	1.543	0.027	0.009	1.513	0.597
Core	2.174	2.238	0.025	0.027	1.493	0.576

From the analysis of defects in the latest sample, that underwent HIP treatment, the lowest recorded average residual porosity value is observed, both along the surface and at the core. As for the average defect diameter, the values are consistent with those obtained from previous samples treated at 1270 °C. Finally, the average shape ratio value also remains comparable to that of previously analysed samples.

Observing the histogram shown in Fig. 75, it can be noted that the highest density peak of values is in the 0.9 - 1.1 class, while the second highest density peak is in the 1.1 - 1.3 class. This suggests that the majority of flaws exhibits an almost spherical morphology, likely due to trapped gas in the material during the LPBF process.

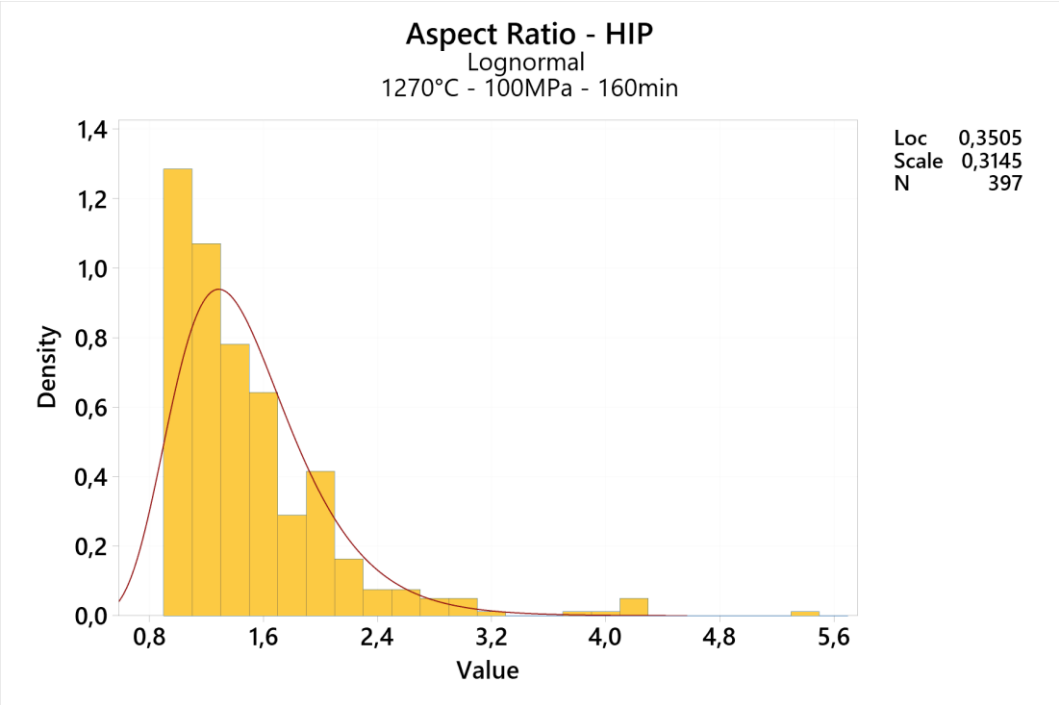

Fig. 75 Aspect ratio histogram of the Sample 9: 1270 °C – 100 MPa – 160 min

In Fig. 76, the grain size microstructure of the sample is shown, where an average grain diameter of 34 µm was recorded, which is very similar to the value obtained with sample 7. From the displayed image, it is also possible to observe that, qualitatively, the grains exhibit a bimodal size distribution. Comparisons among the three samples will be discussed later. However, compared to sample 7, a slight increase in larger grains surrounded by many smaller grains can be observed. This could be related to the longer processing time, which allowed a few grains to grow more significantly.

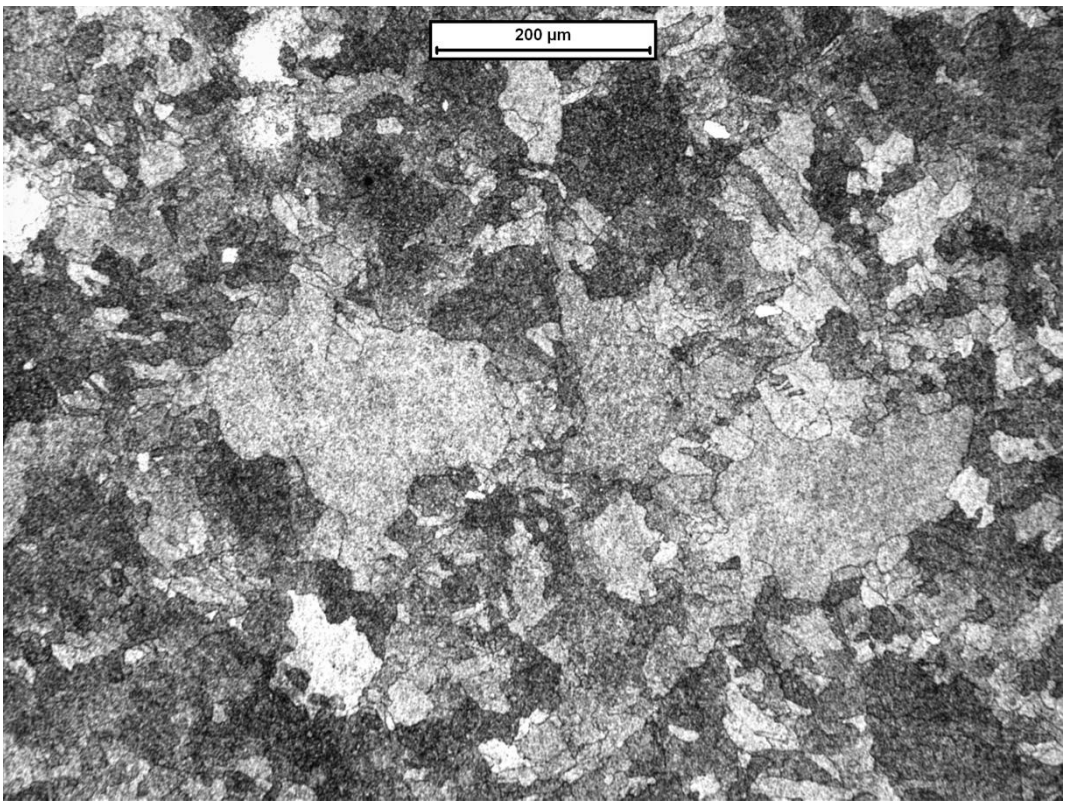

Fig. 76 Grain microstructure of Sample 9 with optical microscope at 100× magnification

The final conducted analysis involves SEM observation, where very similar aspects to the ones seen with sample 7, can be observed. In Fig. 77(a), a grain boundary enriched with carbides, presumably of the $M_{23}C_6$ type, is shown.

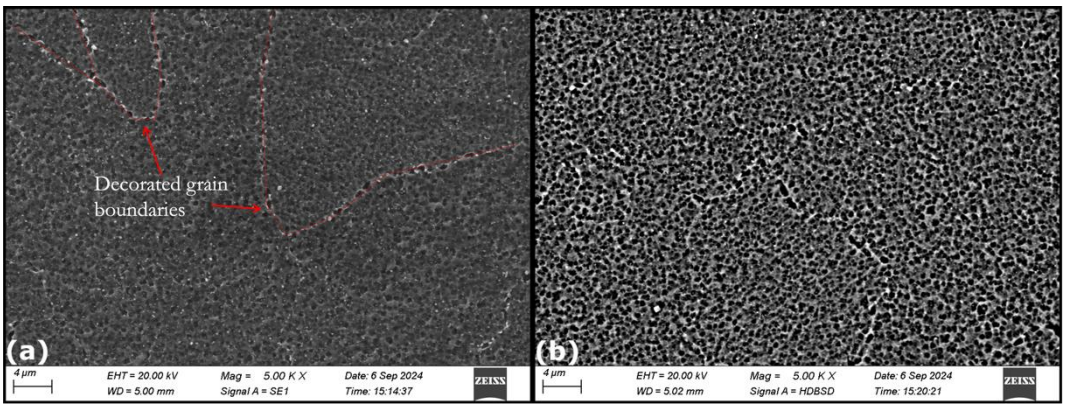

Fig. 77 (a) SE1 signal showing the presence of fine $M_{23}C_6$-type carbides decorated grain boundaries and (b) BSD signal showing γ' phase uniformly distributed on the surface

It is interesting to note that, unlike sample 7, the $M_{23}C_6$ carbides are slightly smaller, while the carbides located inside the grain, likely the M_6C type, are slightly larger. This phenomenon may be related to the prolonged exposure to the temperature of 1270 °C, as it is reasonable to assume that with increased processing time, there is a decrease in the size of $M_{23}C_6$ carbides at the grain boundary and, simultaneously, an increase in the size of internal M_6C carbides. Finally, Fig. 77(b) shows the presence of fine, uniformly distributed γ' throughout the surface, maintaining a cuboidal morphology and slightly larger at the grain boundary compared to the one within the grain.

To conclude what has been discussed so far, a comparison is presented among the three samples treated at 1270 °C, showing their differences and similarities. Fig. 78 displays a boxplot diagram related to the comparison of the residual porosities recorded across the entire surface of the three samples.

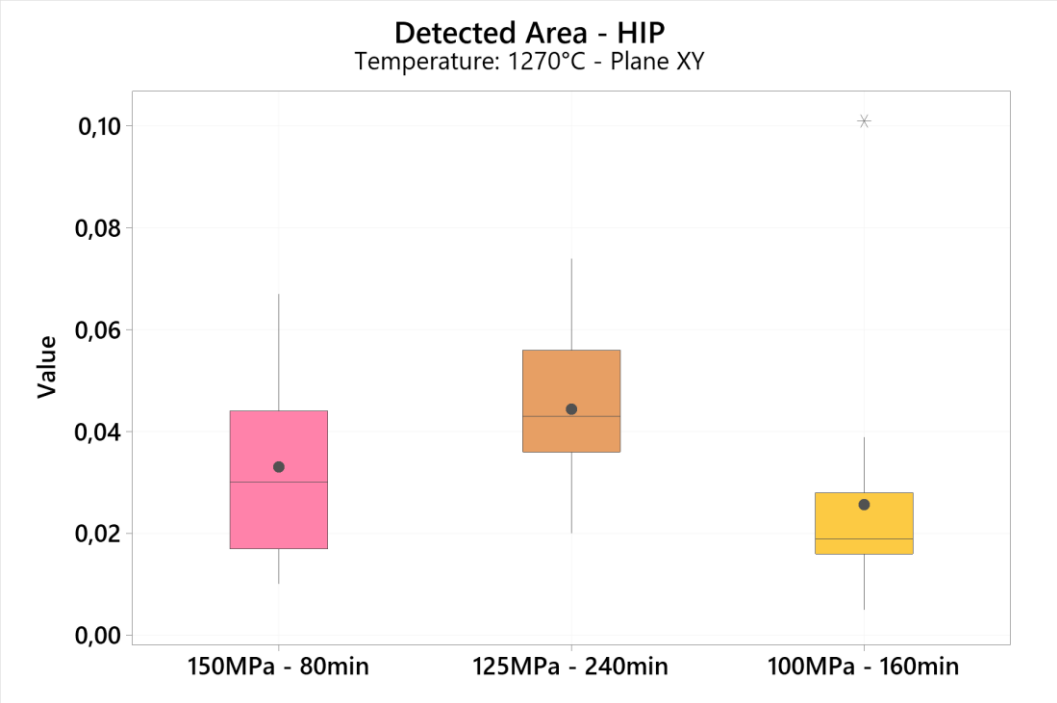

Fig. 78 Summary boxplot of residual porosity of the sample 7, 8 and 9 with the same process temperature, i.e. 1270 °C

The first noteworthy aspect is that, compared to the samples treated at 1290 °C and 1280 °C, these samples exhibit the lowest levels of total defectivity, indicating that they have achieved the highest effective density. In particular, Sample 8 shows the lowest percentage of residual porosity.

Analysing the histogram in Fig. 79, where the aspect ratio data of the three samples are compared, it can be observed that there is generally a decrease in the density of recorded values as the class increases, indicating a reduction in porosities with increasingly high shape ratios.

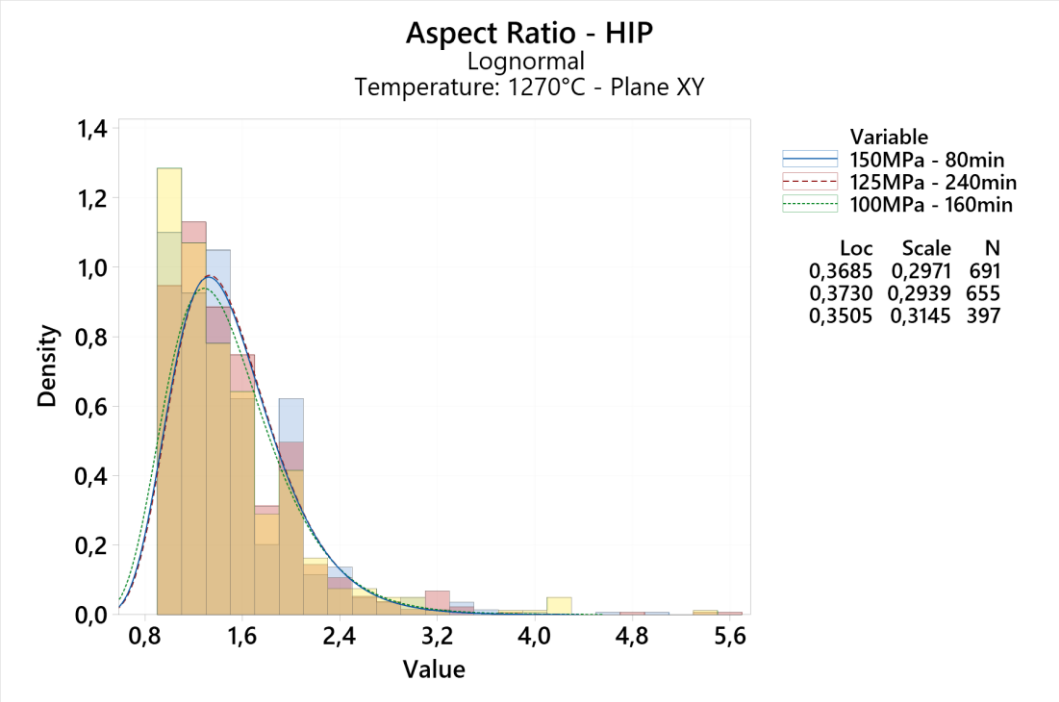

Fig. 79 Summary aspect ratio histogram of the sample 7, 8 and 9 with the same process temperature, i.e. 1270 °C

Similarly, for the samples treated at 1270 °C, the value range between 0.9 and 1.5 shows peaks at the highest density, suggesting that most of the porosities in the samples are spherical, likely due to trapped gas from the LPBF process. Finally, the last comparison concerns the average grain diameters shown in Fig. 80. This comparison reveals a particular trend: for Samples 7 and 9, the average grain diameter is about 35 µm, while for Sample 8, it reaches approximately 157 µm. A possible cause of this phenomenon could be related to the presence of carbides that regulate grain growth and the holding time at the given temperature.

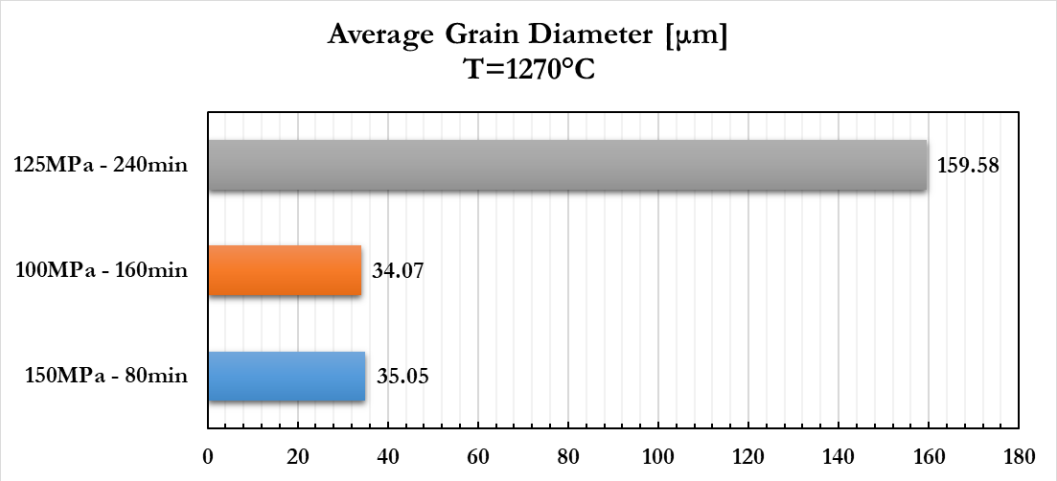

Fig. 80 Summary average grain diameter histogram of the sample 7, 8 and 9 with the same process temperature, i.e. 1270 °C

Specifically, in Fig. 81, it is observed that for Samples 7 and 9, treated for 80 and 160 minutes respectively, there are $M_{23}C_6$ and MC-type carbides at the grain boundaries, which reduce themselves in size. For Sample 8, however, only $M_{23}C_6$ carbides of smaller size and needle-like morphology are observed, while M_6C carbides have almost completely disappeared. Therefore, it is possible that as long as these two types of carbides are present and exceed a certain size, grain growth is restricted due to the pinning effect of the carbides on the grains. Once a certain processing period is exceeded and the carbides reduce themselves in size, then the grains are able to grow freely.

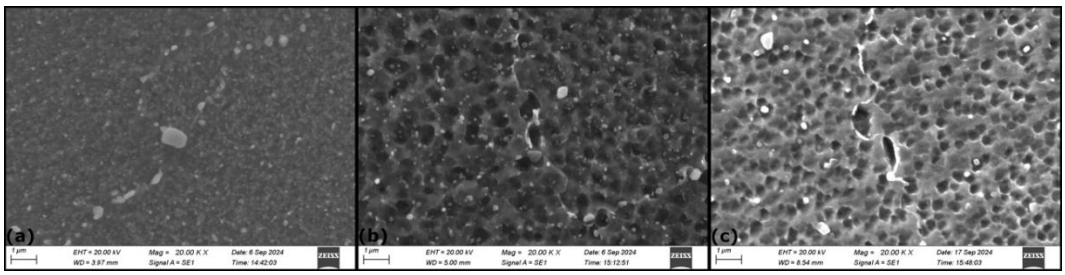

Fig. 81 SE1 signal showing a comparison between distribution and morphology of different types of carbides decorated grain boundary at different time process: (a) 80 min, (b) 160 min and (c) 240 min

In the following paragraph, the results obtained from the DOE will be reported and analysed, based on the data collected from the 9 samples treated with HIP.

3.4. Design of experiment results

To identify which of the three HIP parameters, respectively temperature, pressure, and time, was most influential to modify the density and grain microstructure, two different studies were conducted, considering the results obtained from the 9 samples.

3.4.1. DOE results for material density

First, the effects of the three parameters on the material's density were analysed. For each of the nine samples, 15 average residual porosity values were collected, corresponding to 15 images: 5 along the surface and 10 in the core. In Table 20 is reported the calculation of the mean value of the average volume fraction porosity resulting from defect analyses of HIP samples. This mean value was calculated for each of the 9 HIP samples to conduct the material density data analysis.

Table 20 Example of mean percentual residual porosity calculation for sample 9 (1270 °C – 100 MPa – 160 min)

Sample 9	*Residual Porosity [%]*	*Av. Residual Porosity [%]*	*St. Dev.*
Surface	0.031	**0.027**	0.009
	0.028		
	0.039		
	0.018		
	0.019		
Core	0.020	**0.025**	0.027
	0.022		
	0.011		
	0.005		
	0.101		
	0.018		
	0.013		
	0.017		
	0.016		
	0.026		

Minitab then provided the parameter with the greatest impact among the three, by using the average signal-to-noise ratio for all nine samples, ranking them from the highest to the lowest. This ratio is a robustness measure used to identify control factors that minimize process variability, reducing the impact of uncontrollable effects, or noise. Higher signal-to-noise ratios indicate control factor settings, that minimize noise factor effects. Since the goal for density was to minimize residual porosity, the analysis was conducted with Minitab's "smaller is better" option enabled. The numerical results are shown in Fig. 82.

Response Table for S/N Ratios - Porosity

Smaller is better

Level	Temperature	Pressure	Time
1	31,20	27,64	25,11
2	21,11	25,74	27,62
3	26,48	25,41	26,06
Delta	10,08	2,23	2,52
Rank	1	3	2

Fig. 82 Results of DOE "smaller is better" analysis

The Delta parameter, which corresponds to the difference between the highest and lowest mean values, is used by Minitab to classify the most influential parameter among those indicated. As shown in the table, temperature ranks first, meaning that to reduce porosity in the material with this treatment type, temperature is the fundamental parameter, followed by time and pressure with very similar values. Fig. 83 presents the main effects graph of the signal-to-noise ratio. This type of graph is used to examine level mean differences for one or more parameters. Specifically, a main effect occurs when different factor levels affect the response differently and is graphically represented by a non-horizontal line, with its slope indicating the main effect's magnitude: the steeper the slope of the line, the greater the magnitude of the main effect. From this figure, it is evident that the optimal parameter combination to minimize residual porosity is **1270 °C - 100 MPa - 160 minutes**. The values obtained align with the experimental analysis, as sample 9 exhibits the lowest residual porosity along both the surface and core.

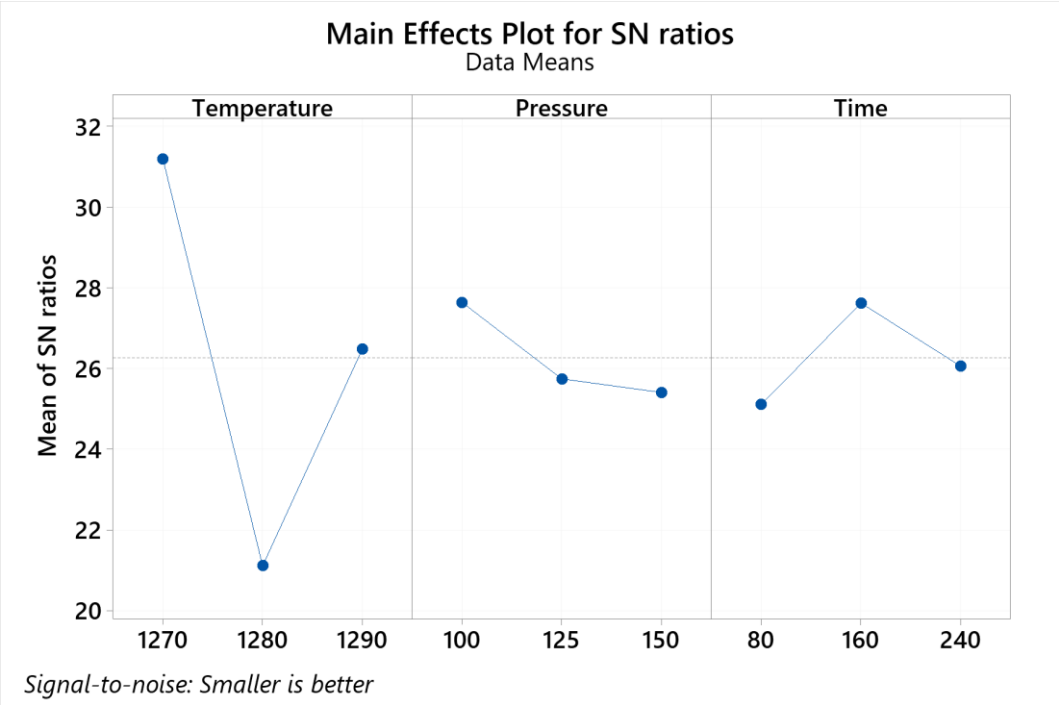

Fig. 83 Main effects plot for signal-to-noise ratios, considering maximum values of S/N ratios for each parameter

Another graph obtained with the Taguchi method, also related to main effects but using the average values as the response, is shown in Fig. 84.

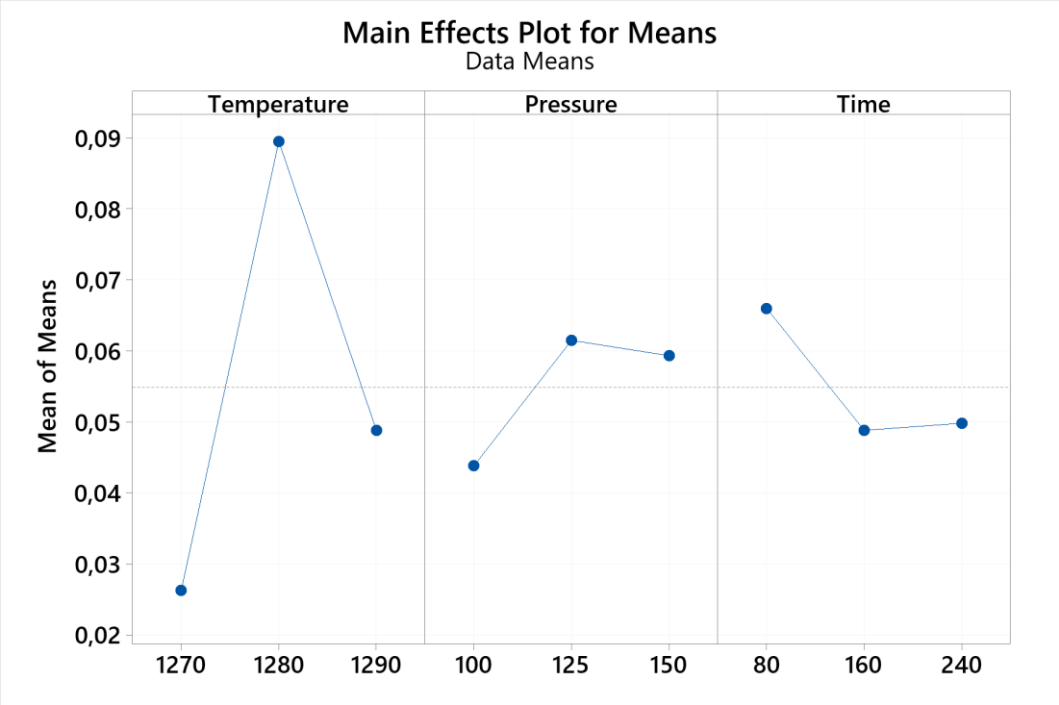

Fig. 84 Main effects plot for means. Consider minimum values of means for each parameter, which correspond to the best percentual porosity

The above chart always shows the combination obtained from the previous chart, confirming the optimal set of parameters. Remember that the residual porosity analysis was conducted with the 'smaller is better' option, so the values minimizing the mean should be considered.

In conclusion, a normal probability plot was also created to assess if the test results followed that distribution. Before examining the resulting plot, it is necessary to define certain parameters. Specifically, p-values from the regression analysis, which measure evidence against the null hypothesis (smaller p-values provide stronger evidence against the null hypothesis), were compared for all three parameters with a significance level of 0.05, which indicates a 5% risk of concluding that data do not follow a normal distribution when the data do follow a normal distribution. All three p-values obtained by DOE analysis exceed the significance level, indicating insufficient evidence to conclude that the data do not follow a normal distribution. Therefore, it is necessary to plot the data on a normal distribution graph, shown in Fig. 85, where it can be seen that the data follow the fitted distribution line closely, as they fall near this straight line. In summary, the normal distribution appears to be a good fit for the data.

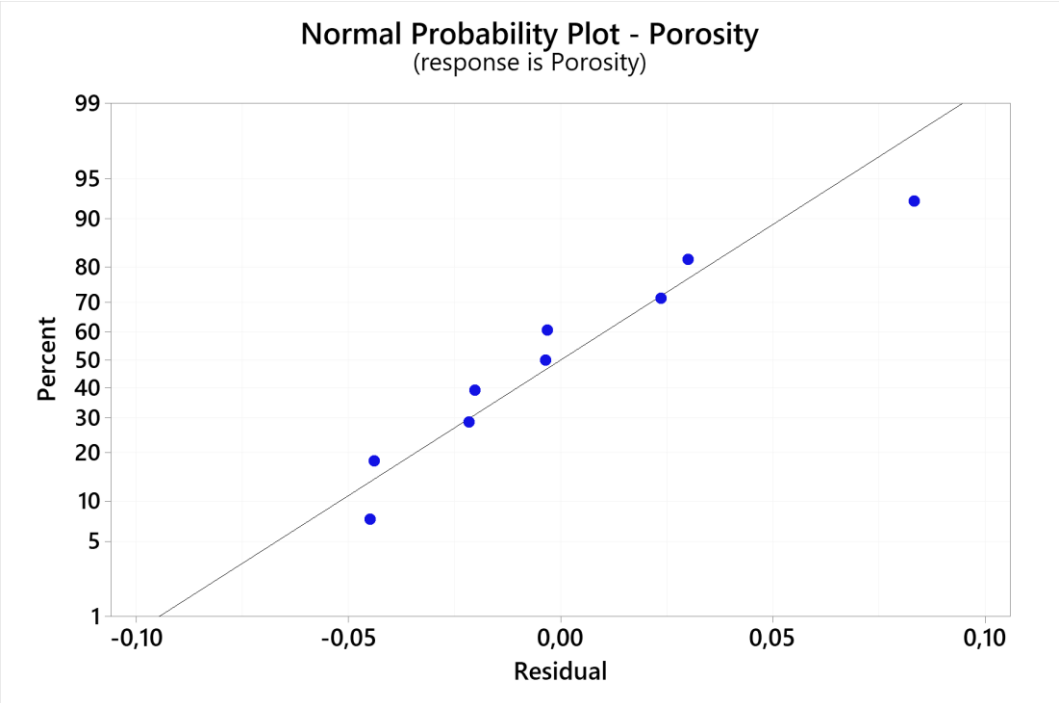

Fig. 85 Normal probability plot showing how the results obtained by DOE follow the normal distribution line

From the data obtained in the DOE analysis, conclusions can be drawn. In particular, as noted, the most impactful parameter for minimizing volumetric porosity is temperature. At this temperature, no liquid-phase areas due to incipient melting were observed; however, it is possible that the combined effect of temperature and time triggered solid-state diffusion phenomena, leading to the closure of residual porosity from the LPBF process. The second most impactful parameter is time, with 160 minutes likely being the optimal duration that allows the development of diffusion phenomena without causing the formation of liquid-phase areas from incipient melting, which would instead lead to undesirable effects like swelling and liquid shrinkage. As for pressure, it does not appear to have significant effects on the material's microstructure, as confirmed by the lower slope of the lines, shown in Fig. 83, compared to those representing temperature and time.

3.4.2. DOE results for grain size

The second analysis, also based on the Taguchi method, concerns the maximum crystal grain size obtained after HIP treatments, and in this case as well, it evaluates which of the three parameters has most influenced this growth. Average grain diameters were used as values for the analysis. Since the objective of this analysis is to achieve the greatest possible grain growth, the analysis was conducted with the "larger is better" option activated. Fig. 86 presents the table with the respective ranking of the three parameters based on the delta values, showing that, in terms of grain size growth, the most impactful parameter is time, followed by temperature and then pressure.

Response Table for S/N Ratios - Grain Size

Larger is better

Level	Temperature	Pressure	Time
1	35,20	36,19	36,89
2	40,02	40,71	36,02
3	38,85	37,17	41,16
Delta	4,82	4,52	5,15
Rank	2	3	1

Fig. 86 Results of DOE "larger is better" analysis

Fig. 87 displays the graphical representation of the main effects related to the signal-to-noise ratio. From this figure, it can be seen that the best combination of parameters for maximizing grain size is **1280 °C - 125 MPa - 240 minutes**.

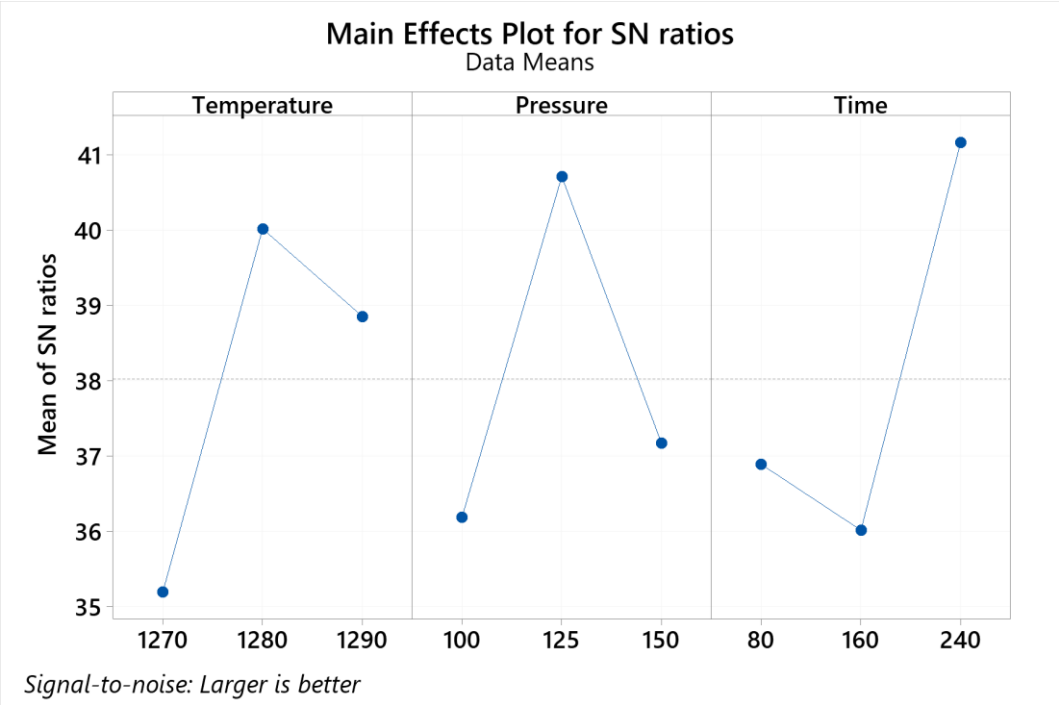

Fig. 87 Main effects plot for signal-to-noise ratios, considering maximum values of S/N ratios for each parameter

Meanwhile, Fig. 88 shows the graph related to the average values; it is important to note that in this case, the values to consider are those that maximize the mean value.

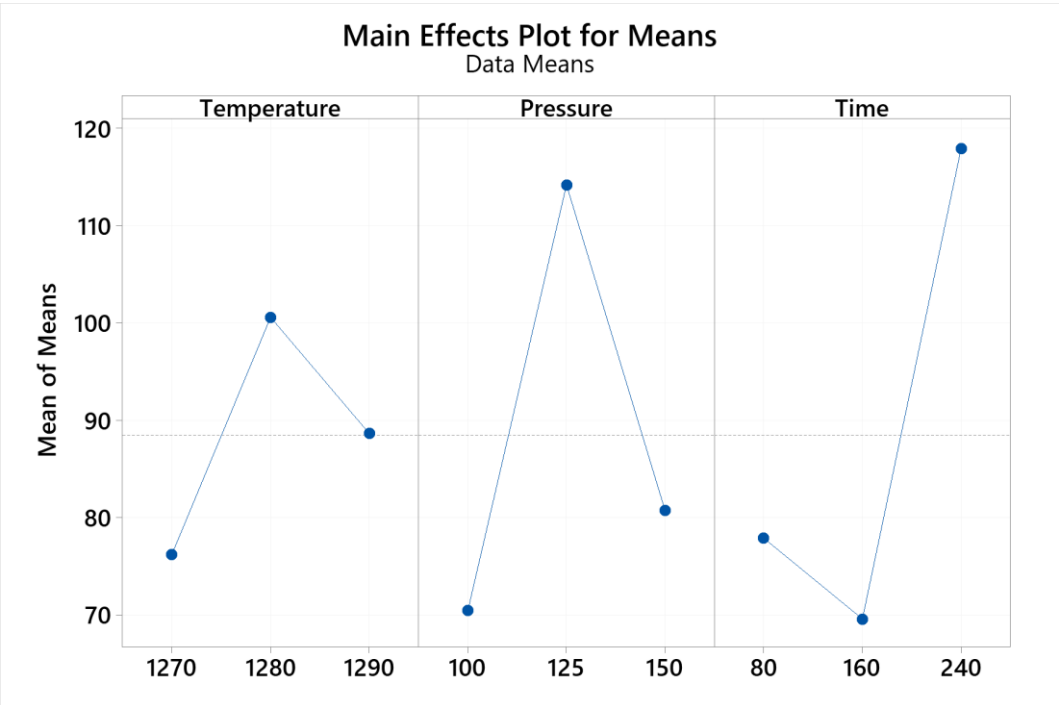

Fig. 88 Results of DOE larger is better analysis, best average grains diameter for each parameter

The last chart, shown in Fig. 89, displays the trend of the obtained data against the normal distribution line. As observed, the data on the average grain size also follows this trend. This indicates that the data for the average grain size approximates a normal distribution, assuming of normality plausible.

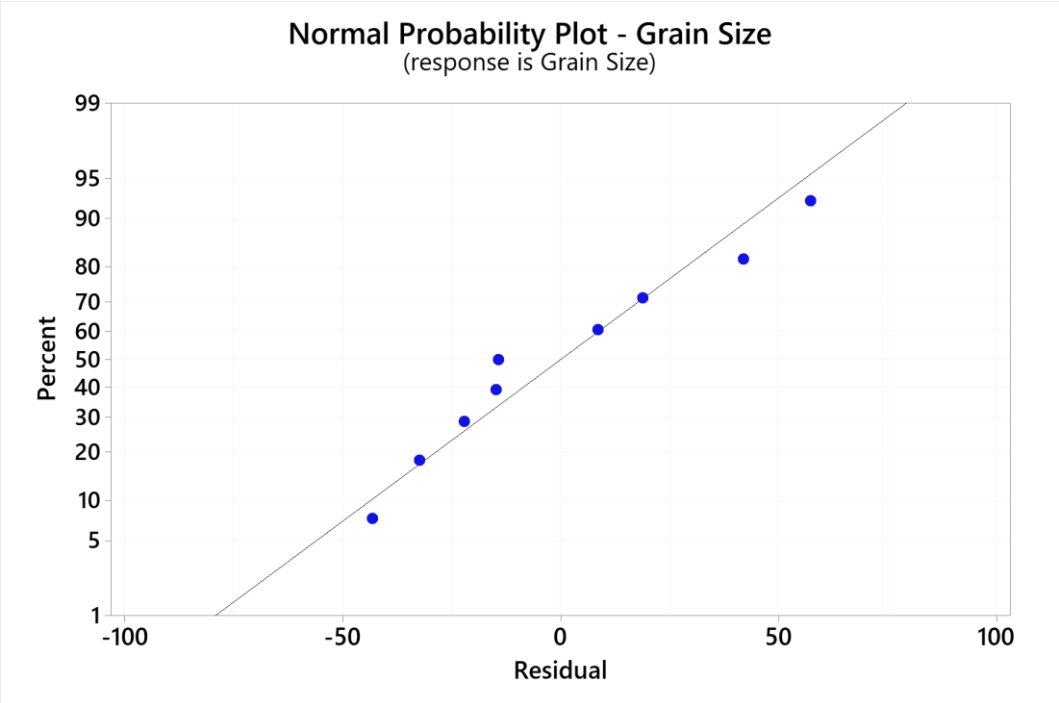

Fig. 89 Normal probability plot showing how the results obtained by DOE analysis related to grain size follow the normal distribution line

Considering the results obtained from the DOE, we can see that the most influential parameter for grain size growth is time rather than temperature, as it was in the previous analysis. An interesting point to observe is that, according to the results from the following analysis, the most influential temperature is not 1270 °C but 1280 °C. This could be due to the fact that at 1280 °C, a higher average grain diameter was obtained compared to the samples treated at 1270 °C, where a marked difference in values was observed between those treated at 80 and 160 minutes, versus the 240 minutes sample. It is also important to recall what was mentioned in the previous section regarding samples treated at 1280 °C, a temperature that corresponds to the segregation of Ti from the γ' phase toward the grain boundary to form $M_{23}C_6$ and MC carbides, which act as regulators of grain growth due to the pinning effect.

Moreover, it is interesting to note that, by observing the inclinations of the lines shown in Fig. 87, the pressure of 125 MPa had a greater influence than the other two values (with the highest recorded average). This could be due to the fact that such pressure allows for precipitation of carbides and γ' particles in quantities that are not so high as to hinder or slow down grain growth. However, this hypothesis requires further research for validation.

To conclude, the results from this DOE analysis showed that the greatest grain size growth occurred in a test not conducted under HIP conditions. Thus, the final step of this thesis work was to treat sample 10 to confirm or refute the analysis, using the following set of parameters: 1280 °C – 125 MPa – 240 min.

3.5. Sample 10: 1280 °C – 125 MPa – 240 min

Fig. 90 shows images of the remaining defects in sample 10, both near edge sample surface and core. Meanwhile, Table 21 provides a summary of the data related to the overall defectiveness of Sample 10.

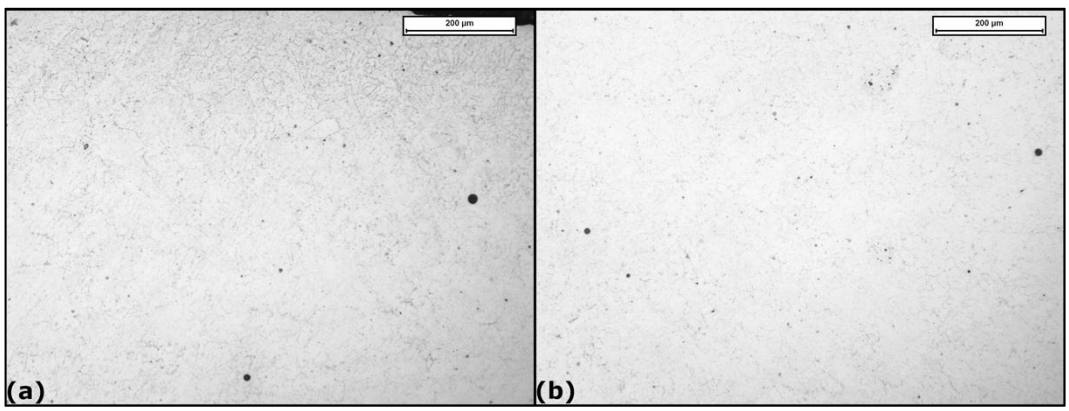

Fig. 90 Density analysis of sample 10 along surface (a) and core (b)

Table 21 Defect analysis summary of Sample 10

Sample 10	Av. Defects diameter [µm]	St. Dev.	Av. Vol. Porosities [%]	St. Dev.	Av. Aspect Ratio	St. Dev.
Surface	1.615	1.733	0.064	0.019	1.474	0.520
Core	1.965	1.893	0.094	0.056	1.504	0.514

Starting from the analysis of data on residual porosity, it can be seen that sample 10 shows a lower percentage of residual volumetric porosity compared to the other samples treated at 1280 °C. When compared to sample 6, which was treated for 240 minutes, it is noted that the average porosity value is lower at the sample's edge and slightly higher in the core. However, these differences are very small in percentage terms and therefore negligible. Interestingly, the average defect diameter values are also lower both along the surface and in the core. As for the average shape ratio, it aligns with those recorded for the other samples, consistently around 1.5, indicating that defects generally exhibit a spherical morphology typical of gas porosity.

Specifically, by analysing the histogram shown in Fig. 91, it can be seen that the highest density peak is in the 0.9 - 1.1 class, thus confirming a predominance of spherical residual porosity. However, it is also important to note a second isolated high-density peak in the 1.9 - 2.1 class. This data confirms the presence of some defects that exhibit a more elongated morphology along the major diagonal, which can no longer be attributed to gas porosity.

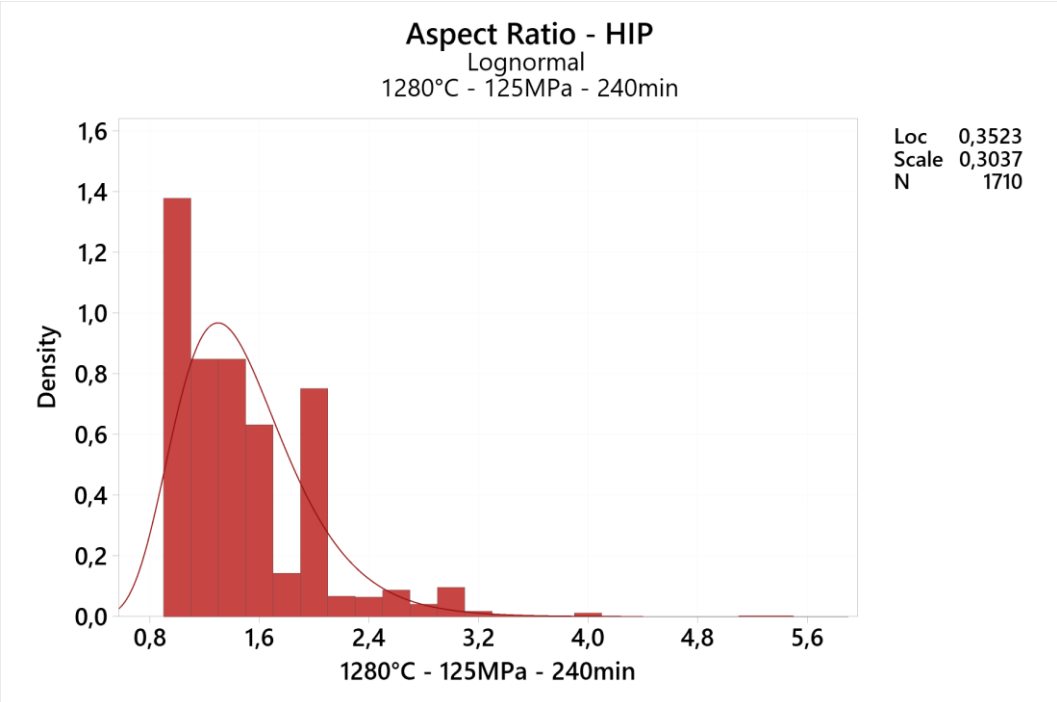

Fig. 91 Aspect ratio histogram of the Sample 10: 1280 °C – 125 MPa - 240 min

Here is the optical microscope observation of the grain-size microstructure of sample 10, shown in Fig. 92. In particular, this image reveals complete recrystallization of the initial microstructure and the formation of grains with an average diameter of approximately 102 μm.

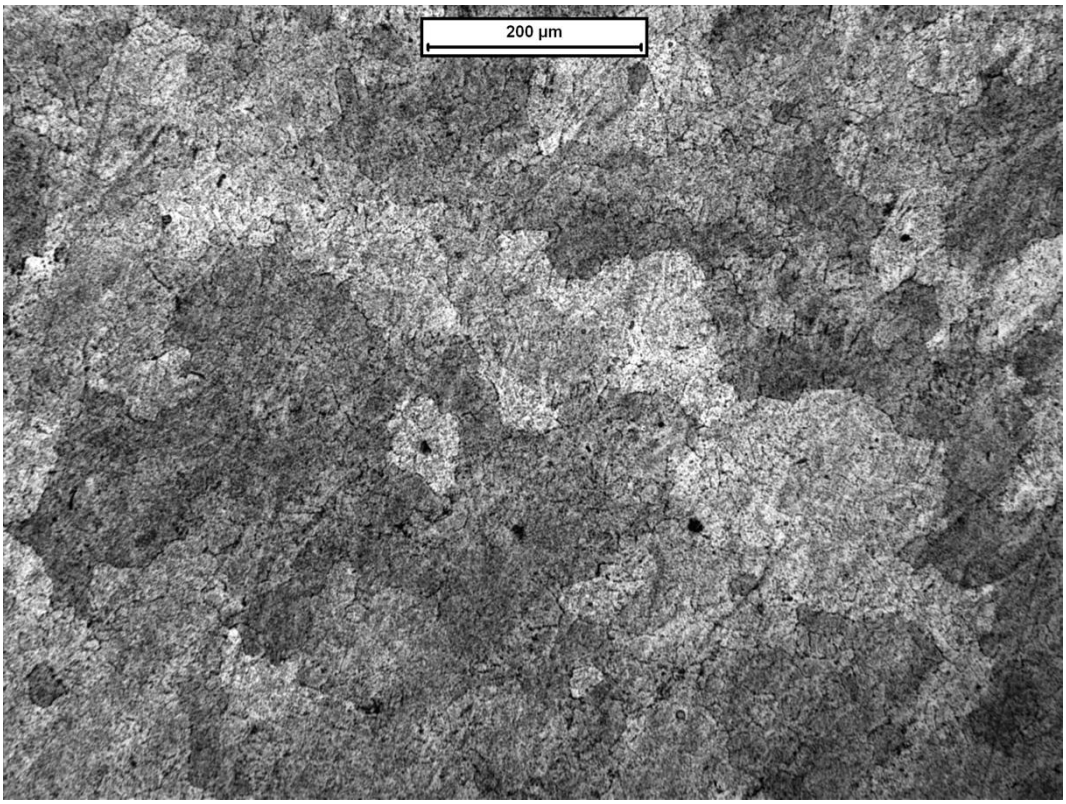

Fig. 92 Grain microstructure of Sample 10 with optical microscope at 100× magnification

This value can be interpreted as follows: with the same processing time, compared to sample 6, which was subjected to a pressure of 100 MPa, here a higher average diameter was observed. This could be due to the higher pressure, which posed a greater obstacle to the growth of carbides at grain boundaries, limiting their presence and thus allowing the grains to grow more freely. On the other hand, if we compare the average grain diameter with sample 5, under the same pressure conditions, it can be observed that, with a longer processing time, it is likely that Ti segregation at the grain boundaries led to the nucleation of a higher concentration of carbides and, consequently, restricted grain development due to the pinning effect.

However, to validate the following hypotheses, it is necessary to analyse the images obtained from SEM observation. Fig. 93 shows two images of the sample surface.

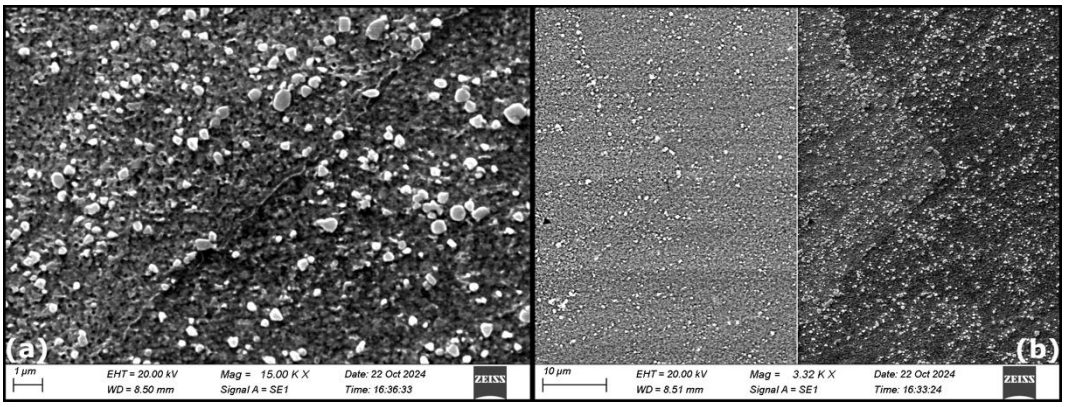

Fig. 93 (a) SE1 signal showing extremely fine grain boundary surrounded by high concentration of different types of carbides, (b) comparison of the same spot observed with the SE1 and BSD signal highlighting the high concentration of carbides and the absence of the γ' phase

Observing Fig. 93(a), a high concentration of carbides is evident across the entire surface; it is difficult to distinguish the exact type, but it is likely that MC-type carbides are present near the grain boundaries, while M_6C-type carbides are found within the grains. Another point to consider is the thickness of the grain boundary, which appears extremely thin and less pronounced, a significantly different behaviour compared to previous samples. In conclusion, it can be seen that, in this sample as well, the γ' phase is absent. This could be due to the complete or nearly complete segregation of Ti at the grain boundary, leading to the formation of various carbide types previously mentioned. In Fig. 93(b), the same area is shown, analysed with both SE1 and BSD signals, allowing for an even clearer view of the high concentration of carbides on the sample. Such a high enrichment of carbides in the alloy could, on one hand, enhance hardness and mechanical strength, but, on the other, it may also increase sensitivity to intergranular fracture, especially at high temperatures, due to embrittlement caused by the hard carbide phases present. Of course, this latter conclusion should still be excluded, because this alloy still needs further heat treatment steps, such as the aging steps.

As with the other samples, a comparison of the main aspects studied among the samples treated at 1280 °C is shown here as well. In particular, Fig. 94 shows a boxplot diagram of the residual volumetric porosity of the four samples, highlighting that, on average, sample 10 has a lower residual porosity than the other samples.

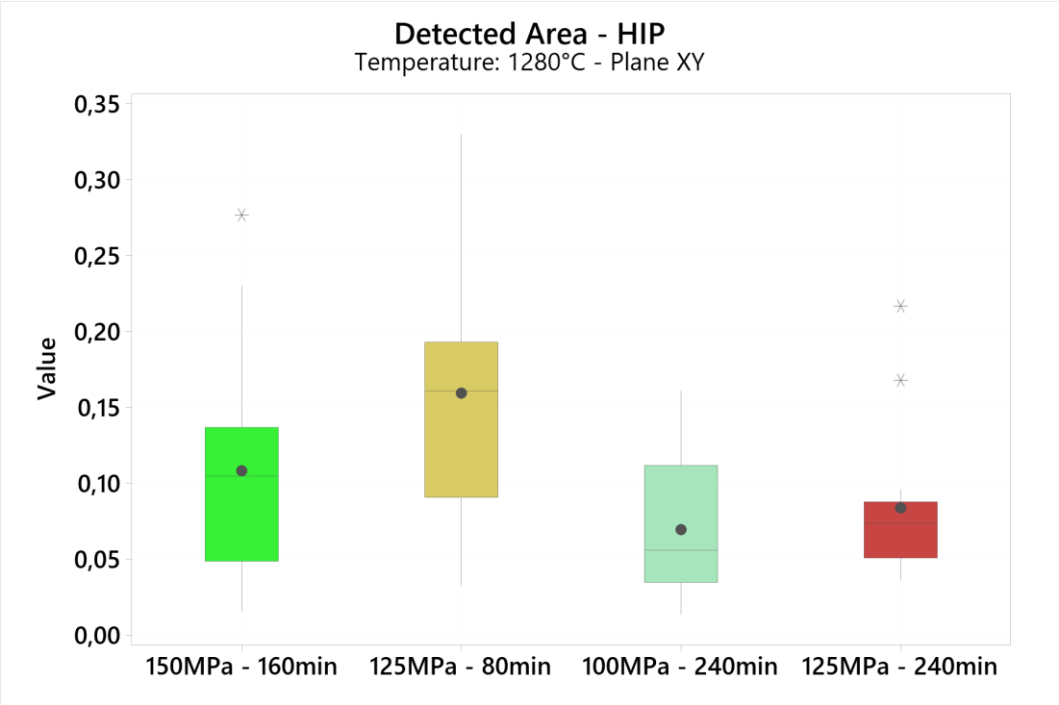

Fig. 94 Summary boxplot of residual porosity of the sample 4, 5, 6 and 10 with the same process temperature, i.e. 1280 °C

Subsequently, a histogram is shown in Fig. 95 to compare all recorded aspect ratio values, indicating that the highest-density peaks are concentrated in the value classes between 0.9 and 1.5. It is also interesting to note the presence of a second peak, common to several samples in the 1.9 - 2.1 range, suggesting the presence of a certain amount of non-spherical porosity likely resulting from gas porosity.

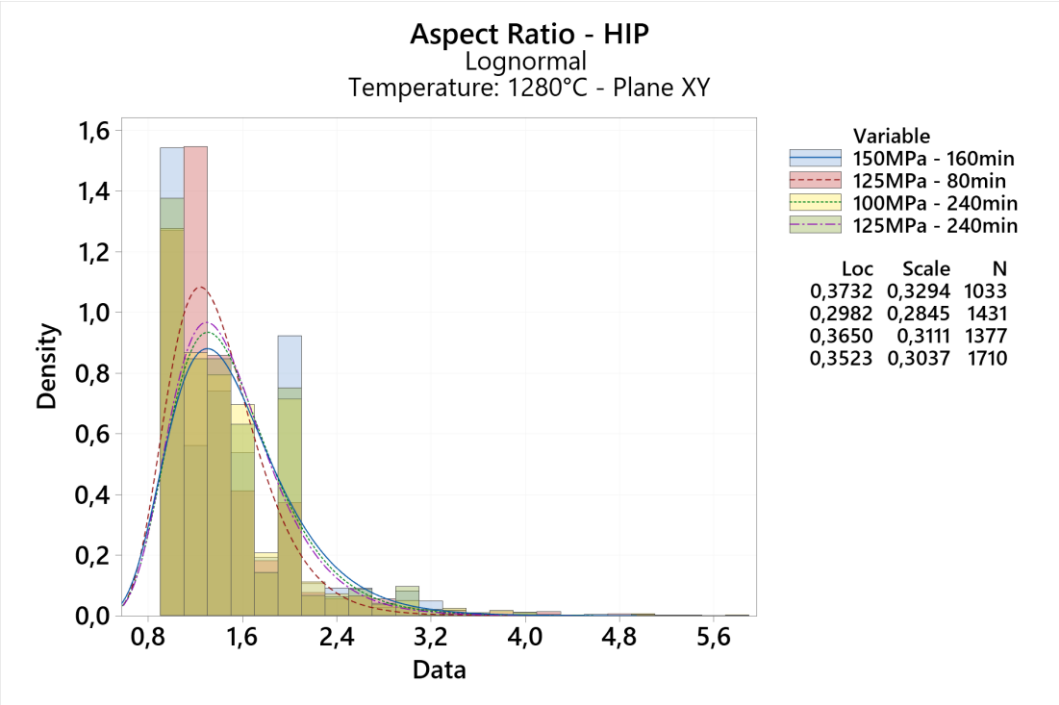

Fig. 95 Summary aspect ratio histogram of the sample 4, 5, 6 and 10 with the same process temperature, i.e. 1280 °C

Fig. 96 presents a comparison of the average grain diameters of the samples treated at 1280 °C, from which various hypotheses were previously drawn.

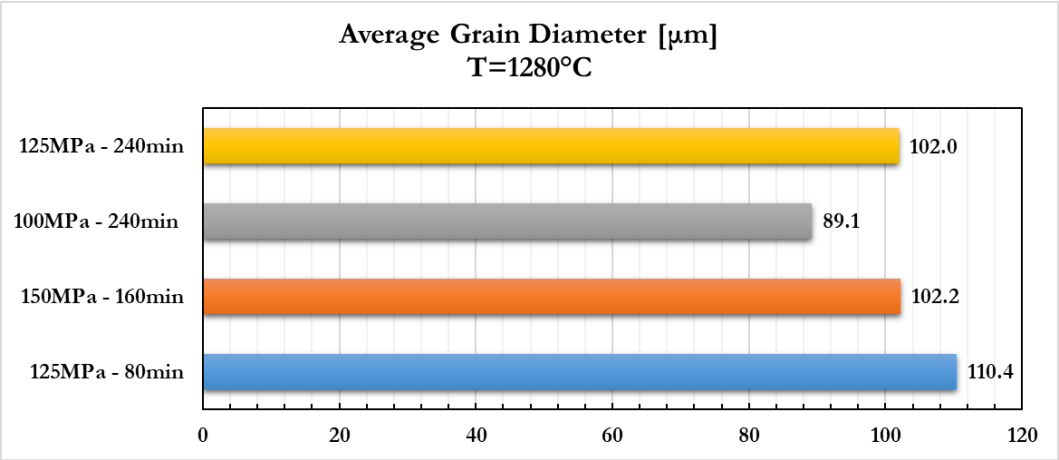

Fig. 96 Summary average grain diameter histogram of the sample 4, 5, 6 and 10 with the same process temperature, i.e. 1280 °C

Fig. 97 shows a synoptic table displaying all 10 samples, comparing the different grain size microstructures obtained after HIP treatment in the material's super-solid temperature range.

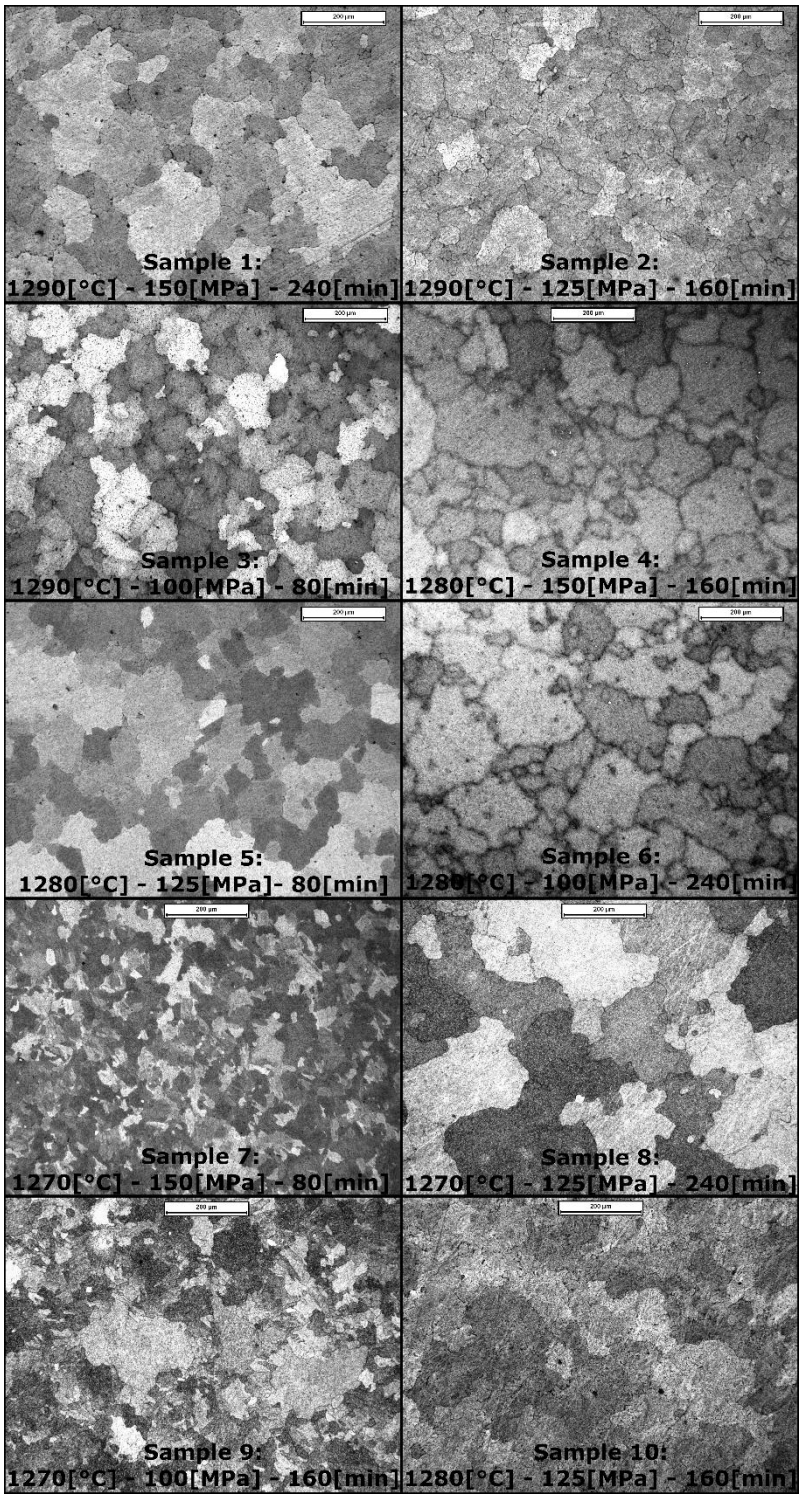

Fig. 97 HIP samples grain microstructure synoptic table

4. Conclusion

This thesis work focused on studying the feasibility of an alternative heat treatment for the Ni-based superalloy IN939 produced via LPBF, specifically employing Hot Isostatic Pressing (HIP). The production of Ni-based superalloy components through LPBF presents two contradictory aspects. On one hand, the advantage of using this technology lies in the ability to produce components with greater structural complexity, while also avoiding fixed (welded) or semi-fixed joints. On the other hand, a possible downside is the resulting microstructure which results extremely fine. This microstructure is not optimal for sustaining creep conditions, which traditionally needs a coarser grain size. However, by performing a dedicated heat treatment on the material obtained through the LPBF process, it is possible to modify the initial microstructure, achieving a fully dense material with coarse grains. IN939 is known for its excellent resistance to high temperatures (up to approximately 850 °C) and outstanding long-term microstructural stability. To address the grain size issue, the solution was using high temperatures above the solutioning temperature to induce complete recrystallization and eliminate the structural anisotropy resulting from the LPBF process. However, significant grain coarsening occurred only at temperatures above the solidus point of the alloy, causing the formation of a liquid-phase among the grains. The use of Hot Isostatic Pressing (HIP) which combined high pressures and temperatures during this procedure was capable of limiting and even impeding the formation of the liquid phase.

This thesis precisely focuses on this aspect, explaining how the use of high pressure and temperature can achieve the aforementioned microstructural goals.

This work started by assessing the material in its "as-built" state. Standard metallographic procedures were employed to evaluate the volumetric fraction of defects. Next, several heat treatments were conducted in an atmospheric furnace to determine the temperature range where the liquid formation occurred and how this condition would affect the final microstructure and the grain size. From these treatments, it was observed that incipient melting appeared at a temperature of 1290 °C. Subsequently, the study moved to the use of the HIP furnace. However, to optimize the combination of key parameters required for the HIP treatment—temperature, pressure, and time—the experimentation was organized following a 3x3 DOE (Design of Experiments) method, with two main objectives:

minimizing residual porosity and maximizing the grain size of the material. The main results for HIPped samples are reported below:

- **Samples treated at 1270 °C**: These samples showed an overall reduction of **56%** in the volumetric fraction of defects compared to the as-built samples. Moreover, when compared to the porosity reduction achieved through heat treatment performed in a static furnace in air, equal to **47%**, it becomes evident that not only high temperature but also high pressure contributes to further reducing the already low residual porosity of the material. Additionally, the average grain diameter recorded was **76 ± 72.18 μm**. At this specific temperature, the sample with the largest grain size, measuring 160 μm, was observed. Moreover, unlike the other samples, a more pronounced bimodal grain size distribution was noted.

- **Samples treated at 1280 °C**: These samples exhibited a **23%** increase in the volumetric fraction of porosity compared to the as-built samples. In this case, it is interesting to compare the percentage value with that obtained in the static furnace, where a **32%** decrease in porosity was recorded. An interesting aspect to note, when observing the percentage values related to heat treatments performed in the static furnace, is that as the treatment temperature in the static furnace increases, there is a rise in residual porosity. This is likely due to the formation of an increasingly higher concentration of the liquid phase, which is not controlled in any way by pressure. The average grain diameter was **101 ± 8.77 μm**. A key observation for these samples was the microsegregation of Ti from the γ' phase toward grain boundary and the consequential formation of small carbides. More specifically, Ti segregation increased with the passing of time. This phenomenon led to the formation of larger carbide which hindered the grain growth, ultimately reducing the average grain size.

- **Samples treated at 1290 °C**: These samples showed an overall reduction of approximately **25%** in the volumetric fraction of internal porosity compared to the as-built samples and an average grain diameter of **89 ± 16.23 μm**. This observation is further confirmed by this series of samples treated at this temperature. In fact, for the sample heat-treated at 1290°C in the static furnace, an increase in residual porosity of **230%** compared to the as-built sample was recorded. This is precisely

due to the high concentration of the liquid phase that forms at this temperature, which remains uncontrolled by the pressure within the static furnace, as it operates at atmospheric pressure. At this temperature, complete recrystallization and elimination of the initial anisotropy caused by the LPBF process were observed.

Based on the results obtained using the DOE and the Taguchi method, the optimal parameter combination for the super-solidus HIP treatment to maximize material density (i.e., minimize residual porosity) was determined to be **1270 °C - 100 MPa - 160 min**. Conversely, the parameter combination of **1280 °C - 125 MPa - 240 min** allowed for the maximization of the average grain size. This latter combination was applied to Sample 10, yielding an average grain diameter of **102 μm ± 8.56** and an average volumetric defect fraction of 0.079%. However, the average grain size was not larger than that recorded for Sample 8, which could be attributed to the interplay between temperature and Ti segregation. The following average grain diameter value remains consistent with those predicted by the DOE method, confirming the validity of this scientific approach to the problem. In the future, an improvement to this method could involve increasing the number of repetitions and expanding the range of temperature, pressure, and time.

Noteworthy, all the investigated samples didn't show any obvious trace of liquid formation, such as, dendritic grains or eutectic phases. This fact proves that the expansion of liquid pools was completely avoided in all the HIPped samples. However, further investigations are required to demonstrate whether the solidus temperature was increased, due to the application of the external pressure. In other words, it would be interesting to understand if liquid didn't form at all during the process. Conversely, it is still possible that only a minimal quantity of liquid was formed and then it was confined at grain boundaries triple points thanks to the application of the external pressure.

Anyhow, the samples showed improvements in both porosity reduction and grain size growth through the super-solidus HIP treatment. Future work should focus on the following heat treatments to prepare the material for service, particularly the homogenization treatments.

5. Acknowledgements

Eccomi qui, arrivato alla fine di un lungo, anzi lunghissimo percorso accademico durato tanti anni (se li conto mi viene quasi male a dirlo…) e che mi porterò sempre con me. In particolare, durante questi ultimi anni di università ho imparato alcune cose che vorrei scrivere e rendere indelebili qui su questo mio lavoro.

Ho imparato che, nel bene e nel male, la famiglia è la vera cosa che importa in questo mondo, che sarà sempre al tuo fianco e che farà di tutto per farti stare bene, anche quando le cose non vanno propriamente bene. Quindi grazie mamma e papà per la strada che mi avete permesso di intraprendere e per il futuro che ho davanti a me. Grazie a mio fratello che, anche se pensa che non gli voglia tanto bene, in realtà è esattamente il contrario e anzi, nutro un profondo senso di rispetto e ammirazione per quello che sei e per quello che stai facendo. Continua così brother! Grazie anche alle mie zie che sono sempre state lì a chiedermi come stessi e se tutto andasse bene, vi voglio un mondo di bene.

Ho imparato che i veri amici sono quelli che incontri e rimangono sempre lì al tuo fianco, che ti aiuteranno sempre e comunque perché sono, in un certo senso, la tua seconda famiglia. Quindi grazie alla mia compagnia, la Pía Pùa Malachia, per esserci sempre stata. Grazie a tutti quanti, soprattutto ai miei due migliori amici, Pagno e Albi, per aver ascoltato sempre tutto quello che avessi da dire e aiutato a prescindere da tutto. Grazie anche a tutti gli altri membri di questo bellissimo gruppo, siete i migliori!!

Ho imparato che oltre alla compagnia di amici di una vita, è possibile scoprire anche nuove persone che possono arricchirti e farti divertire allo stesso modo, ecco perché voglio ringraziare anche tutte quelle persone che ho incontrato in questi anni e al piccolo, ma fantastico, gruppo che è venuto a formarsi. Grazie a tutti voi, grazie alle due Laura, ad Andre e a Franci, ma soprattutto grazie a quei due pazzi di Albi e Nino, con cui ho condiviso tanti mesi in laboratorio e sul treno in balia di Alessandria e delle mille sfortune successe.

Ho imparato che abitare in una casa con persone che prima di allora non conoscevi minimamente è forse la cosa più importante e sperare di trovare le persone giuste lo è ancora di più. Posso dire di ritenermi fortunato perché in questi anni ho convissuto e condiviso la mia vita con persone fantastiche che mi hanno divertito e aiutato tanto. Grazie a Michi e

Hysni, i miei due condottieri con cui ho iniziato questa nuova avventura qui a Torino e poi grazie allo "Student Garden" che mi ha permesso di conoscere i migliori coinquilini possibili (tranne gli Erasmus…). Grazie a Chiara, Fabiola, Claudia, Daniele, le due Giorgia e Michele per aver fatto parte di questa mia avventura.

Ho imparato che non è vero che il mondo universitario è sempre serio, triste e difficile; esistono sempre delle eccezioni e nel mio caso questo lo devo al mio relatore, il Professor Emilio Bassini, che ha saputo mostrarmi quanto può essere affascinante, ma anche estremamente duro, il mondo scientifico e tutto quello che vi sta dietro. Grazie di tutto Professore.

Infine, ho imparato che è importante anche avere la consapevolezza di quello che si è riusciti a fare durante la propria vita, ecco perché voglio ringraziare me stesso con questo ultimo video

6. Bibliography

[1] K. Minet, A. Saharan, A. Loesser, and N. Raitanen, "Superalloys, powders, process monitoring in additive manufacturing," in *Additive Manufacturing for the Aerospace Industry*, Elsevier Inc., 2019, pp. 163–185. doi: 10.1016/B978-0-12-814062-8.00009-1.

[2] A. Kracke, "Superalloys, the Most Successful Alloy System of Modern Times-Past, Present, and Future," in *7th International Symposium on Superalloy 718 and Derivatives (2010)*, John Wiley & Sons, Inc., 2010, pp. 13–50. doi: 10.7449/2010/Superalloys_2010_13_50.

[3] M. J. Donachie and S. J. Donachie, "Selection of Superalloys," in *Superalloys: A technical Guide*, ASM International, 2002, ch. 2, pp. 11–24. doi: 10.31399/asm.tb.stg2.t61280011.

[4] Geddes B., Leon H., and Huang X., "Strengthening Mechanisms," in *Superalloys: Alloying and Performance*, 2010, pp. 17–24. doi: https://doi.org/10.31399/asm.tb.sap.9781627083133.

[5] S. Parizia, "Study of heat treatments for the Inconel 625 and process optimization for the Inconel 939 produced by Laser Powder Bed Fusion," Politecnico di Torino, Torino, 2022. Accessed: Sep. 27, 2024. [Online]. Available: https://iris.polito.it/retrieve/handle/11583/2827708/366477

[6] Geddes B., Leon H., and Huang X., "Overview of Superalloys," in *Superalloys: Alloying and Performance*, 2010, pp. 9–15. doi: https://doi.org/10.31399/asm.tb.sap.t53000009.

[7] G. P. Sabol and R. Stickler, "Microstructure of Nickel-Based Superalloys," *physical status solidi (b)*, vol. 35, no. 1, pp. 11–52, Jan. 1969, doi: 10.1002/pssb.19690350102.

[8] D. K. Ganji and G. Rajyalakshmi, "Influence of Alloying Compositions on the Properties of Nickel-Based Superalloys: A Review," in *Lecture Notes in*

Mechanical Engineering, Springer Science and Business Media Deutschland GmbH, 2020, pp. 537–555. doi: 10.1007/978-981-15-1071-7_44.

[9] Z. Mišković, M. Jovanović, M. Gligić, and B. Lukić, "Microstructural investigation of IN 939 superalloy," *Vacuum*, vol. 43, no. 5–7, pp. 709–711, May 1992, doi: 10.1016/0042-207X(92)90115-D.

[10] T. M. Pollock and S. Tin, "Nickel-based superalloys for advanced turbine engines: Chemistry, microstructure, and properties," 2006, *American Institute of Aeronautics and Astronautics Inc.* doi: 10.2514/1.18239.

[11] J. N. DuPont, J. C. Lippold, and S. D. Kiser, *Welding Metallurgy and Weldability of Nickel-Base Alloys*. Wiley, 2009. doi: 10.1002/9780470500262.

[12] M. J. Donachie and S. J. Donachie, "Understanding Superalloy Metallurgy," in *Superalloys*, vol. 3, ASM International, 2002, pp. 25–39. doi: 10.31399/asm.tb.stg2.t61280025.

[13] Reed Roger C., *The Superalloys - Fundamentals and Applications*, R. C. Reed 2006. Knovel, 2021. Accessed: Sep. 26, 2024. [Online]. Available: www.cambridge.org/9780521859042

[14] A. Mostafaei *et al.*, "Additive manufacturing of nickel-based superalloys: A state-of-the-art review on process-structure-defect-property relationship," Jul. 01, 2023, *Elsevier Ltd.* doi: 10.1016/j.pmatsci.2023.101108.

[15] J. Belan, "GCP and TCP Phases Presented in Nickel-base Superalloys," in *Materials Today: Proceedings*, Elsevier Ltd, 2016, pp. 936–941. doi: 10.1016/j.matpr.2016.03.024.

[16] Geddes B., Leon H., and Huang X., "Phases and Microstructure of Superalloys," in *Superalloys: Alloying and performance*, 2010, pp. 25–57. doi: https://doi.org/10.31399/asm.tb.sap.9781627083133.

[17] G. Liu, X. Xiao, M. Véron, and S. Birosca, "The nucleation and growth of η phase in nickel-based superalloy during long-term thermal exposure," *Acta Mater*, vol. 185, pp. 493–506, Feb. 2020, doi: 10.1016/j.actamat.2019.12.038.

[18] K. Hou *et al.*, "The formation of η-Ni3Ti phase microstructure in a cast nickel-based superalloy with high Ti/Al ratio," *Journal of Materials Research and Technology*, vol. 29, pp. 764–778, Mar. 2024, doi: 10.1016/j.jmrt.2024.01.156.

[19] Q. Zhu, G. Chen, C. Wang, L. Cheng, H. Qin, and P. Zhang, "Effect of the δ phase on the tensile properties of a nickel-based superalloy," *Metals (Basel)*, vol. 9, no. 11, Nov. 2019, doi: 10.3390/met9111153.

[20] J. Donachie Matthew and J. Donachie Stephen, "Understanding Superalloy Metallurgy," in *Superalloys: A Technical Guide*, ASM International, 2002, ch. 8, pp. 25–39. doi: 10.31399/asm.tb.stg2.t61280025.

[21] A. S. Wilson, "Formation and effect of topologically close-packed phases in nickel-base superalloys," Jun. 13, 2017, *Taylor and Francis Ltd.* doi: 10.1080/02670836.2016.1187335.

[22] Gibbons T. B. and Stickler R., *High Temperature Alloys for Gas Turbines 1982*. Dordrecht: Springer Netherlands, 1982. doi: 10.1007/978-94-009-7907-9.

[23] S. A. Raza, O. E. Canyurt, and H. K. Sezer, "A systematic review of Inconel 939 alloy parts development via additive manufacturing process," *Heliyon*, vol. 10, no. 3, Feb. 2024, doi: 10.1016/j.heliyon.2024.e25506.

[24] M. R. Jahangiri, S. M. A. Boutorabi, and H. Arabi, "Study on incipient melting in cast Ni base IN939 superalloy during solution annealing and its effect on hot workability," *Materials Science and Technology (United Kingdom)*, vol. 28, no. 12, pp. 1402–1413, Dec. 2012, doi: 10.1179/1743284712Y.0000000090.

[25] K. M. Delargy, S. W. K. Shaw, and G. D. W. Smith, "Effects of heat treatment on mechanical properties of high-chromium nickel-base superalloy I N 939," 1986.

[26] N. T. Aboulkhair, F. Bosio, N. Gilani, C. Phutela, R. J. M. Hague, and C. J. Tuck, "Additive manufacturing processes for metals," in *Quality Analysis of Additively Manufactured Metals: Simulation Approaches, Processes, and Microstructure Properties*, Elsevier, 2022, pp. 201–258. doi: 10.1016/B978-0-323-88664-2.00016-6.

[27] "Additive manufacturing-General principles-Fundamentals and vocabulary Fabrication additive-Principes généraux-Fondamentaux et vocabulaire INTERNATIONAL STANDARD ISO/ASTM 52900 ISO/ASTM 52900:2021(E) COPYRIGHT PROTECTED DOCUMENT." Accessed: Oct. 09, 2024. [Online]. Available: https://www.iso.org/obp/ui/#iso:std:iso-astm:52900:ed-2:v1:en

[28] A. S. Shaikh, "Laser powder bed fusion processing and heat treatment of Ni-base superalloys: microstructure and properties," Chalmers University of Technology, Gothenburg, Sweden , 2022. Accessed: Aug. 20, 2024. [Online]. Available: https://research.chalmers.se/publication/530468/file/530468_Fulltext.pdf

[29] C. Pauzon *et al.*, "Residual stresses and porosity in Ti-6Al-4V produced by laser powder bed fusion as a function of process atmosphere and component design," *Addit Manuf*, vol. 47, Nov. 2021, doi: 10.1016/j.addma.2021.102340.

[30] C. Pauzon, E. Hryha, P. Forêt, and L. Nyborg, "Effect of argon and nitrogen atmospheres on the properties of stainless steel 316 L parts produced by laser-powder bed fusion," *Mater Des*, vol. 179, Oct. 2019, doi: 10.1016/j.matdes.2019.107873.

[31] J. Reijonen, A. Revuelta, T. Riipinen, K. Ruusuvuori, and P. Puukko, "On the effect of shielding gas flow on porosity and melt pool geometry in laser powder bed fusion additive manufacturing," *Addit Manuf*, vol. 32, Mar. 2020, doi: 10.1016/j.addma.2019.101030.

[32] A. Caballero, W. Suder, X. Chen, G. Pardal, and S. Williams, "Effect of shielding conditions on bead profile and melting behaviour in laser powder

bed fusion additive manufacturing," *Addit Manuf*, vol. 34, Aug. 2020, doi: 10.1016/j.addma.2020.101342.

[33] M. C. Karia, M. A. Popat, and K. B. Sangani, "Selective laser melting of Inconel super alloy-a review," in *AIP Conference Proceedings*, American Institute of Physics Inc., Jul. 2017. doi: 10.1063/1.4990166.

[34] N. T. Aboulkhair, M. Simonelli, L. Parry, I. Ashcroft, C. Tuck, and R. Hague, "3D printing of Aluminium alloys: Additive Manufacturing of Aluminium alloys using selective laser melting," Dec. 01, 2019, *Elsevier Ltd.* doi: 10.1016/j.pmatsci.2019.100578.

[35] "EOS NickelAlloy IN939 Material Data Sheet Metal Solutions."

[36] T. Mishurova, S. Evsevleev, P. Piault, A. King, L. Henry, and G. Bruno, "Understanding the hot isostatic pressing effectiveness of laser powder bed fusion Ti-6Al-4V by in-situ X-ray imaging and diffraction experiments," *Sci Rep*, vol. 13, no. 1, Dec. 2023, doi: 10.1038/s41598-023-45258-1.

[37] S. Li, Q. Wei, Y. Shi, C. K. Chua, Z. Zhu, and D. Zhang, "Microstructure Characteristics of Inconel 625 Superalloy Manufactured by Selective Laser Melting," *J Mater Sci Technol*, vol. 31, no. 9, pp. 946–952, Sep. 2015, doi: 10.1016/j.jmst.2014.09.020.

[38] D. Zhang, Z. Feng, C. Wang, W. Wang, Z. Liu, and W. Niu, "Comparison of microstructures and mechanical properties of Inconel 718 alloy processed by selective laser melting and casting," *Materials Science and Engineering: A*, vol. 724, pp. 357–367, May 2018, doi: 10.1016/j.msea.2018.03.073.

[39] G. Marchese *et al.*, "Study of the microstructure and cracking mechanisms of hastelloy X produced by laser powder bed fusion," *Materials*, vol. 11, no. 1, Jan. 2018, doi: 10.3390/ma11010106.

[40] A. S. Shaikh, M. Rashidi, K. Minet-Lallemand, and E. Hryha, "On as-built microstructure and necessity of solution treatment in additively manufactured

Inconel 939," *Powder Metallurgy*, vol. 66, no. 1, pp. 3–11, 2023, doi: 10.1080/00325899.2022.2041787.

[41] G. Marchese *et al.*, "The influence of the process parameters on the densification and microstructure development of laser powder bed fused inconel 939," *Metals (Basel)*, vol. 10, no. 7, pp. 1–19, Jul. 2020, doi: 10.3390/met10070882.

[42] F. Zhang *et al.*, "Effect of heat treatment on the microstructural evolution of a nickel-based superalloy additive-manufactured by laser powder bed fusion," *Acta Mater*, vol. 152, pp. 200–214, Jun. 2018, doi: 10.1016/j.actamat.2018.03.017.

[43] M. R. Stoudt *et al.*, "The Influence of Annealing Temperature and Time on the Formation of δ-Phase in Additively-Manufactured Inconel 625," *Metall Mater Trans A Phys Metall Mater Sci*, vol. 49, no. 7, pp. 3028–3037, Jul. 2018, doi: 10.1007/s11661-018-4643-y.

[44] G. Marchese *et al.*, "Influence of heat treatments on microstructure evolution and mechanical properties of Inconel 625 processed by laser powder bed fusion," *Materials Science and Engineering: A*, vol. 729, pp. 64–75, Jun. 2018, doi: 10.1016/j.msea.2018.05.044.

[45] S. Sanchez *et al.*, "Powder Bed Fusion of nickel-based superalloys: A review," Jun. 01, 2021, *Elsevier Ltd.* doi: 10.1016/j.ijmachtools.2021.103729.

[46] V. D. Divya *et al.*, "Microstructure of selective laser melted CM247LC nickel-based superalloy and its evolution through heat treatment," *Mater Charact*, vol. 114, pp. 62–74, Apr. 2016, doi: 10.1016/j.matchar.2016.02.004.

[47] A. Mostafa, I. P. Rubio, V. Brailovski, M. Jahazi, and M. Medraj, "Structure, texture and phases in 3D printed IN718 alloy subjected to homogenization and HIP treatments," *Metals (Basel)*, vol. 7, no. 6, Jun. 2017, doi: 10.3390/met7060196.

[48] A. Hilaire, E. Andrieu, and X. Wu, "High-temperature mechanical properties of alloy 718 produced by laser powder bed fusion with different processing parameters," *Addit Manuf*, vol. 26, pp. 147–160, Mar. 2019, doi: 10.1016/j.addma.2019.01.012.

[49] S. Goel, M. Ahlfors, F. Bahbou, and S. Joshi, "Effect of Different Post-treatments on the Microstructure of EBM-Built Alloy 718," *J Mater Eng Perform*, vol. 28, no. 2, pp. 673–680, Feb. 2019, doi: 10.1007/s11665-018-3712-0.

[50] Chandler Harry, "Heat Treating Superalloys," Chandler Harry, Ed., ASM International, 1996, ch. 2. Accessed: Nov. 14, 2024. [Online]. Available: https://app.knovel.com/kn/resources/kpHTGPPNA2/toc?b-q=Heat%20Treater%27s%20Guide%3A%20Practices%20and%20Procedures%20for%20Nonferrous%20Alloys&include_synonyms=no&q=Heat%20Treater%27s%20Guide%3A%20Practices%20and%20Procedures%20for%20Nonferrous%20Alloys&sort_on=default

[51] J. Donachie Matthew and J. Donachie Stephen, "Heat Treating," in *Superalloys: A Technical Guide*, ASM International, 2002, pp. 135–147. doi: https://doi.org/10.31399/asm.tb.stg2.t61280135.

[52] Chandler Harry, "Heat Treating Superalloys," in *Heat Treater's Guide - Practices and Procedures for Nonferrous Alloys*, Chandler Harry, Ed., ASM International, 1996, ch. 2.

[53] X. Li *et al.*, "Effect of heat treatment on microstructure evolution of Inconel 718 alloy fabricated by selective laser melting," *J Alloys Compd*, vol. 764, pp. 639–649, Oct. 2018, doi: 10.1016/j.jallcom.2018.06.112.

[54] N. L. Loh and K. Y. Sia, "An overview of hot isostatic pressing," *J Mater Process Technol*, vol. 30, no. 1, pp. 45–65, Feb. 1992, doi: 10.1016/0924-0136(92)90038-T.

[55] J. Cormier and C.-A. Gandin, "Processing of directionally cast nickel-base superalloys: solidification and heat treatments Charles-André Gandin. Processing of directionally cast nickel-base superalloys: solidification and heat

treatments. Nickel base single crystals across length scales PROCESSING OF DIRECTIONALLY CAST NICKEL BASED SUPERALLOYS-SOLIDIFICATION AND HEAT TREATMENTS," pp. 193–222, 2022, doi: 10.1016/b978-0-12-819357-0.00015-9ï.

[56] M. J. Donachie and S. J. Donachie, "Superalloys for High Temperatures—a Primer," in *Superalloys*, ASM International, 2002, pp. 1–9. doi: 10.31399/asm.tb.stg2.t61280001.

[57] M. R. Jahangiri, S. M. A. Boutorabi, and H. Arabi, "Study on incipient melting in cast Ni base IN939 superalloy during solution annealing and its effect on hot workability," *Materials Science and Technology (United Kingdom)*, vol. 28, no. 12, pp. 1402–1413, Dec. 2012, doi: 10.1179/1743284712Y.0000000090.

[58] "4.1: DESIGN OF EXPERIMENTS VIA TAGUCHI METHODS-ORTHOGONAL ARRAYS 14.1.1: SUMMARY OF TAGUCHI METHOD 14.1.1.1: PHILOSOPHY OF THE TAGUCHI METHOD." [Online]. Available: https://eng.libretexts.org/@go/page/22674

[59] R. K. . Roy, *A primer on the Taguchi method*. Society of Manufacturing Engineers, 2010.

[60] K. Song and M. Aindow, "Grain growth and particle pinning in a model Ni-based superalloy," *Materials Science and Engineering: A*, vol. 479, no. 1–2, pp. 365–372, Apr. 2008, doi: 10.1016/j.msea.2007.09.055.

[61] M. M. Attallah, H. Terasaki, R. J. Moat, S. E. Bray, Y. Komizo, and M. Preuss, "In-Situ observation of primary γ' melting in Ni-base superalloy using confocal laser scanning microscopy," *Mater Charact*, vol. 62, no. 8, pp. 760–767, Aug. 2011, doi: 10.1016/j.matchar.2011.05.001.